Towards Quantum Teleportation from a Spontaneous Parametric Down-Conversion Source to a Quantum Dot Spin by Hong-Ou-Mandel Interference

by

Alexander Peter Burgers

A dissertation submitted in partial fulfillment
of the requirements for the degree of
Doctor of Philosophy
(Physics)
in The University of Michigan
2015

Doctoral Committee:

Professor Duncan G. Steel, Chair
Professor Paul R. Berman
Professor Cagliyan Kurdak
Professor Theodore B. Norris
Associate Professor Vanessa Sih

For my wife, Evangeline

My parents, Peter and Bonnie

And my brother, Mark

ACKNOWLEDGEMENTS

First off I want to thank my adviser Duncan Steel, because without him I would not be successful in this field. Duncan invited me into his lab after I spent almost two years working on the LHC. He was instrumental in getting me excited about spectroscopy and quantum optics. After a month's worth of group meetings and lab work I was hooked and haven't looked back since. Duncan has helped me along every step of the way with advice and encouragement. I truly believe he is one of the finest mentors a young scientist could ever hope to have, and I count myself lucky to have had the privilege of working with him. Second to Duncan the most influential person in the lab was John Schaibley. John taught me nearly everything I needed to know about lab work and experiments in the Steel lab and what he didn't know, we figured out together. He was a truly great partner and mentor to me and he is an excellent scientist. The basis of the entanglement project presented in this thesis is the work John and I completed together, on which we spent many long nights in lab collecting data and trouble shooting the experiment. It gives me great pleasure to count John as one of my friends and colleagues.

After completion of the entanglement experiment I embarked on a new project involving teleportation (the content of this thesis). I am very grateful to Luming Duan and Paul Berman for stimulating discussions in making this next step. Along with Duncan, we developed a new plan involving Paul Kwiat and J. J. Wong at the University of Illinois for a teleportation protocol that would bring together two different quantum systems. The implementation of this experiment requires a number

of people and the most vital to me has been Uttam Paudel (The Pal). Uttam came from a similar particle physics background as I did so we immediately hit it off and began working on the teleportation experiment. We knew that the light collection must be improved for this experiment so this was our first hurdle, and it was quite the hurdle. Over a year and one resurrected cryostat later, we began to make progress. If research could ever be described as being "in the trenches" this was it, and I can't think of a better comrade than Uttam. Day in and day out, we lurched along improving things and troubleshooting the set-up, with of course some breaks to discuss philosophy and politics. Though it was hard at the time, I don't think I have had more fun being in the lab discussing experiments and physics than during that era. What helped make the time so fun was the presence of Cameron Nelson, Colin Chow, and Aaron Ross in the lab as well. We were each struggling with different aspects of our own experiments, but there was a real "brothers in arms" feel to the lab. We helped each other with new ideas and jokes to preserve sanity. The Steel lab is a special place because of all the great people we have working with us and the environment fostered by Duncan. It has been the greatest privilege of my life to work in this lab and with these people.

None of this research could be possible without the help and support of the excellent staff in the physics department. Chrissy Zigulis helped me greatly while I was transitioning into Duncan's Lab and dealing with the difficult task of completely shifting my research focus. The entire student services staff has been very helpful with issues encountered during graduate school. Honorary SSO member Midhat Farooq is always there to discuss life and propose a beer run.

Labs don't work if the building doesn't work and no one makes our building work better than Paul T-H-U-R-M-O-N-D. He is on top of every building issue we have and he will advocate on behalf of the labs to get the best operation out of our good Old Randall. Truly our research would be impossible with out him and Joe Sheldon.

A number of friends and colleagues have helped me along the way. I have to especially thank Jake, Ryo, and Ben; these guys kept me sane during first-year and beyond. We helped each other survive and I am going to miss them very much. We grew into the best of friends and I know that will last a lifetime. I was lucky enough to have one of my best friends from college and high school, Alex Mueller, in Ann Arbor with me for 6 years. Alex was getting his math PhD, and he and I, along with Evangeline, brought a little bit of the U to Ann Arbor. My grad school friends and non-grad school friends have made my time here very special . Ann Arbor has provided me with a lot of great memories and friends and it will be hard to leave but the memories and impact on my personal growth will last me forever.

Before even coming to Ann Arbor my life was set in motion by my family. Both of my parents, Peter Burgers and Bonnie Yoder (Papa and Mama) have fostered my curiosity and given me love and support through every stage of my life, and continue to do so. I would not be remotely where I am without them and I am so grateful to have them as parents. I hope I can be half as good of parent as they were. The only person in the world who knows what it was like to have these excellent parents is my brother Mark. Mark and I have helped shaped each other through the years. We are much more similar than either of us really think and I am thankful for that. Sometimes in science Nature doesn't always work the way we expect, but in this case Nature saw fit to send me a best friend, advocate and partner in crime all wrapped into one. My family has been instrumental in my growth and success and I don't think I can ever thank them enough.

Finally, the most important person to me through this whole grad school experience has been my best friend in the world, my wife Evangeline. Her love and support have allowed me to wake up everyday and know I can face the challenges in front of me. She makes me think in ways I never have before and has a truly complementary personality to my own. Doing something like a PhD can affect the loved ones around

you and I am so grateful to her for the encouragement she gives me, even sometimes after working in the lab for 24 hours. Without her support I know I would not have been able to do this and she has made my time here in Ann Arbor infinitely better. I am so lucky to have such an amazing partner and I look forward to the next chapter of our lives together.

Thank you Ann Arbor! It has been fun!

TABLE OF CONTENTS

LIST OF FIGURES

Figure

CHAPTER I

Introduction

The desire to understand fundamental quantum processes in nature drives current research on technologies that exploit and enhance our understanding of quantum mechanics. One area receiving much interest is quantum information. In its simplest form, quantum information uses the principles of coherent superposition, a cornerstone of quantum theory, to represent information. A yes or a no (a 1 or a 0) is an example of how to represent classical information; however, by utilizing the principle of superposition, quantum information allows for a system to exist in a state of both yes and no (1 and 0) simultaneously. We call this a quantum bit or qubit. The versatility provided here gives rise to a multitude of improvements over classical schemes: encryption, information transport and computing times are a few examples of current technologies that would be greatly enhanced using quantum information. Yet for all the positive impacts and improvements that can be made using quantum mechanics, a deeper understanding of its role in nature is what truly energizes research. This thesis will demonstrate how fundamental tests of quantum mechanics are coupled to improvements in the field of quantum information. To begin, a well-motivated quantum system is chosen for study. This work will focus on solid-state quantum dots (QDs) and their interactions with the radiation field. QDs are small islands (20nm in diameter and 3nm tall) grown in semiconductor structures. Dots exhibit

three-dimensional confinement and under the proper circumstances a single electron can be confined to the dot. This ground-state electron will serve as the qubit (spin-up or spin-down) as it relates to quantum information. The QD spin state is addressed via application of optical fields where the emitted or scattered radiation is used to read-out or transport information from the system. The measurement of scattered or emitted radiation and how that relates to the dynamics of the QD system give insight into properties such as entanglement, which can be exploited in a number of ways. Additionally, classification of QDs as single emitters is determined by observing the scattered radiation arrival statistics. With a single electron in the ground state there exists an optically accessible excited state transition by way of electron-hole pair creation (an exciton). This three quasi-particle state (the confined electron and the electron-hole pair) is referred to as a trion. Once excited to the trion state, a decay via spontaneous emission will leave the dot in either of the spin states (up or down), or more precisely in a superposition of spin states. Now the emitted radiation, or single photon pulse, carries the information of the spin-state in its polarization or frequency. Determining, or measuring, the photon pulse in one of these degrees of freedom will collapse the QD spin wavefunction into a single state. For example, if radiative decay to spin-up corresponds to a horizontally (H) polarized decay channel, then a polarization sensitive detector would collapse the wavefunction to spin up if H polarized radiation is registered. So, actions performed on the single photon pulse have an influence on the spin state coherence. Interference between this single photon pulse and a similar pulse from another system on a beam splitter, say, can influence both respective systems similarly. In some cases the systems that produced the photon pulses (maybe two QDs) can become entangled with each other. Other situations may involve information coded in one single photon pulse to be transferred, through interference, to the other pulse and, by virtue of its entanglement with the system of origin (the QD spin), this information is transferred to that system. This information

transfer is referred to as teleportation. This thesis will explore the role of interference in information transfer and how this can be used to further the field of quantum information. Involved, is a detailed description of the entanglement generated between a QD and a single photon pulse and the properties of the photon pulse itself. A further investigation, tackles the manipulations that can be made through interference with this photon pulse. The beginning is the study of two photon pulses generated by the same QD. These are not generated at the same time but one after another where the first photon pulse is delayed to ensure temporal overlap on the beam splitter. An added complication arises when a separate QD is used for the second photon pulse due to mismatch in frequency and decay profiles, however, if QDs have a viability for future applications interactions between separate dots must be realized. Finally, the use of a completely different source of single photon pulses permits the study of a QDs interaction with disparate systems and further analysis of interference. For this thesis the single photon pulse pairs generated in spontaneous parametric down-conversion (SPDC) are employed due to their already established impact on quantum information and the ability to create high brightness sources. As all of these experiments involve building statistics, detection efficiencies and brightness of sources is extremely important to attain the signal to noise necessary for claims of entanglement and teleportation. All aspects of the preceding experiments shall be discussed, including the difficulties in performing the measurements and significance to the field arising from their completion.

CHAPTER II

Quantum Dots for Quantum Information Architectures

2.1 Introduction

The pursuit for a working quantum computer is one of the most important technological endeavors of the modern era, requiring scalable quantum computing architectures. By replacing classical computing bits with quantum bits (qubits), we are able to exploit the nature of quantum mechanics to drastically improve computing power and encryption protocols. While a classical bit can be either 0 or 1, a qubit exists as a superposition of two states meaning that it is simultaneously in both states until a measurement is performed. This effect allows for computation times much smaller than classical computers. Though the field is still young, some research has already been done on determining what systems could be used to build a quantum computer. A few different systems have emerged as promising qubits: trapped ions, Nitrogen vacancy centers in diamond, superconducting qubits, donor-spins in silicon, and semiconductor quantum dots (QDs). This chapter discusses some of the current systems studied for quantum information applications and focus particularly on QDs and their potential as a quantum computing qubit.

2.2 Other Platforms

Though QDs will be the focus of this work, a short study of the current competing technologies is necessary to get an accurate look at the field of quantum information. Furthermore, many of the techniques and protocols studied and developed for the following systems are useful when studying QDs. Since many of these systems utilize optical manipulation and readout methods, the primary tools for quantum dots, much can be gained by study of dissimilar systems.

2.2.1 Trapped Ions and Neutral Atoms

Perhaps the most mature technology for quantum information platforms; trapped ions are enhanced by the fact that all of the optical control techniques now used in a varied of other solid-state systems had their origin in atomic systems. Many of the quantum information protocols, like DLCZ, began in atoms [28]. Indeed, spin-photon entanglement and teleportation using matter qubits (not just entangled photon pairs) were first done in atomic systems [12, 68, 4, 59]. For all the advantages of atomic system, scalability has been the main issue, though there is much work being done to improve this [79, 40, 20]. There are even emerging techniques for quantum error correction, which will be the only way a universal quantum computer can avoid the crippling effects of decoherence [21].

One disadvantage these systems have is scalability, and though all quantum information systems suffer from this problem, the field of atoms has a harder time with overcoming the obstacle. In order to get an atom prepared in such a way that you can preform the necessary quantum information techniques to do meaningful manipulations, complicated atom-trapping techniques are employed. The scaling of these techniques has been achieved to some degree, but solid-state qubits have the advantage that they are stationary and can exploit nano-fabrication techniques to create large arrays of structures. Atoms are approaching this state but it is hard to imagine

a laptop quantum computer powered by an atom cloud. Of course quantum technologies maybe so fundamentally difficult that a quantum computer laptop is not a realistic thing to consider when evaluating the merits of each quantum technology.

2.2.2 Nitrogen Vacancy Centers in Diamond

Nitrogen vacancy (NV) centers in diamond occur as defects in the diamond structure where a Nitrogen atom couples with a vacancy (lack of a carbon atom) to form an optically accessible system. In principle this system has the added bonus that the dynamics can be observed at room temperature. However, the optical transitions in NV centers become highly broadened by phonons so most of the experiments are carried out at cryogenic temperatures. This limitation is not as fundamentally crippling as it is in GaAs systems where the exciton simply does not exist at room temperature. The electron qubit in the NV is shown to be an attractive qubit for quantum computing and many of the crucial entanglement protocols have been achieved by previous groups [81]. Distant spin entanglement was recently achieved in these systems as well [8].

Recently NV centers have emerged as useful tools for magnetic sensing and this may be their technological future[54]. The nuclear spin coupling to the electron spin coupled with the optical readout method allows these devices to sense very small changes in magnetic fields. By placing the NV in a diamond cantilever, fine magnetic sensing of phenomena such as Majorana fermion states in solids, and topological insulators may be possible.

There are additional solid-state systems that exist for the purposes of quantum computing and each has it's own advantages and disadvantages. With this in mind, likely the most powerful quantum technology may be a hybrid of two or three utilizing the strengths exhibited by each.

2.2.3 Spontaneous Parametric Down Conversion

Spontaneous parametric down conversion (SPDC) describes the process by which a nonlinear medium generates single photon pairs when irradiated by a strong optical pump field. Due to conservation of energy the emerging photons' frequencies must add to the pump frequency $\omega_p = \omega_1 + \omega_2$. Additionally, these two photons can form polarization entangled states [48]. The entanglement can be exploited to do a number of protocols involving Bell state measurements, and universal quantum gates [46, 67]. Since SPDC quantum information technologies or linear optical quantum computing (LOQC) do not contain a matter qubit, scaling can be difficult when considering quantum algorithms requiring large numbers of qubits. However, quantum cryptography platforms requiring fewer qubit states and the ability to transport protected quantum information across long distances, as demonstrated between the Canary Islands, is powerful [53].

For the reasons described above our group has teamed up with Paul Kwiat's group at the University of Illinois to get the QD spin-photon entangled state to interact with SPDC photons using teleportation. The robustness of photons as an information channel make this endeavor useful and the field of quantum information is moving more towards trying to implement hybrid-quantum systems. As we have seen each quantum information system has its own strengths and weaknesses and we hope to utilize both strengths of the QD-SPDC hybrid system to accomplish interesting and useful science.

2.3 QD Spins as Qubits

The main topic of this work will be on the optical study and manipulation of QDs. In particular we will focus on optical spin manipulations of a single electron confined to a QD structure. Using selective charging provided by a diode structure,

we are able to confine a single electron to the QD and, under an applied magnetic field in the direction transverse to the crystal growth direction, exploit the qubit nature of the electron spin (aligned and anti-aligned to the direction of the field). The optical techniques used in initialization and readout of the spin state are discussed in detail and through careful analysis of these optical interactions we are able to extract interesting information about the coherence of the QD optical transitions. Since the spin states are split, if we construct our experiment in such a way that we cannot tell which of the states the photon decayed to and only that there was a photon present, then we have a spin-photon entangled state. Verifying this entanglement is an important part of this work since it is the crux of the teleportation protocol we wish to implement. If the QD photon is not entangled with the spin state then teleportation cannot occur. This will be discussed in more detail later.

Almost 20 years ago DiVincenzo outlined criteria that should be met for QDs to be viable as a quantum information platform [51, 27]. Here we outline the criteria and the current status of QD technologies as it relates to each:

► **Identification of well defined qubits.** The QD system we mainly study in our lab consists of a single electron confined to the QD. This electron provides us with a qubit when a magnetic field is applied, where addressing and accessing the qubit spin has been achieved by many different groups including our own. The electron qubit is not the only qubit that can be utilized in QD structures. Some groups use the hole spin instead of the electron and even the ground and excited state of QD exciton can form a qubit. For now we will restrict our discussion to the electron qubit.

►**Reliable state preparation.** For many quantum information protocols we must be able to initialize to a pure spin state. The entanglement experiment discussed in chapter V, and indeed all subsequent measurement utilizing spin-photon entanglement (teleportation, spin-spin entanglement, etc.) rely on the ability to initialize to a single spin state. Our group has shown the nature of this initialization

before and by nature of our successful entanglement experiment we can infer good initial state preparation [72, 88].

►**Low decoherence rate.** In practice the decoherence rate of the qubit is measured by how many operations (spin flips) one can perform before the spin state decoheres. Using nuclear spin locking techniques discovered by our lab we are able to achieve electron coherence time on the order of μs [89]. The gate operations on a QD spin can be generated by an optical pulse of width 2ps, meaning 10^6 operations can be performed before decoherence [66, 45].

►**Universal set of quantum gates.** Any quantum operation can be constructed out of a control-not (cnot) gate and a qubit rotation. This was demonstrated in our group previously [50]. However, the scalability of such an operation is questionable and a more elegant approach would be to utilize coupled quantum dots or quantum dot molecules (QDM) to generate two-qubit spin gates [22].

►**Strong qubit-specific measurements** For this case we are looking for a non-destructive measurement of the spin state. So, by measuring the spin state one destroys the coherence by transferring population to an excited state that can then decay to the other spin state (This is the readout method used in the spin-photon entanglement verification), this criteria is not satisfied. In atomic physics they utilize what is known as a cycling transition. Essentially this is a closed loop transition that only exists for one of the qubit states so no population can be transferred to the other qubit state. In QDMs, discussed above, a specific charge configuration can lead to a non-destructive cycling transition that can be used as a readout method [44].

2.4 Quantum Teleportation

As discussed in section 2.2.3, our final goal is to show teleportation between the spin-photon entangled state from the QD and a controllable single photon state from a SPDC source. In order to achieve this teleportation we must first verify that the

photon spontaneously emitted from the QD carries information about the spin state and when interfered with a SPDC photon, the information coded on the SPDC photon is teleported onto the spin state of the QD. Quantum teleportation has been achieved in other systems including both QDs and SPDC, and for a pedagogical description of teleportation, *Bouwmeester et. al.* is a good reference [13].

2.5 Conclusion

Here we have outlined some of the current technologies for quantum information architectures. In particular, QDs were discussed in greater depth and the DiVincenzo criteria was laid out for QDs as viable quantum computing qubits, where we have demonstrated nearly all of the required criteria. The integration of the QD system with the SPDC system will be discussed later in the thesis.

CHAPTER III

Electronic properties of Self-Assembled InAs/GaAs Quantum Dots

3.1 Introduction

The QDs studied in this thesis are self-assembled Indium Arsenide (InAs) dots grown using molecular beam epitaxy. The InAs is deposited on a Gallium Arsenide (GaAs) structure, the details of GaAs structure will be discussed later, where a 7% mismatch in the lattice constant creates strain fields in the crystal. The strain fields give rise to the island structures that, when capped with more GaAs, become our QDs. The three dimensional confinement leads to a number of interesting properties particularly when considering optical interactions. This chapter will discuss the bulk properties of crystal structures, particularly GaAs, and how the three dimensional confinement achieved in QD heterostructures leads to atomic-like behavior.

3.2 Bulk Semiconductor Properties

The semiconductor systems of interest in this thesis are III-V structures. An important property to keep in mind throughout the discussion of the optical and electronic properties of these solids is that bare atoms, the III category (In and Ga) and the V category (As), have electron valence shells in the s and p orbitals. While in a

crystal the properties become more complicated due to the periodicity and interaction in the solid, the carriers still retain s and p type characteristics. GaAs and InAs are both zincblende structures, meaning it has a tetrahedral structure where each atoms is surrounded by four atoms of the opposite type. The electronic band structure (shown in figure 3.1) behaves as a parabola at the center of the first Brillouin zone ($k = 0$), or the Γ point. Additionally, at the center of the Brillouin zone, the eigenfunctions in each band retain the symmetry inherent to that bands basis functions. For the valence band, the basis functions are x, y, and z, indicating a p orbital-like; and the conduction band basis functions are s orbital-like [76]. When we include spin the total angular momentum, $\mathbf{j} = \mathbf{l} + \mathbf{s}$, we obtain additional states in both the conduction and valence band. For the conduction band we have only two states since $\mathbf{j} = 1/2$ and $j_z = \pm 1/2$, however the valence band becomes more complicated and is summarized in the table below.

Valence band states		
Total angular momentum ($\mathbf{j}$)	z-projection (j_z)	Band label
1/2	$\pm 1/2$	Split-off (SO)
3/2	$\pm 1/2$	light hole (LH)
3/2	$\pm 3/2$	heavy hole (HH)

An important consequence of the angular momentum states is that we must consider the effect of spin-orbit coupling. Spin-orbit coupling arises from the fact that an electron moving in an electric field will observe an effective magnetic field due to relativistic effects. The Hamiltonian for this interaction can be approximated from the Dirac equation, assuming an isotropic spin-orbit interaction in the crystal,

$$H_{so} \approx \lambda_{so} \mathbf{L} \cdot \mathbf{S}. \tag{3.1}$$

Where λ_{so} is a constant. Using the fact that $\mathbf{J}^2 = (\mathbf{L} + \mathbf{S})^2$, we can replace Eqn 3.1 with the following,

$$H_{so} \approx \lambda_{so} \frac{\mathbf{J}^2 - \mathbf{L}^2 - \mathbf{S}^2}{2}. \tag{3.2}$$

The split off (SO) band is shifted in energy from the light hole (LH) and heavy hole (HH) bands by the interaction energy extracted from Eqn. 3.2,

$$\Delta_{so} = \frac{3}{2}\hbar^2 \lambda_{so}. \tag{3.3}$$

The energy associated with this splitting is much larger than any that would arise from strain or confinement and as such the SO band is neglected in our experiments.

The next consideration is given to the HH and LH bands. For this treatment it is necessary to look at the periodic potential in crystalline solids and solve for the wavefunctions of electrons in one of the bands. The periodic potential can be written as $V(\mathbf{r}) = V(\mathbf{r} + \mathbf{R})$ and the corresponding Bloch states for an electron in a specific band b become,

$$\langle \mathbf{r} | \Psi^b_{\mathbf{k}} \rangle = e^{i\mathbf{k}\cdot\mathbf{r}} u^b_{\mathbf{k}}(\mathbf{r}). \tag{3.4}$$

As discussed above, at the Γ point we can take angular momentum to be a good quantum number and use the angular momentum states in further discussion. An important note is that away from $k = 0$ this assumption is no longer valid and care must be taken to use the correct approach when solving for the bandstructure. The famous $\mathbf{k} \cdot \mathbf{p}$ method for calculating band structure is most commonly used for calculations away from the center of the first Brillouin zone[39]. For now it is useful to write the Bloch states from Eqn. 3.4 for the HH and LH in the angular momentum representation as $|u^j_{j_z}\rangle$, with j being the total angular momentum number and j_z the z

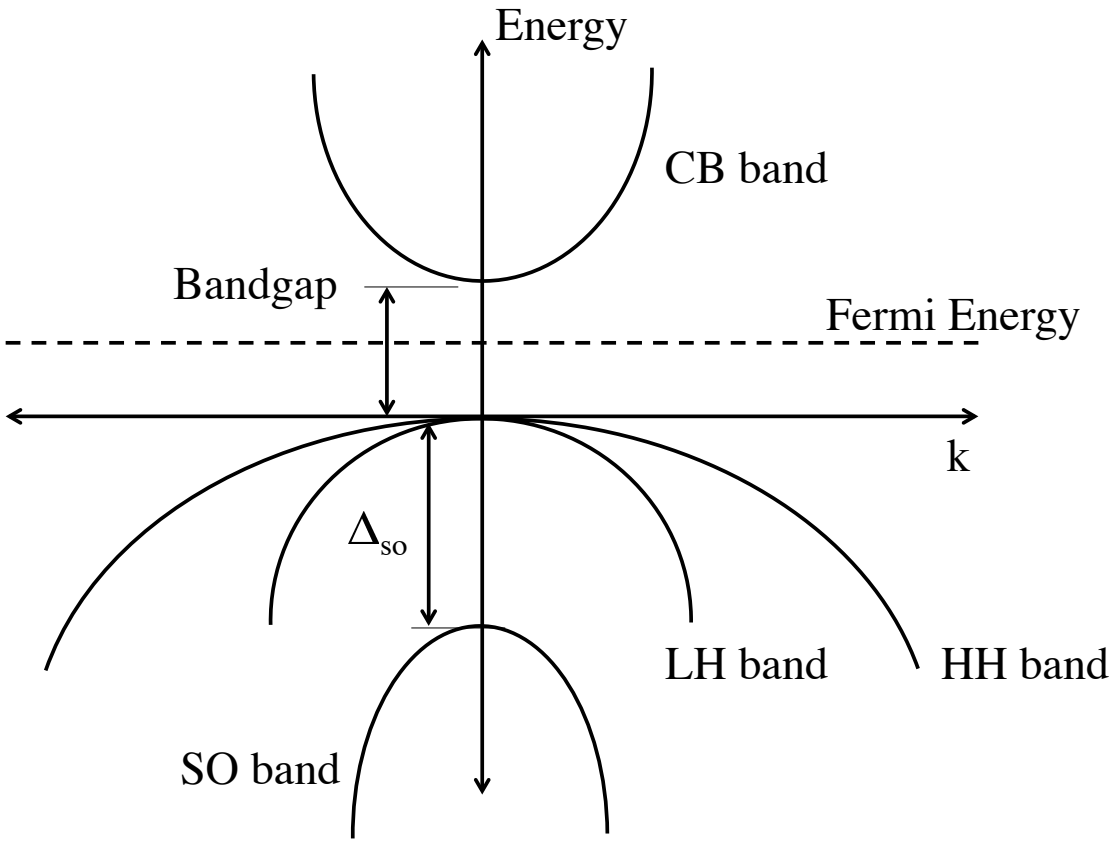

Figure 3.1: The electronic band structure for GaAs (or InAs). Due to spin-orbit coupling the split-off (SO) band is shifted in energy by Δ_{so}. Since this is a diagram of the bulk band structure the light hole (LH) and heavy hole (HH) bands are degenerate, however, when strain and confinement are introduced, as is the case for QDs, the degeneracy is broken.

projection of angular momentum. We have included the Clebsch-Gordon coefficients and the arrow ($\uparrow$ and $\downarrow$) direction signifies the spin states along the crystal growth direction (z).

$$\begin{aligned}
|u^{3/2}_{+3/2}\rangle &= -\frac{1}{\sqrt{2}}|x+iy\rangle\uparrow \\
|u^{3/2}_{-3/2}\rangle &= \frac{1}{\sqrt{2}}|x-iy\rangle\downarrow \\
|u^{3/2}_{+1/2}\rangle &= -\frac{1}{\sqrt{6}}|x+iy\rangle\downarrow -2|z\rangle\uparrow \\
|u^{3/2}_{-1/2}\rangle &= \frac{1}{\sqrt{6}}|x-iy\rangle\uparrow +2|z\rangle\downarrow
\end{aligned} \tag{3.5}$$

Of note is the fact that under confinement the LH band becomes split from the HH band, this fact will become important when we discuss QDs since they are a highly confined system in three dimensions. For now we will continue the discussion of QDs by discussing the growth process and then optical coupling. The background we have developed in this section will become important when discussing the interaction of light with semi-conductors and specifically QDs

3.3 QD Growth

The InAs/GaAs QDs studied in this thesis are created in the Stranski-Krastanov (SK) growth mode via molecular beam epitaxy (MBE). The 7% lattice mismatch between the InAs and GaAs enables islands to form due to strain effects at the interface. A key aspect of the SK growth mode is that as the InAs is deposited on the GaAs substrate it will adapt to the GaAs lattice constant creating a thin layer (wetting layer). Once the wetting layer has reached a critical thickness, the intrinsic lattice constant of InAs dominates and pancake-like islands begin to form (figure 3.2). The islands are finally capped with GaAs and form the three dimensional confinement. The adaptation of the InAs lattice constant across the dot gives rise to

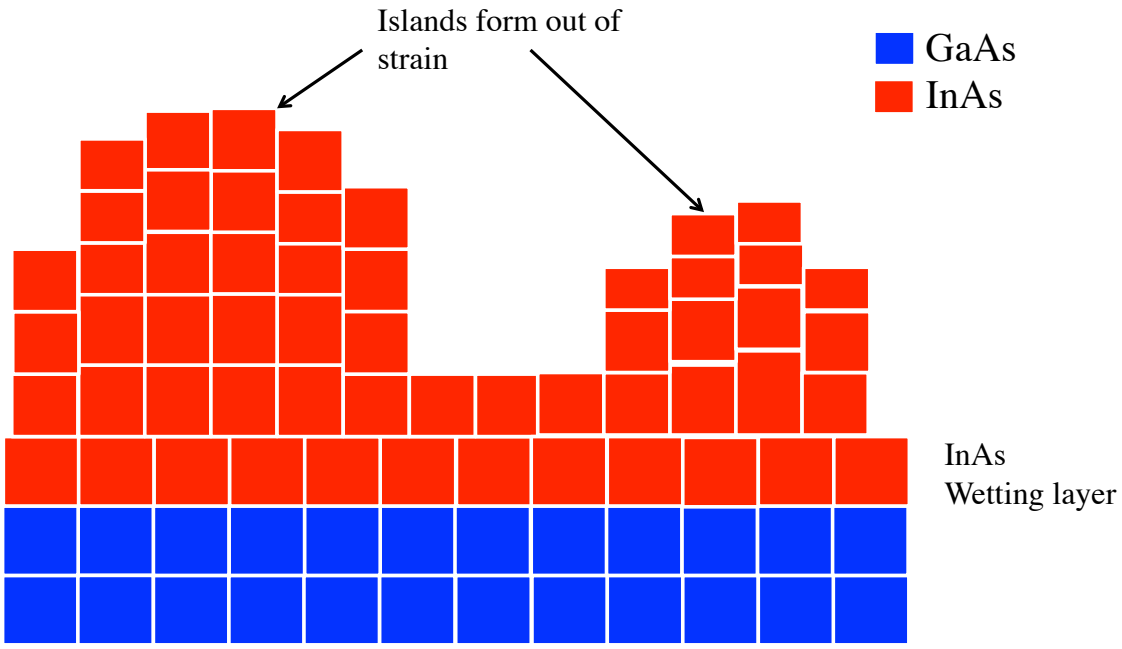

Figure 3.2: The Stranski-Krastanov (SK) growth mode involves depositing a thin layer of InAs atop a GaAs substrate; at first the InAs adapts to the GaAs lattice constant but as more is InAs is deposited the strain causes pancake-like islands to form.

large strain effects that shift the energy of the QD structure. So the total energy now contains contributions from many interactions: strain, confinement, InAs bandgap, and exciton binding energy. From our own measurements on these structures we have determined the QD energy distribution to be centered around 1.3eV, and the bandgap and exciton binding energy are known to be roughly 0.35eV. This means that the confinement and strain play a major role in determining the energy of these QD structures.

The samples studied in this thesis are embedded in a diode structure (either Schottky or PIN). The purpose this serves is to allow for selective charging of the QD. By applying a voltage across the QD region the valence and conduction bands will be altered as a function of bias. When sufficient bias is applied the lowest energy state of a single QD will fall below the Fermi level and it is then energetically favorable

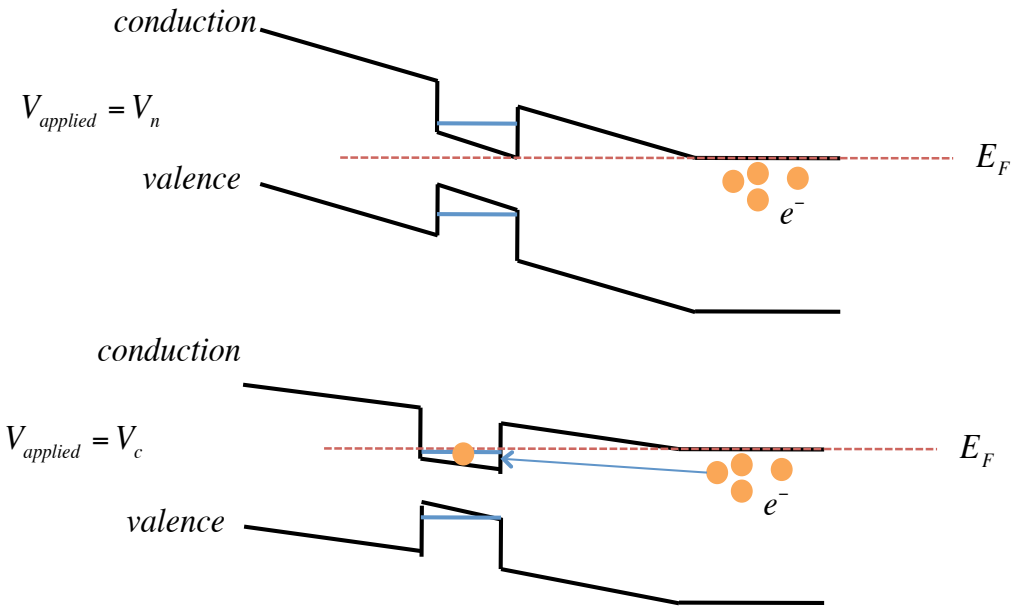

Figure 3.3: In a diode structure the gate voltage applied across the sample alters the conduction and valence band with respect to the Fermi level. When a specific charging voltage is applied, V_c, the lowest energy state of the QD falls below the Fermi level and an electron can tunnel into the dot creating a negatively charged dot

for an electron from the n-doped GaAs substrate to tunnel into the QD. A cartoon of this process is given in figure 3.3. With a single electron confined to the QD we now have a single qubit ground state (the spin state of the electron will serve as this qubit) making a singly charged QD, X^-, a viable system for quantum computing architectures. One of the most attractive aspects of the charged QD is its coupling to light via creation of excitons (electron-hole pairs), which is discussed in section IV. First we should take some time to describe the two types of samples used in this work.

3.3.1 Schottkey Diode Sample

The sample used for most of the work in the first part of the thesis consists of single self-assembled QDs embedded in a Schottky diode heterostructure shown in

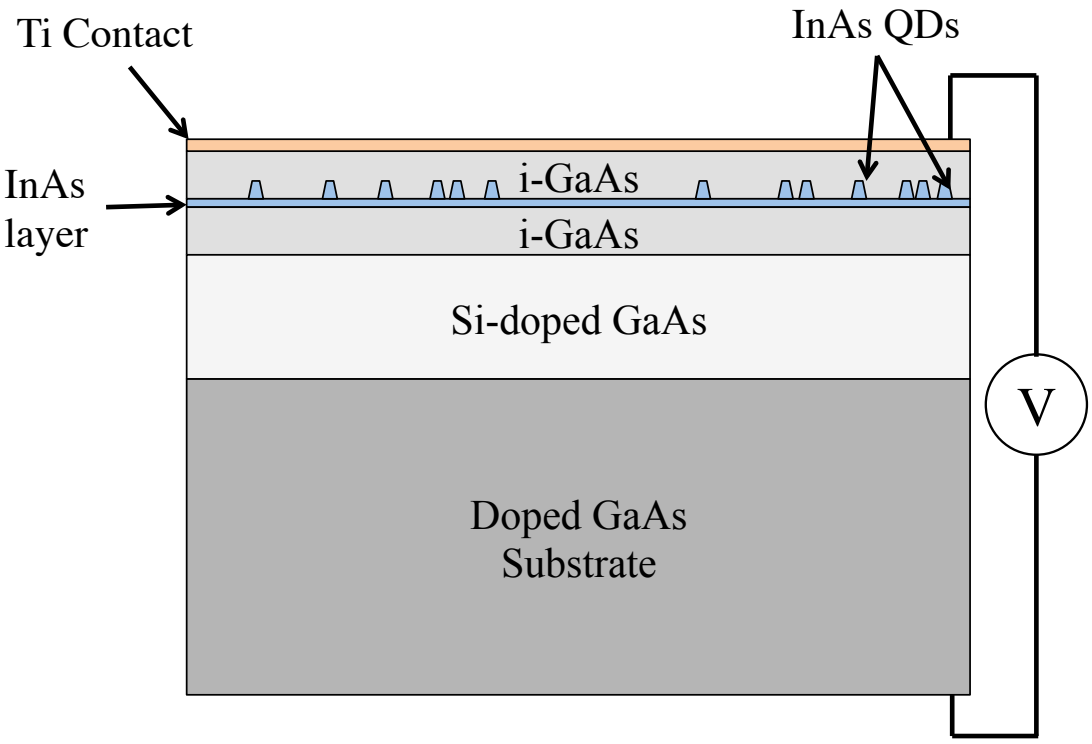

Figure 3.4: The Schottky diode structure provides a mechanism to selectively charge the QDs with single electrons. The doped GaAs substrate

figure 3.4. The sample consists of a bottom layer of doped GaAs substrate that will form the bottom contact for the Schottky diode. Next a Si(n)-doped layer provides the electrons that can tunnel into the dot creating a negatively charged QD state. On top a 40nm layer of intrinsic GaAs is grown before the InAs layer is grown. The InAs dot layer is typically between 2-3nm and is capped by a 280nm layer of intrinsic GaAs. The top Schottky is created using a final layer of Ti (∼5nm). The doping concentration used is $\sim 10^{18} cm^{-3}$, which gives a high concentration needed to inject electrons into QD structures under appropriately applied gate voltage across the diode.

As said this sample is used in the beginning part of the thesis and will be indicated when used. There are two main drawbacks to this sample structure; the titanium top contact is only semi-transparent due to its small thickness and this causes absorption

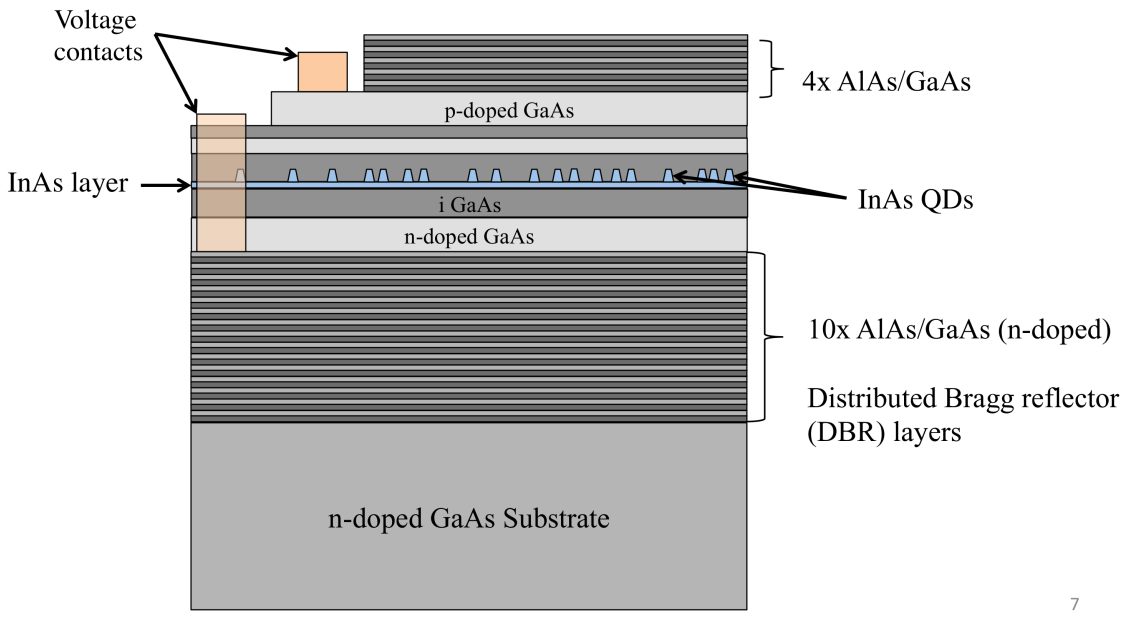

Figure 3.5: The DBR layers directly behind the QD layer reflect radiation back and allow us to collect more of the emitted or scattered light from the QD. Improved light collection make more complicated photon counting experiments possible.

at the surface both for incident radiation and scattered or emitted radiation from the QD. Also, radiation into the GaAs substrate can be lost in the material easier. The next sample design uses mirrors just below the QD layer to direct radiation out of the top of the sample so it does not have to pass through the 0.5mm thick substrate with high probability of loss. More will be discussed about this sample in the next section.

3.3.2 PIN Diode Sample with Bragg Mirror for Increased Light Collection

During the later parts of this work it will become necessary to employ a sample with better light collection than the usual Schottky diode structure. To accomplish this layers of a distributed Bragg reflector (DBR) are grown just below the QD layer to direct radiation back through the top of the sample. The doped substrate is essentially

the same as before with identical doping concentration for charging. However, now the alternating layers of aluminum arsenide (AlAs) and GaAs are deposited to form the bottom distributed Bragg reflector (DBR) layers; in particular, 10 periods are used with alternating size of 82nm/69nm (AlAs/GaAs). Additionally, these layers are n-doped to provide electrons for QD charging. On top of the DBR layers is a 96nm of n-doped GaAs which forms the negative part, or bottom contact, of the PIN diode. Then a layer of intrinsic GaAs (40nm) is grown to provide the base of the InAs QD layer. The InAs layer is next and its growth procedure is identical to the previous sample and is capped by another layer of intrinsic GaAs (66nm). These intrinsic layers along with the dot layer form the "I" part of the PIN diode. There is actually another layer of n-doped GaAs (10nm) and intrinsic GaAs (40nm) before the final p-doped GaAs (40nm) layer is grown to complete the diode. The reason for this extra layer is to decrease the electric field at the QD layer so we can work at a manageable voltage ($\sim$0-1V) and avoid drawing too much current, which can lead to local heating effects, so perhaps it is more accurate to call this a PININ diode. A final set of four un-doped DBR layers completes the sample and provides us with a weak cavity with about a 15nm width, giving us a Q-factor of $\sim$63. We see a slight enhancement in counts, but Purcell effects have yet to be observed.

The placement of the contacts is extremely important for the stability of this sample. Many earlier version included Schottky diode structures where we would observe the QD resonances shift in energy on the order of minutes. The belief was that charges were becoming trapped in the DBR layers since the diode applied an electric field across the entire sample. So to try and avoid this problem a PIN diode structure was introduced where the voltage contacts would be etched down to the appropriate layer so that only the QD layer was subjected to the applied bias and not the entire sample (seen in figure 3.5). Under these conditions we were able to show stability of QD resonances and increased collection, which will be shown in the form

of data later in the thesis.

A tremendous amount credit and gratitude goes to Allan Bracker and Dan Gammon at the Naval Research Lab (NRL). They have been working on this sample design for some time and have worked very closely with our lab to determine the parameters that work and give the best results. We are grateful to them for their hard work. Without the improvements over the Schottky diode sample, the newer generation of experiments using QDs causing unfeasible integration times to get the proper statistics for a measurement.

3.4 Optical coupling of QD states

To begin the discussion of optical coupling to QDs we will discuss briefly excitons in bulk. Incident radiation with energy at or above the bandgap can promote an electron from the valence band into the conduction band leaving behind a hole. For the case where the exciton is extended over many lattice sites we use the band edge electrons and holes to describe the excitonic dynamics [76]. These are known as Wannier-Mott excitons. The other type of exciton is called a Frenkel exciton which only extends to a few lattice sites. The theory for Frenkel excitons requires a full treatment of the bandstructure and is not within the scope of this work. The Coulomb interaction attracts the positive holes to the negative electrons and appears as a potential term in the Hamiltonian for the electron-hole system. The Mott excitons can be described using effective mass theory where we write the Schrödinger equation,

$$\left(-\frac{\hbar^2}{2m_e^*}\nabla_e^2 - \frac{\hbar^2}{2m_h^*}\nabla_h^2 - \frac{e^2}{4\pi\epsilon|r_e - r_h|}\right)\Psi = E\Psi. \tag{3.6}$$

Here Ψ is is given by the Bloch states derived from the periodic nature of the crystal,

$$\Psi = e^{i\mathbf{k}\cdot\mathbf{r}}u_{\mathbf{k}}(\mathbf{r}), \tag{3.7}$$

where $u_k(r)$ has the periodicity of the lattice. This two body problem can be distilled to a one body problem mimicking the hydrogen atom Hamiltonian and solved in the same way [77]. By rewriting the one-body Hamiltonian we can solve Schrödinger's equation for the two distinct parts giving us a plane wave solution and a hydrogen like solution

$$H = \overbrace{\frac{\hbar^2 K^2}{2(m_e^* + m_h^*)}}^{\text{plane wave solutions to SE}} + \underbrace{\frac{\hbar^2 k^2}{2m_r^*} - \frac{e^2}{4\pi|\mathbf{r}|}}_{\text{hydrogen-like solutions to SE}} \tag{3.8}$$

where,

$$\begin{aligned} \mathbf{k} &= \frac{m_e^* \mathbf{k}_e + m_h^* \mathbf{k}_h}{m_e^* + m_h^*} \\ \mathbf{r} &= \mathbf{r}_e - \mathbf{r}_h \\ \mathbf{K} &= \mathbf{k}_e - \mathbf{k}_h \end{aligned}$$

The plane wave solution is given by,

$$\phi(\mathbf{R}) = e^{i\mathbf{K}\cdot\mathbf{R}} \tag{3.9}$$

with,

$$\mathbf{R} = \frac{m_e^* \mathbf{r}_e + m_h^* \mathbf{r}_h}{m_e^* + m_h^*}.$$

The exciton hydrogen-like envelope functions look like,

$$\psi_{100}(\mathbf{r}) = \frac{1}{\sqrt{\pi a_e}} e^{-\mathbf{r}/a_e} \tag{3.10}$$

Here a_e is the exciton Bohr radius and it varies from the usual a_0 according to the effective mass. The a_e for these materials ranges from 10-50 nm. Also, from this approach binding energies for the exciton arise and what we observe is that the typical binding energy is around 5meV. Recalling that kT at room temperature is 25 meV,

we can clearly see why these systems must be studied at liquid helium temperatures, which is still 0.4 meV.

The techniques used in the next section to derive the selection rules for transitions will be more like the techniques used in atomic physics using a matrix element approach, but it is instructive to keep in mind the discussion of the exciton since it is what gives rise to the optical coupling in the QD systems.

3.4.1 Selection Rules at Zero magnetic field

From section 3.2 we determined that the electronic bands obey the symmetry of the point group at $k = 0$, and since these are direct bandgap semiconductors we will use the angular momentum formalism to calculate the selection rules for QD transitions. In section 3.3 we introduced a negatively charged QD, a single electron confined to the ground state, and this will be the system of investigation for the remainder of the thesis. With this in mind let us calculate the selection rules for a singly charged QD at zero magnetic field.

For the purposes of this discussion it is sufficient to assume a semi-classical picture where the electric field interacting with the dot is given by,

$$\mathbf{E}(t) = \mathbf{E}cos(kz - \omega t), \tag{3.11}$$

with z as the propagation direction anti-parallel to the crystal growth axis. The semi-classical Hamiltonian for interactions of radiation with an electron in the effective mass approximation is given by,

$$H_{em} = \frac{(\mathbf{p} - e\mathbf{A})^2}{2m_e^*} + V(r). \tag{3.12}$$

Here we have chosen to work in the Coulomb gauge, with $\mathbf{A}$ as the vector potential. All of the rich semiconductor physics, such as confinement, that we discussed in

section 3.2 has been swept into the $V(r)$ term and we will consider the additional terms as perturbations to the original eigenstates.

$$H_{tot} = \overbrace{\frac{\mathbf{p}^2}{2m_e^*} + V(r)}^{H_0} \underbrace{- \frac{e}{m_e^*}\mathbf{p}\cdot\mathbf{A}}_{H_I} + \overbrace{\cancel{\frac{e^2}{2m_e^*}\mathbf{A}^2}}^{\text{neglect } 2^{nd} \text{ order}} \tag{3.13}$$

The $\mathbf{p}\cdot\mathbf{A}$ can be rewritten in a more convenient form using the dipole moment, $\mu = -e\mathbf{r}$, and the electric field,

$$H_I = \mu \cdot \mathbf{E} = -e\mathbf{r}\cdot\mathbf{E} \tag{3.14}$$

Since our goal is to find the allowed transitions in a single charged QD we should look at the configuration of the ground and excited states. We start with an single electron in the conduction band and a full valence band. An exciton (electron-hole pair) is created when the system interacts with an optical field of sufficient energy. The three particles now form a system we call a trion. An example of the electron and hole configuration is given in figure 3.6. The two electrons in the conduction band will have opposite spin leaving the hole spin as the angular momentum carrier. As we saw before the conduction band states behave as s-like atomic orbitals and the valence band states as p-like atomic orbitals. To calculate the selection rules we will use the Wigner-Eckart theorem so describing both $\mathbf{r}$ and $\mathbf{E}$ in terms of their spherical components is an important first step,

$$\begin{aligned} r_{\pm 1} &= \mp\frac{x \pm iy}{\sqrt{2}} \\ r_0 &= z \end{aligned} \tag{3.15}$$

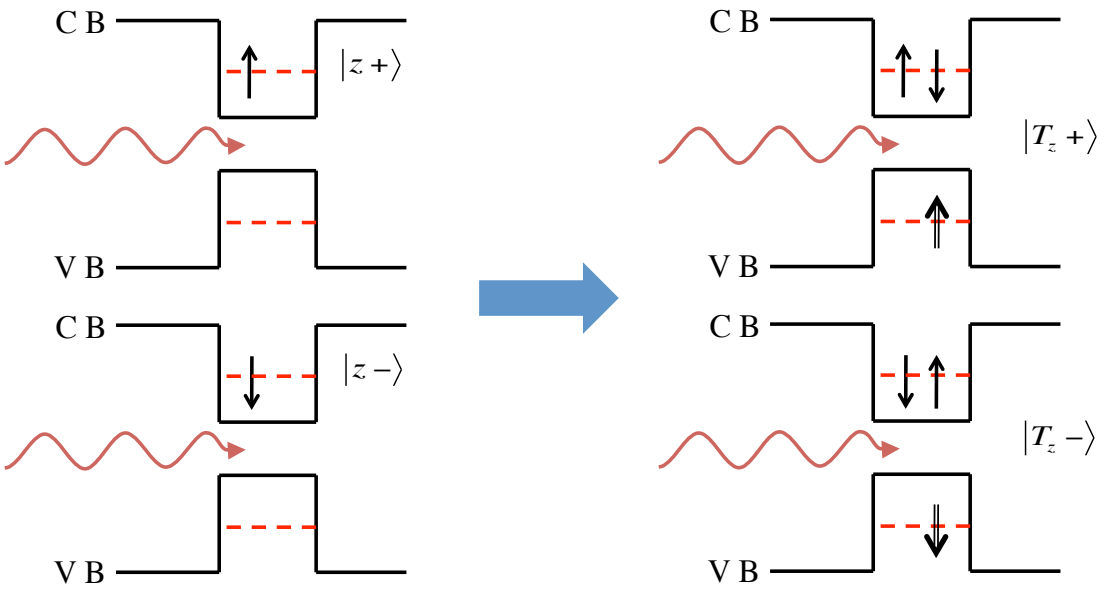

Figure 3.6: Upon excitation an electron from the valence band is promoted to the conduction band leaving behind a hole. The two conduction band electrons and the valence band hole form the trion excited state$|T_z\pm\rangle$, where the $\pm$ indicates the direction of the hole spin. Due to Pauli exclusion the two electrons in the conduction band will have opposite spin making the hole spin the dominant angular momentum

and we look at the polarization vectors when considering the electric field,

$$\begin{aligned} \mathbf{E} &= E_0\epsilon_{\mathbf{0}} - E_{+1}\epsilon_{-1} - E_{-1}\epsilon_{+1}, \qquad (3.16) \\ \text{where,} & \\ \epsilon_{\pm 1} &= \mp\frac{\hat{\mathbf{x}} \pm i\hat{\mathbf{y}}}{\sqrt{2}} \\ \text{and,} & \\ \epsilon_0 &= \hat{\mathbf{z}}. \end{aligned}$$

Now we represent the ground states and trions states in terms of angular momentum, $|j, m_j\rangle$,

$$\begin{aligned} |z\pm\rangle &= \left|\frac{1}{2}, \pm\frac{1}{2}\right\rangle, \\ |T_z\pm\rangle &= \left|\frac{3}{2}, \pm\frac{3}{2}\right\rangle. \qquad (3.17) \end{aligned}$$

Now to find the allowed transitions we look at the matrix elements for transitions from the ground state to the excited state.

$$\langle T_z+| - e\mathbf{r}\cdot\mathbf{E}|z+\rangle = \left\langle \frac{3}{2}, +\frac{3}{2}\right| r_0E_0\epsilon_0 - r_{-1}E_{-1}\epsilon_{+1} - r_{+1}E_{+1}\epsilon_{-1} \left|\frac{1}{2}, +\frac{1}{2}\right\rangle \qquad (3.18)$$

From Wigner-Eckart we are left with one non-vanishing Clebsch-Gordon coefficient,

$$\left\langle \frac{3}{2}\right\| er \left\|\frac{1}{2}\right\rangle \left\langle \frac{1}{2}, 1, +\frac{1}{2}, +1|\frac{3}{2}, +\frac{3}{2}\right\rangle E_{-1}\epsilon_{+1} \qquad (3.19)$$

And the reduced matrix element gives us the strength of the dipole interaction. Here we can plainly see that only ϵ_{+1} polarized light couples the $|z+\rangle \rightarrow |T_z+\rangle$. Similarly

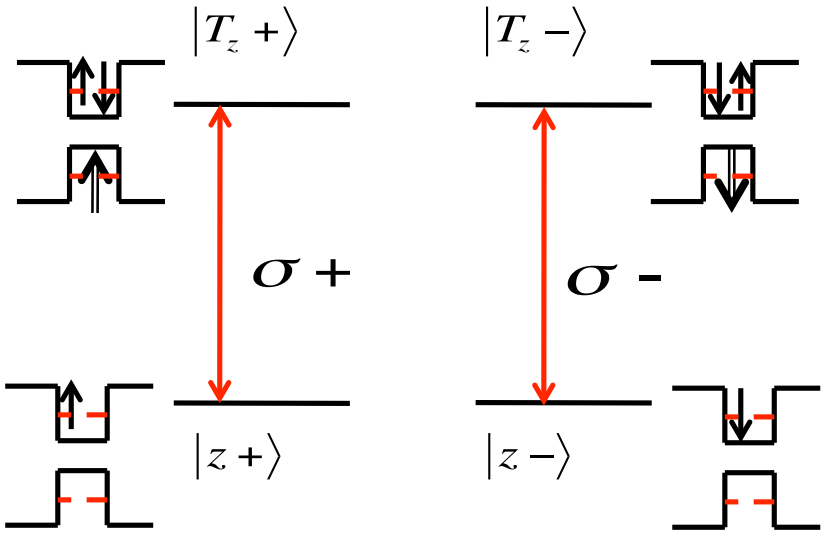

Figure 3.7: From the derived selection rules only circularly polarized light couple the transitions and the cross transitions are forbidden at zero magnetic field. Cartoons of the band diagram are shown beside each transition to show the configuration in the conduction and valence band

we can write down the matrix elements for the other possible transitions

$$\begin{aligned}
\langle T_z-|-e\mathbf{r}\cdot\mathbf{E}|z-\rangle &= \left\langle \frac{3}{2}\middle\| er \middle\|\frac{1}{2}\right\rangle \left\langle \frac{1}{2},1,-\frac{1}{2},-1\middle|\frac{3}{2},-\frac{3}{2}\right\rangle E_{+1}\epsilon_{-1} \\
\langle T_z-|-e\mathbf{r}\cdot\mathbf{E}|z+\rangle &= 0 \\
\langle T_z+|-e\mathbf{r}\cdot\mathbf{E}|z-\rangle &= 0
\end{aligned}$$

Therefore, we have shown that only circularly polarized light couples the trion transitions at zero magnetic field and by recalling that $\sigma\pm = \mp\epsilon_{\pm 1}$, we can draw the selection rules for this system and shown in figure 3.7

At zero magnetic field the electron states are degenerate making it hard to store information in the spin state since there is no discernible difference between the two. We could apply a magnetic field in the growth direction (Faraday geometry), but the selction rules would remain unchanged since the axis of quantization is the same as at zero field. So, the forbidden cross-transitions makes it impossible for us to transfer

population from one to the other via the excited states. The goal would be for us to mix these states and transitions while also splitting the electron energy. The way we do this is by applying a transverse magnetic field (the Voigt geometry) that changes the axis of quantization, thereby mixing the zero field ground and excited states. In the next section we determine the selection rules for our system under such conditions.

3.4.2 Selection Rules in the Voigt Geometry

In the previous section we discussed the optical coupling to the QD system and introduced the concept of a singly charged QD. The selection rules for the trions states were derived, however one missing element was the ability to manipulate the spin state. We will see that using a magnetic field in the Voigt geometry, changes the axis of quantization thereby mixing the z-basis states allowing for cross transitions to exist.

The Hamiltonian for the applied magnetic field $B = B\hat{x}$ is the same Zeeman Hamiltonian we are accustomed to, only now we have both electron and hole spins to take into account. The new Hamiltonian is,

$$H_B = g_e \mu_B \mathbf{B} \cdot \hat{S}_e - g_h \mu_B \mathbf{B} \cdot \hat{S}_h \tag{3.20}$$

with g_e and g_h as the electron and hole g factors, respectively, and μ_B is the Bohr magneton. We can easily see the mixing of the states by writing the Hamiltonian in the z-basis,

$$H_B = \begin{array}{c} \\ \langle z+| \\ \langle z-| \\ \langle T_z+| \\ \langle T_z-| \end{array} \begin{array}{c} \begin{array}{cccc} |z+\rangle & |z-\rangle & |T_z+\rangle & |Tz-\rangle \end{array} \\ \begin{pmatrix} 0 & \frac{1}{2}\hbar g_e \mu_B B & 0 & 0 \\ \frac{1}{2}\hbar g_e \mu_B B & 0 & 0 & 0 \\ 0 & 0 & 0 & -\frac{1}{2}\hbar g_h \mu_B B \\ 0 & 0 & -\frac{1}{2}\hbar g_h \mu_B B & 0 \end{pmatrix} \end{array} \tag{3.21}$$

When we solve for the new electron eigenstates and eigenenergies are,

$$\begin{aligned} |x\pm\rangle &= \frac{|z+\rangle \pm |x-\rangle}{\sqrt{2}} \\ E_{x\pm} &= \pm\frac{1}{2} g_e \mu_B B \end{aligned} \tag{3.22}$$

Similarly for the trion states,

$$\begin{aligned} |Tx\pm\rangle &= \frac{|T_z+\rangle \pm |T_x-\rangle}{\sqrt{2}} \\ E_{T_{x\pm}} &= \mp\frac{1}{2} g_h \mu_B B \end{aligned} \tag{3.23}$$

Now all that is left is to calculate the new selection rules in the Voigt geometry using our new eigenstates. This follows that same basic premise as the calculation done in section 3.4.1 using Eqns. 3.14 and 3.18, only now the transitions we are looking for are the linear combinations of the old z-basis eigenstates. Since we have already determined the z-basis matrix elements, the extensions is somewhat trivial as shown below,

$$\begin{aligned} \langle T_x+| - e\mathbf{r}\cdot\mathbf{E}|x-\rangle &= \frac{-1}{2}\left[\left\langle\frac{3}{2},+\frac{3}{2}\right| + \left\langle\frac{3}{2},-\frac{3}{2}\right|\right] e\mathbf{r}\cdot\mathbf{E}\left[\left|\frac{1}{2},+\frac{1}{2}\right\rangle - \left|\frac{1}{2},-\frac{1}{2}\right\rangle\right] \\ &= \frac{-1}{2}\left[\left\langle\frac{3}{2},+\frac{3}{2}\right| e\mathbf{r}\cdot\mathbf{E}\left|\frac{1}{2},+\frac{1}{2}\right\rangle - \left\langle\frac{3}{2},+\frac{3}{2}\right| e\mathbf{r}\cdot\mathbf{E}\left|\frac{1}{2},-\frac{1}{2}\right\rangle\right] \\ &- \frac{1}{2}\left[\left\langle\frac{3}{2},-\frac{3}{2}\right| e\mathbf{r}\cdot\mathbf{E}\left|\frac{1}{2},+\frac{1}{2}\right\rangle - \left\langle\frac{3}{2},-\frac{3}{2}\right| e\mathbf{r}\cdot\mathbf{E}\left|\frac{1}{2},-\frac{1}{2}\right\rangle\right] \end{aligned}$$

These matrix elements are exactly the same as we calculated before, so we can simply use the results from 3.18 and just using the polarization notation the allowed

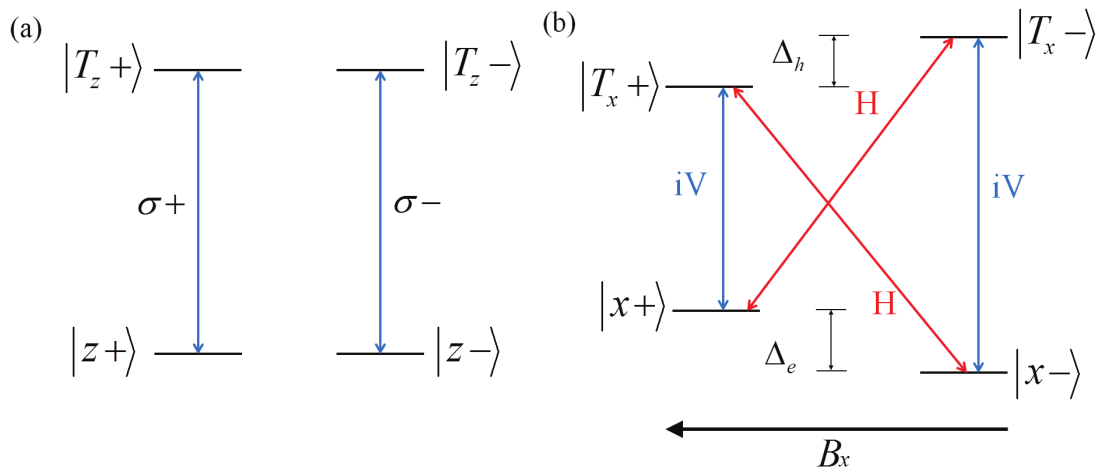

Figure 3.8: (a) The degenerate two-level system at zero magnetic field showing circularly polarized selection rules and forbidden cross-transitions. (b) The introduction of a transverse magnetic field gives acts to mix the z-basis ground and excited states and converts the circular polarization selection rules into linear ones. Furthermore, this system leaves us with a well defined qubit ($|x+\rangle$ and $|x-\rangle$), and the ability to transfer population from one spin state to the other by utilizing the now optically accessible trion states.

transitions become,

$$\begin{aligned}
\langle T_x + |e\mathbf{r}\cdot\mathbf{E}|x-\rangle &\sim -\epsilon_{+1} + \epsilon_{-1} \sim \hat{\mathbf{x}} \\
\langle T_x + |e\mathbf{r}\cdot\mathbf{E}|x+\rangle &\sim -\epsilon_{+1} - \epsilon_{-1} \sim i\hat{\mathbf{y}} \\
\langle T_x - |e\mathbf{r}\cdot\mathbf{E}|x-\rangle &\sim -\epsilon_{+1} - \epsilon_{-1} \sim i\hat{\mathbf{y}} \\
\langle T_x - |e\mathbf{r}\cdot\mathbf{E}|x+\rangle &\sim -\epsilon_{+1} + \epsilon_{-1} \sim \hat{\mathbf{x}}
\end{aligned} \tag{3.24}$$

The $\hat{\mathbf{x}}$ and $\hat{\mathbf{y}}$ vectors correspont to horizontally (H) and vertically (V) polarized transitions, respectively. The final four level diagram that we will use for the remainder of our magnetic field studies is shown in figure 3.8.

Now we we are working in a system with cross transitions, which allow us to transfer population from one spin state to the other. Also, the splitting of the ground state spin gives us a well defined qubit in the form $|x+\rangle$ and $|x-\rangle$. The remainder of

the thesis will build up our ability to coherently manipulate the spin state. We will show entanglement between a photon emitted from the QD and the spin state as well as outline a new experiment to teleport information from another source onto the the QD spin state, which utilizes the entangled photon.

3.5 Conclusion

This chapter served to introduce the theoretical background for semiconductor QDs to provide some context as we move forward. We described the band structure of the bulk materials in QDs and their optical properties. These properties extend to the QD and we used that theoretical framework to determine the allowed optical transitions in InAs QDs. Finally we showed that under a transverse magnetic field we can create a spin qubit and use optical trion transitions to move between spin states. The later chapters will focus heavily on the optical techniques we employ to manipulate the spin states.

CHAPTER IV

Optical Investigation of Single QDs

4.1 Introduction

The selection rules for both the neutral and trion systems derived in the previous chapter give rise to allowable paths for manipulation of the QD ground and excited states. Many quantum computing protocols require optical initialization, rotation and readout of single spins and in the case of the trion system we see that this can be accomplished by exploiting the derived energy level structure[2, 88, 66, 45]. This chapter discusses the frequency domain and time domain optical techniques used to identify QDs. Spectrally resolving the luminescence from a QD sample, after it has been excited with a laser tuned above the band-gap, identifies individual QDs present in our field of view. Narrow linewidth continuous wave (CW) lasers probe the individual transitions to determine the energy of the state and the linewidth associated with the transition. Pulsed lasers or time gated CW lasers are used to study the time dynamics of QD transitions and also to manipulate the QD electron spin. This chapter will cover the discovery and characterization of single QDs and evolve to discuss how spin manipulations are carried out.

4.2 Geometry of Optical Excitation

We begin by discussing how the laser field is made to interact with the QD sample. As was discussed in chapter III, the QD samples are embedded in a diode structure that allows tuning of the conduction and valence band relative to the fermi level. At the appropriate applied bias an electron can tunnel into the QD and become confined, giving rise to a trion system under excitation. To optically excite the system we use a high numerical aperture lens, bolted to the sample to ensure that the sample-lens system remains rigid while cooling to liquid Helium temperatures. The lens (Thorlabs 354330-B) has a focal length of 3.1mm and a numerical aperture of 0.68 creating a tight, 1μm, beam spot. The dot fluorescence can then be collected by the focusing asphere (the reflection geometry) or another asphere can be placed on the back of the sample to collect the forward fluorescence (the transmission geometry). The sample-asphere system can be seen in figure 4.1.

4.3 Photoluminescence Spectroscopy

The most versatile approach to identifying QD charge states and resonant energies in a given field of view would be to "turn on" all of the QDs in that region and collect the light emitted from each of these using a spectrometer. Collecting the emission from the QDs as a function of applied bias to the sample shows the energy of the different charge states. The 'turning on" of the QD transitions is achieved by exciting the sample above the QD band gap (discussed in chapter III) thereby injecting carriers (electrons and holes) into the bulk. The carriers non-radiatively decay to the Γ point where they then radiatively recombine at the specific QD charge state resonance energy; this technique is known as photoluminescence (PL) spectroscopy. A 920nm long-pass filter is placed before the spectrometer to remove the excitation laser light so as not to saturate the spectrometer and only let through the light coming from the

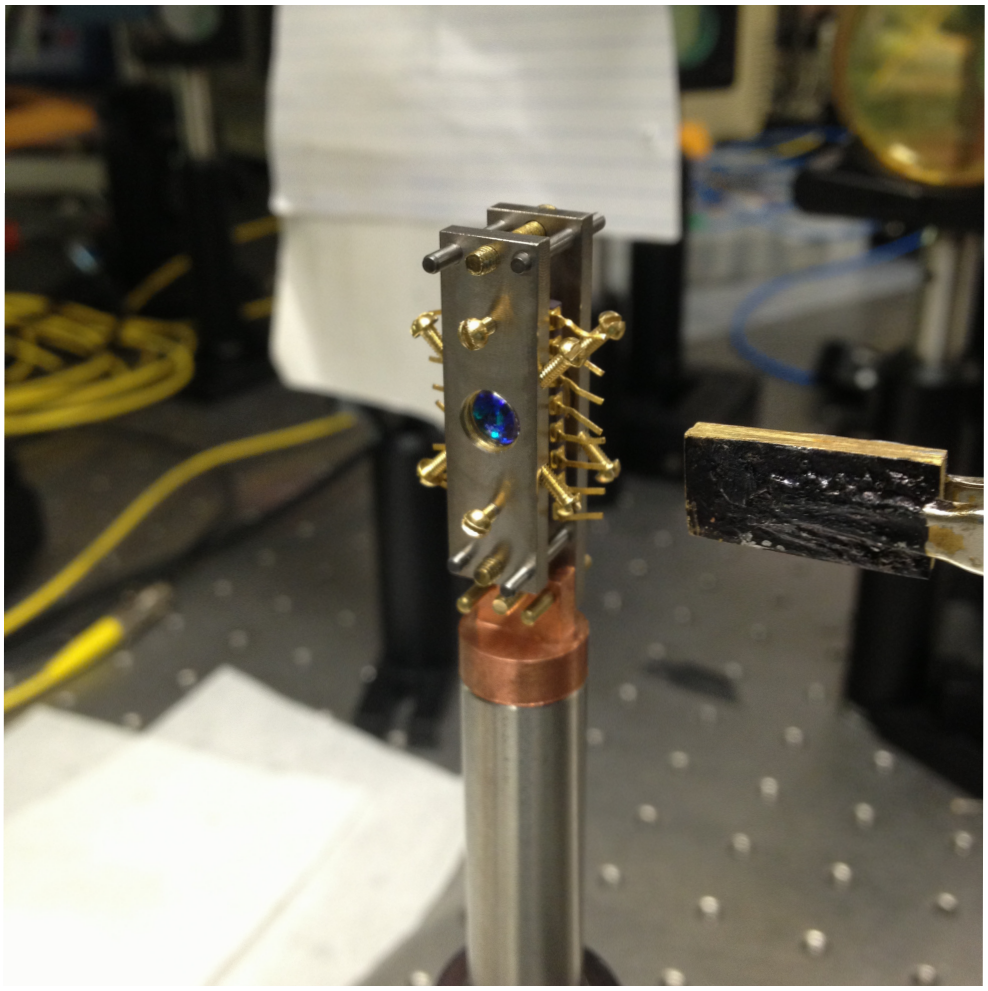

Figure 4.1: The asphere-sample mounting scheme. The aspheres are held in place on either end of the ceramic sample mount by titanium mounts. The mounts are rigidly clamped to the sample by using fine threaded set screws that also act as a fine tuning of the asphere focus. Additionally, there are 4 set screws on the edge of the mount holding the lens in place and allow us to excite different regions of the samples. The usage of brass set screws and titanium lens mounts is done to avoid changes in alignment when a magnetic field is applied.

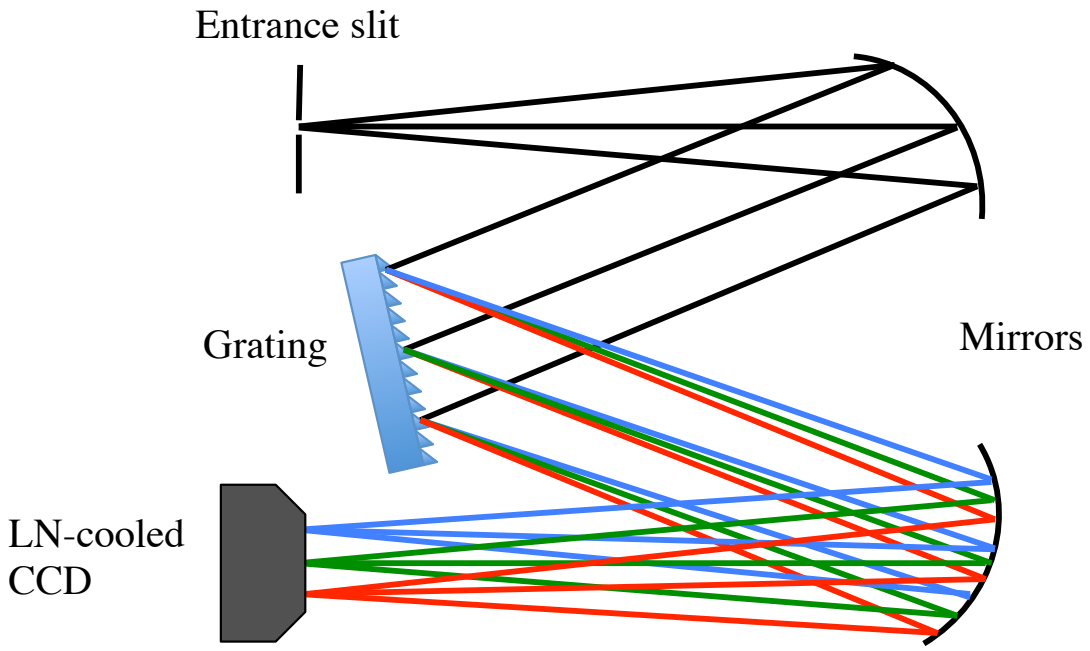

Figure 4.2: A typical diagram of a single grating spectrometer. The light is separated by the grating and focused on to a liquid nitrogen cooled CCD

QD transitions.

The spectrometer used for these PL measurements is a HR640 single grating spectrometer with a 1200 groves per mm (g/mm) grating. After the light is separated into frequency components by the grating it is focused on to a charge-coupled device (CCD) camera with 1024 pixel resolution. A schematic of this set-up is provided in figure 4.2. A capture of the CCD is taken at different biases and integrated together in a 3 dimensional plot where the deterministic charging is observed. An example of a single spectrum is seen in figure 4.3, and a 3D plot showing the charging of the different QD states is provided in figure 4.4.

PL is an excellent technique for the early characterization of QD transitions and charge states but for the purposes of coherent spectroscopy and control it is somewhat lacking. For more precise measurement and control of the QD transitions we move to resonant CW excitation and readout. Using narrow linewidth CW lasers to probe

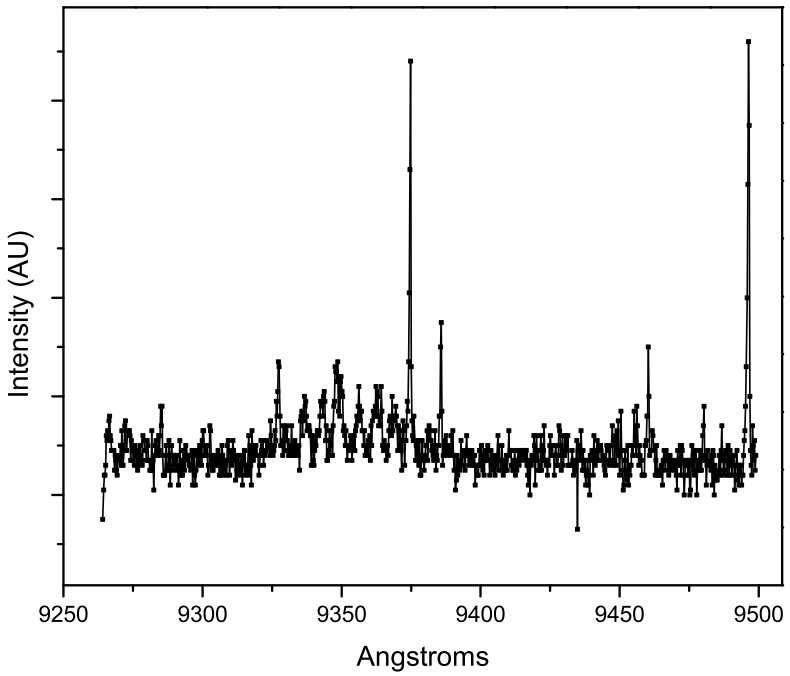

Figure 4.3: A single spectrum taken using the CCD and the HR640 spectrometer. The single peaks observed over the background are the individual QD resonances separated in wavelength. The dots are excited with a laser tuned just above the band gap ($\sim$ 890nm) and the excitation laser is filtered out using a 920nm long-pass filter leaving only the luminescence from the excited QDs

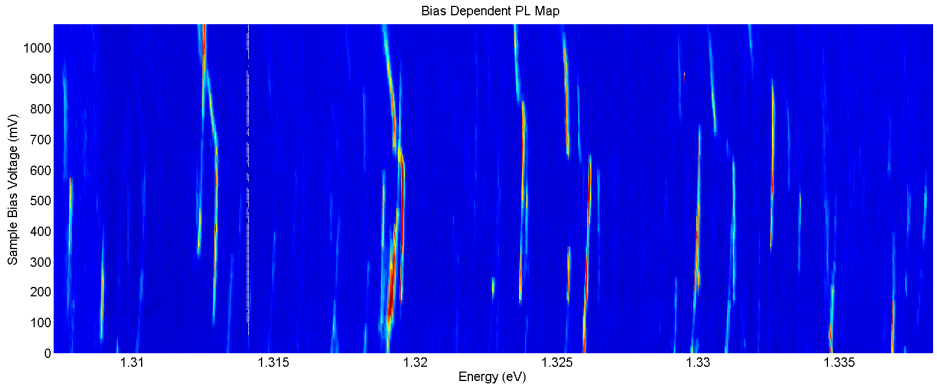

Figure 4.4: A bias dependent PL map. We can see as the gate voltage is tuned charge states will turn on and off. There is a $\sim$ 6meV difference between the neutral exciton X^0 and the negative exciton state, trion, X^{-1}. This serves as a guide to where the trion state should be in bias and voltage but complete confirmation of the state comes from resonant excitation experiments.

transitions we can extract more information about the QD optical transitions.

4.4 Resonant Optical Interactions with a Two Level System

Before we can discuss the techniques used in resonant excitation of a QD we must first develop the theoretical framework for optical interactions. For simplicity we will take the case of a resonant laser interacting with a two-level system, which is the zero magnetic field structure for a trion system. We use a semi-classical approach to solve for the steady state dynamics of an ideal system under resonant excitation. We can start in the field interaction representation and write the Hamiltonian for this system under influence of a semi-classical radiation field in the rotating-wave approximation (RWA)[7].

$$\tilde{H(t)} = \begin{pmatrix} -\frac{\delta}{2} & \chi(t)^* \\ \chi(t) & \frac{\delta}{2} \end{pmatrix} \tag{4.1}$$

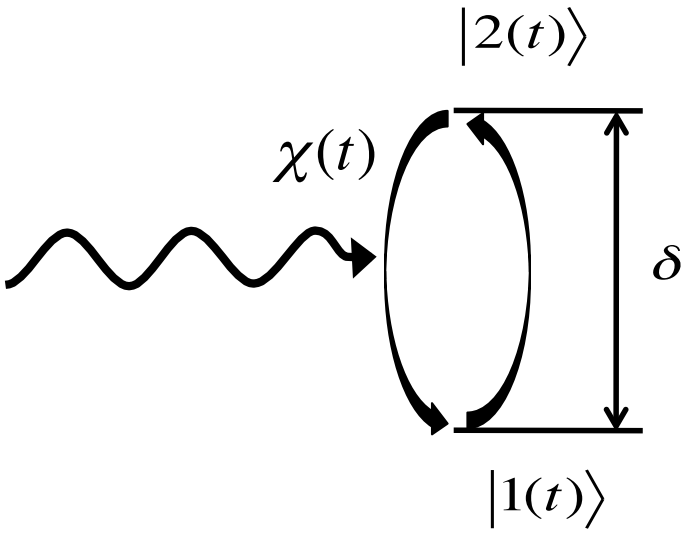

Figure 4.5: A sample 2 level system in the field interaction picture where χ is the Rabi frequency and $\delta = 0$ indicates that the radiation field is on resonance with the transition.

Here $\delta = 0$ corresponds to resonant excitation and χ is the Rabi frequency given by,

$$\chi(t) = \frac{\mu E_0(t)}{2\hbar} \tag{4.2}$$

A graphical description of the two level system is provided in figure 4.5.

The discussion follows the from that found in Ref[7]. It is useful to discuss coupling of a radiation field to a 2 level system using the density matrix formalism. If we have a hermitian operator $\mathbf{O}$, we can look for the expectation value of $\mathbf{O}$ given an arbitrary state $|\psi(t)\rangle$. We find that by representing $|\psi(t)\rangle$ using a linear combination of basis kets $\sum_n a_n(t)|n\rangle$ the expectation value becomes,

$$\langle\psi(t)|\mathbf{O}|\psi(t)\rangle = \sum_{n,m} a_m^*(t)a_n(t)\langle m|\mathbf{O}|n\rangle \tag{4.3}$$

The density matrix, $\rho(t)$ is made up of elements $a_n(t)a_m^*(t)$ so, $\rho(t) = |\psi(t)\rangle\langle\psi(t)|$.

Now the expectation value of $\mathbf{O}$ becomes,

$$\langle\psi(t)|\mathbf{O}|\psi(t)\rangle = \mathrm{Tr}[\rho(t)\mathbf{O}]. \tag{4.4}$$

In the field interaction picture we can now write solutions for the density matrix elements for our 2 level system by using,

$$\tilde{\rho} = e^{-i\frac{\omega t}{2}\sigma_z}\rho e^{i\frac{\omega t}{2}\sigma_z}, \tag{4.5}$$

and time evolution given by,

$$-i\hbar\frac{d\tilde{\rho}}{dt} = [\tilde{H}'\tilde{\rho}] + \text{relaxation terms} \tag{4.6}$$

Here σ_z is just the usual 2x2 Pauli matrix. From here we can go on to solve for the matrix elements of ρ.

$$\begin{aligned}
\dot{\rho_{11}} &= -i\chi(t)^*\tilde{\rho_{21}} + i\chi(t)\tilde{\rho_{12}} + \gamma_2\rho_{22} \\
\dot{\rho_{22}} &= i\chi(t)^*\tilde{\rho_{21}} - i\chi(t)\tilde{\rho_{12}} - \gamma_2\rho_{22} \\
\dot{\tilde{\rho_{12}}} &= -i\chi(t)^*[\rho_{22} - \rho_{11}] + i\delta\tilde{\rho_{12}} - \gamma\rho_{12} \\
\dot{\tilde{\rho_{21}}} &= i\chi(t)^*[\rho_{22} - \rho_{11}] - i\delta\tilde{\rho_{12}} - \gamma\rho_{12}
\end{aligned} \tag{4.7}$$

The relaxation terms from Eqn. 4.6 are included above where γ_2 denotes the excited state lifetime and γ coherence decay rate of ρ_{12}. These two quantities are related by $\gamma = \gamma_2/2 + \Gamma$, where Γ is the dephasing decay rate and represents the collision rate in atomic vapors. The meaning of these decay rates is worth further discussion.

The meaning of γ_2 is simply the decay of population from the excited state to the ground state. Now γ is slightly more complicated since it represents the decay of the coherence terms ρ_{12} and ρ_{21}. These terms correspond to the in phase and

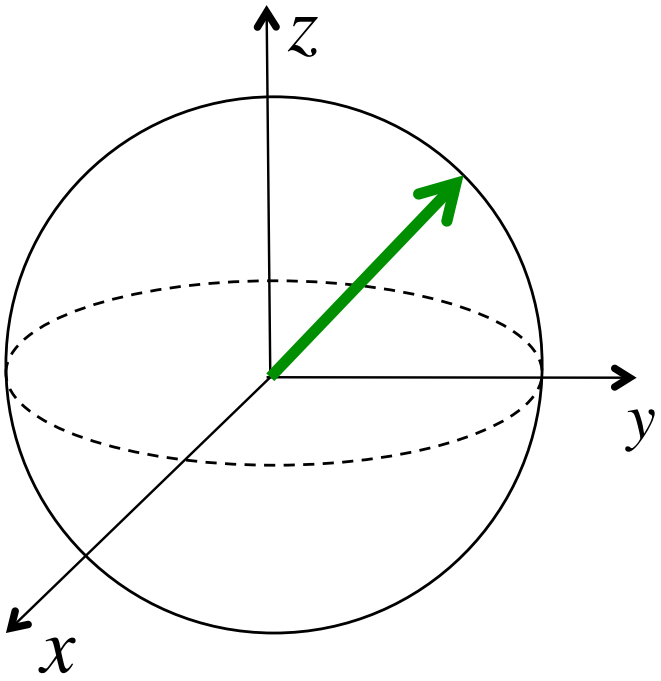

Figure 4.6: An example of a bloch sphere diagram where the green arrow represents the state of the system.

out of phase components of the two level transition dipole moment with the applied field. In the absence of dephasing the relationship of these two quantities reduces to $\gamma = \gamma_2/2$. This expression has a well known analogue in the world of NMR which states that $T2 = 2T1$, where $T1$ is the spin-lattice relaxation rate and $T2$ is the is the spin-spin relaxation rate [49]. The meaning of $T1$ in NMR is the rate by which the spin magnetization relaxes, in the direction of the applied field, into equilibrium with the surroundings; this can be compared to the radiative lifetime in atomic systems, or $1/\gamma_2$. $T2$ represents the transverse decay of the spin magnetization in the direction transverse to the applied magnetic field. A good way to think about this quantity is by shifting the discussion of atomic systems to the Bloch sphere picture. An example of the Bloch sphere for a two-level atom is provided in figure 4.6. The decay in length of the bloch vector in the z direction gives the radiative lifetime and the decay in the transverse plane gives the coherence decay rate, γ. The Bloch sphere visualization

is a useful tool when considering the dynamics of a system. The rotations of the Bloch vector in the transverse and longitudinal direction reveal information about the coherent dynamics of the system.

With a better understanding of the decay terms in our system we can solve for the steady-state solutions of equations 4.7 where in particular we get the expression for the excited state population ρ_{22},

$$\rho_{22} = \frac{2\gamma}{\gamma_2} \frac{|\chi|^2}{\left(\gamma^2 + \delta^2 + \frac{4\gamma}{\gamma_2}|\chi|^2\right)} \tag{4.8}$$

4.5 Voltage Modulated Absorption

To investigate the quantum dot trion transition we use narrow linewidth continuous wave (CW) lasers tuned to the trion resonance. As the lasers scan across the trion resonance a dip in the transmission of the laser through the sample will occur having the Lorentzian profile dictated by Eqn. 4.8. The amount of the beam absorbed when on resonance is usually about 0.1%, which is extremely difficult to observe over the laser intensity fluctuations present in the optical set-up. To observe the signal buried in the noise we employ a lock-in detection scheme.

The lock-in works by taking an input signal, in this case from an avalanche photodiode (APD), and multiplies it by a reference signal and then integrates over a specified time constant (usually 100ms-500ms). The lock-in will pick out a signal occurring at the reference frequency. So, if there is a way to modulate the signal of interest then we only will pick up signal in that specific frequency band and all other sources of noise not in the reference frequency band will be highly suppressed. In typical measurements using lock-in methods two optical fields are used and a single modulation frequency is placed on one of the beams and this serves as the reference for the lock-in. This is often referred to as a pump-probe method, where dynamics in the system induced by the presence of the pump field will be modulated at ω_{pump} so

the signal observed in the probe field will be observed at ω_{pump}. If we are looking at a signal modulated at ω_{pump}, then leakage of the pump beam on to the detector would cause the lock-in to register a unwanted signal. In these experiments great care must be taken to shield the detector from any pump light, this is generally achieved using polarization rejection and/or spatial separation of the beams. The diode nature of our set-up allows us to modulate the signal of interest without requiring a second pump beam.

In our case the diode nature of the sample allows us to modulate the sample instead of another beam. As noted previously in 3.3, the charge state of the QD and detuning can be changed by adjusting the gate voltage across the Schottky diode. So, by modulating the gate voltage using a square wave we can bring the trion on and off resonance with an incident CW laser. By collecting the laser light after it has interacted with the QD we should see a definitive drop in laser intensity as the dot is switched on and off by the modulated voltage. The optical geometry for this scheme is shown in figure 4.5.

Depending on the size of the applied modulation we can get different line shapes. If we use a modulation depth that is less than the linewidth of the of the transition we get a derivative lineshape. Typically we use modulation amplitudes that are of order the linewidth or slightly larger (we refer to this as medium modulation). These techniques are used first to find the energy of the QD transition after a PL bias map is performed. A sample trace of a medium modulation scan is shown in figure 4.5. To get a more accurate scan of the state linewidth using absorption we use large voltage modulation and isolate the transition (seen in figure 4.5.

4.6 Resonant Rayleigh Scattering from a QD

The trion system described above provides us with a degenerate two level system with circularly polarized selection rules as shown in Fig. 3.8a. Experiments involving

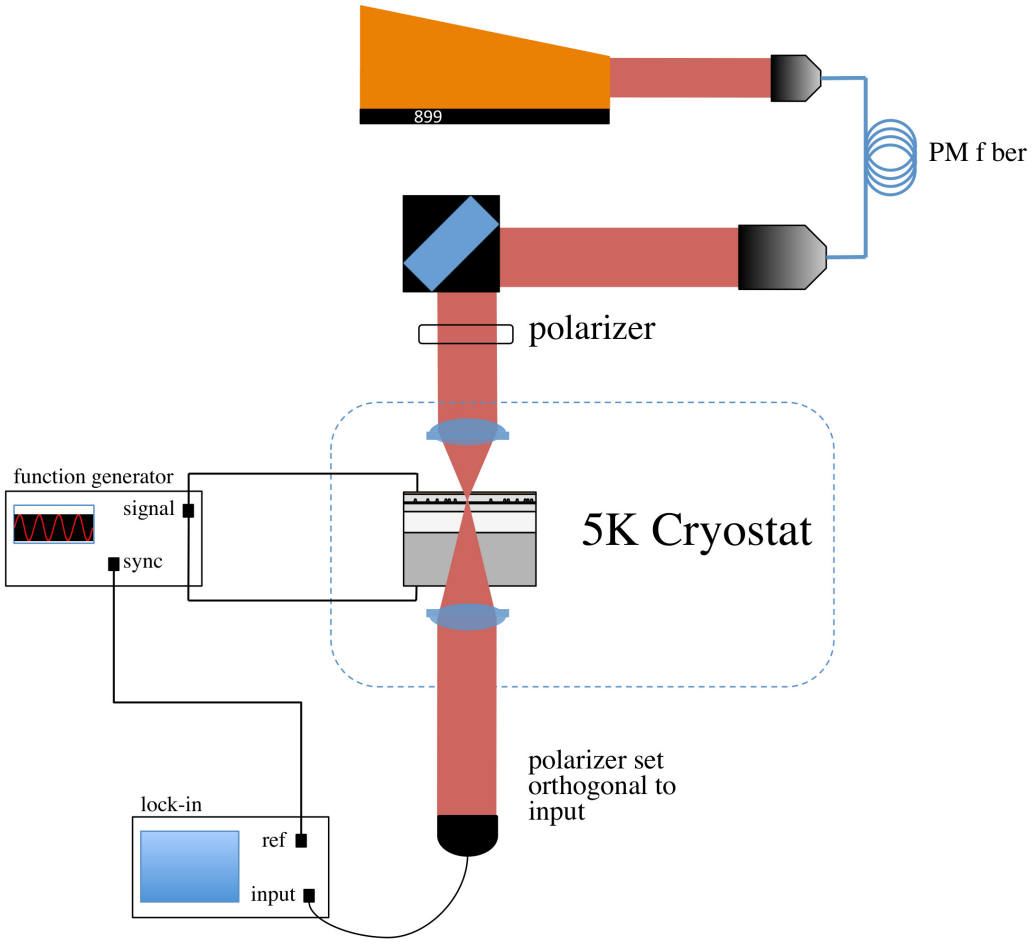

Figure 4.7: The homodyne optical set-up. The sample gate voltage is choped by a signal generator and as the QD is swept on and off resonance the input laser beam experiences absorption when the voltage is on resonance. This signal manifests in the lock-in as a DC signal that follows a Lorentzian line shape as a function of detuning.

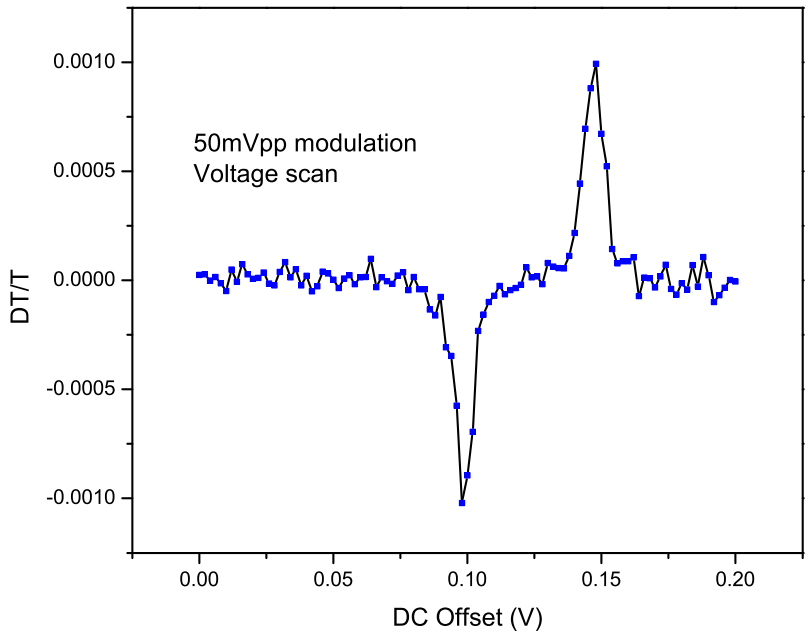

Figure 4.8: An example absorption scan for a medium modulation depth of 50mVpp. We can see that if we imagine decreasing this modulation the two features will combine in a derivative lineshape. Even though this is absorption the phase sensitive detection nature of the lock-in detection scheme gives both a positive and negative peak. An added difference in this scan is that we scan the detuning by scanning the voltage with respect to the a fixed laser frequency. The mirror of this would be to scan the laser frequency while keeping the offset voltage fixed as in figure4.5.

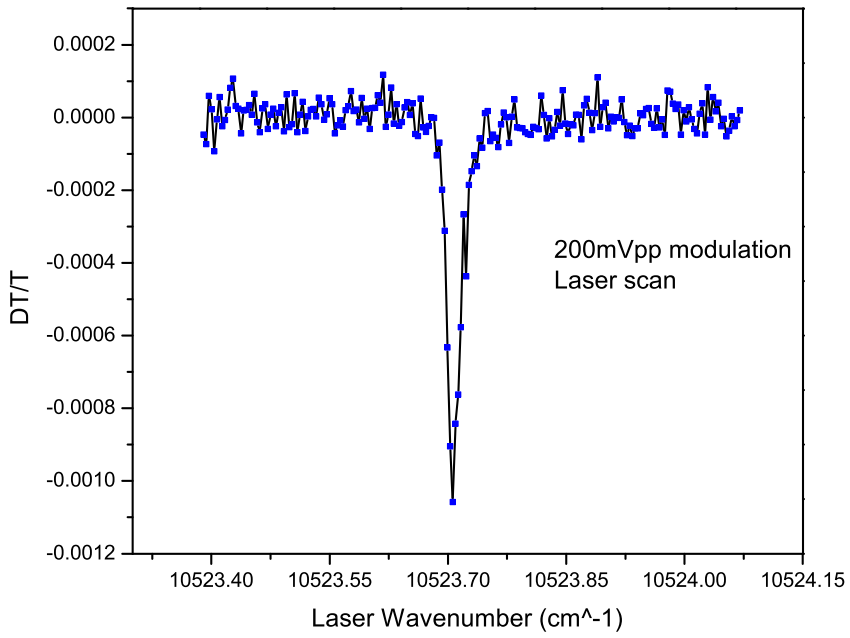

Figure 4.9: An absorption scan similar to figure 4.5 only now the modulation depth is increased to allow only one peak to appear in a given scan range. Here, the laser is scanned while the voltage is kept fixed (aside from the modulation of course) and a Lorentzian lineshape is recovered as the laser passes across the trion resonance.

photon counting with QDs, such as encountered in some entanglement protocols, require the suppression of the excitation laser to allow the detection of photons that are emitted or scattered by the QD exciton (or trion). A schematic of this detection method can be found in figure 4.6. Previous measurements utilize lock-in detection and avalanche photodiodes (APDs) to observe the absorption (a measure of the change in transmission when the laser is on resonance vs off, or DT/T) of laser light by the QD [1]. In those experiments, the APDs measures the transmitted laser intensity instead of the direct single photon scatter from the QD. Here, we use polarization rejection to filter out the excitation laser so that we are only sensitive to single photons scattered from the QD (i.e. the resonant Rayleigh scattering).

For the degenerate two-level system described above linear polarization couples both of the transitions, so we set our input laser to vertical (V). Two aspheric lenses are placed on either side of the QD sample, the front for excitation and the back for collection. The QD will scatter in 4π, but we are only sensitive to the 2% collected by the back asphere. The laser light however is almost completely collected and therefore must be removed to observe the scattered photons. A polarizer set to H in the transmission geometry suppresses the excitation laser by a factor of 10^5. Unfortunately, this level of suppression is insufficient so the use of an optical fiber for spatial filtering gives an extra factor of 100. A single photon avalanche detector (SPAD), which is an APD operated in geiger mode (operated above the breakdown voltage), is sensitive to single photon events that cause the device to register a single event and reset. With the SPAD and a $\sim 10^7$ level of suppression, scanning the laser across a QD resonance reveals a Lorentzian shape signal shown in Fig. 4.11. The state linewidth for this QD is 623$\pm$25 MHz.

A final important step before moving to the time-resolved data involving QDs is to determine if the trion system of interest is indeed a single photon emitter. The most common method to determine if a system is a single emitter is to perform a

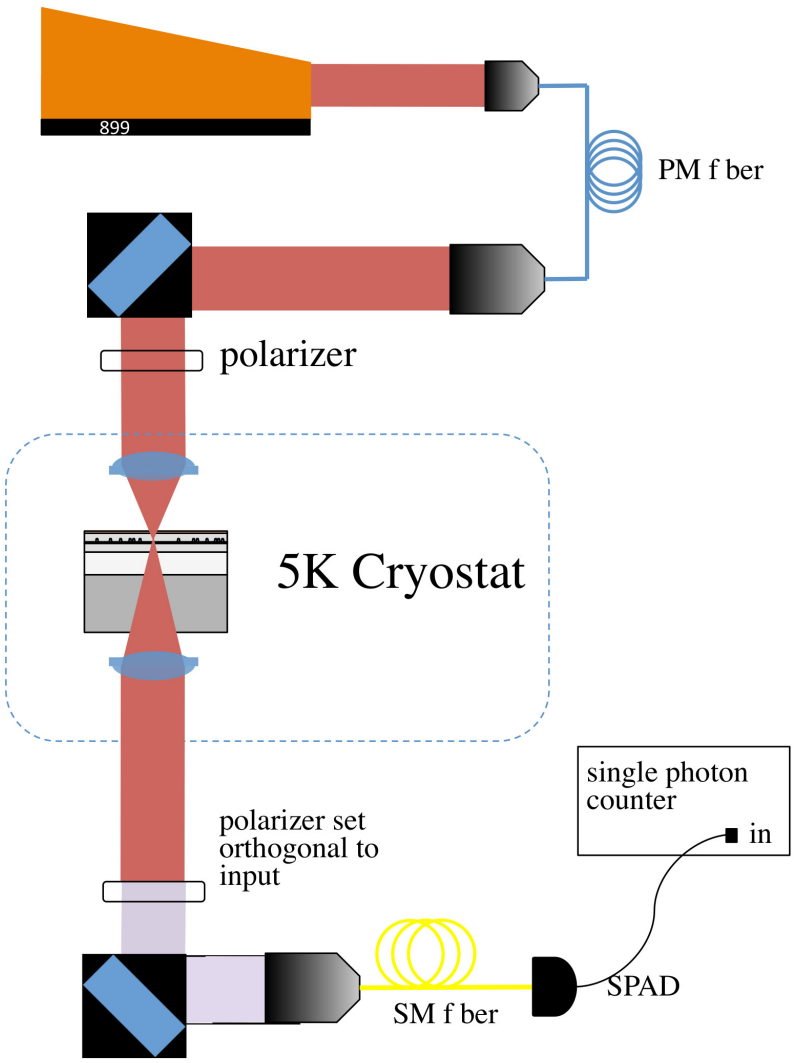

Figure 4.10: The optical set-up for resonant Rayleigh scattering. The excitation laser is focused on the sample and then a combination of polarization and spatial filtering is used to suppress the excitation laser and allow only the scattered single photons to be observed by the single photon avalanche photo-diode (SPAD).

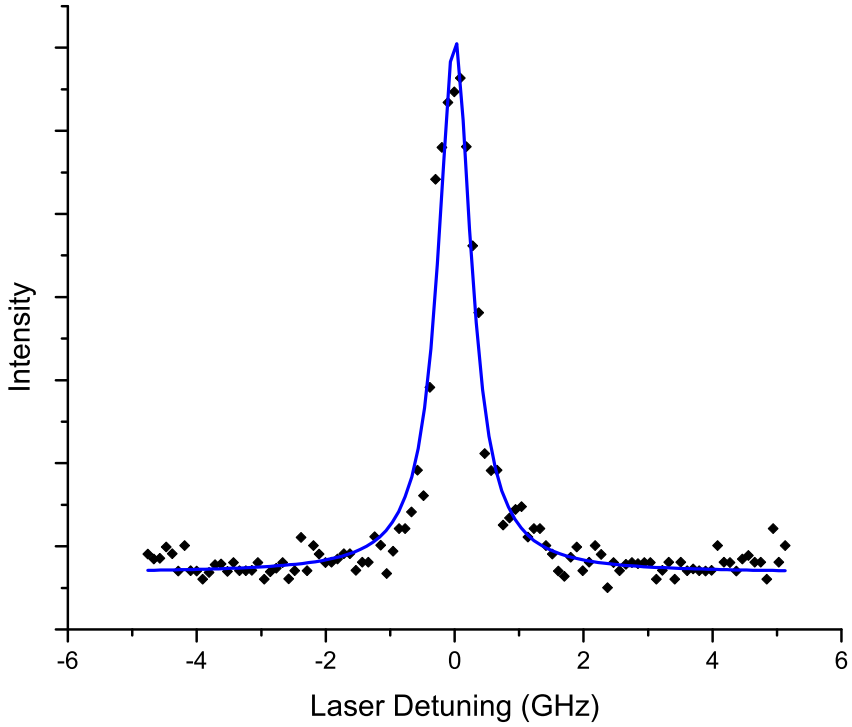

Figure 4.11: An example CW resonance fluorescence scan with a Lorentzian fit yielding a line width of 623 ± 25 MHz.

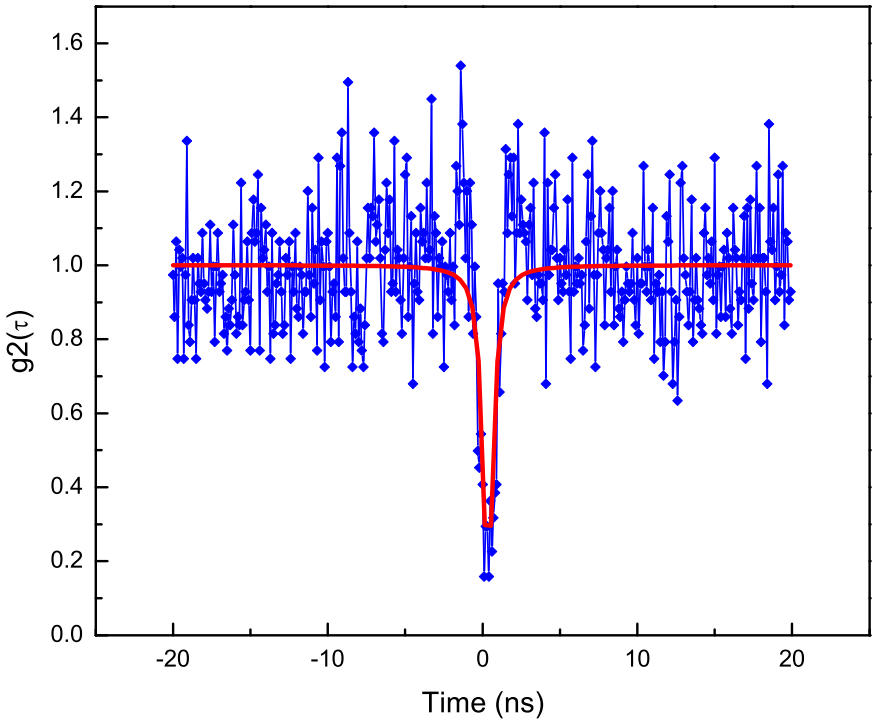

Figure 4.12: The intensity correlation spectrum, $g^{(2)}(\tau)$, for a trion system at zero magnetic field. The dip in the spectrum below 0.5 indicates the non-classical nature of the emitter.

temporal intensity correlation measurement, $g^{(2)}(\tau)$. The arrival times of the photons are recorded in a Hanbury Brown and Twiss (HBT) type set-up where a dip at zero delay indicates a non-classical signature[16, 63]. Data indicating the single emitter nature of the QDs studied here is found in Fig. 4.12.

The excitation laser rejection and the ability to recover the resonant Rayleigh scattered spectrum are essential to photon counting with QDs. The observation of many of the coherent properties of the QD require the ability to do single photon counting as seen in the $g^{(2)}(\tau)$ measurements. In the next section more sophisticated time tagging techniques, required to performed advanced correlation measurements, are introduced.

4.7 Time Domain Fluorescence

Here we present data probing the nature of coherent population oscillations, Rabi oscillations, and discuss excitation techniques that are useful for other coherent control experiments using QDs [73].

In the previous section we reported on observations in the frequency domain using CW lasers for excitation. A further tool we can use in characterizing the coherence properties of QDs is to observe the fluorescence in the time domain. By time gating the excitation of a QD, we can observe the dynamics during and after excitation that are not available in CW measurements. By using an electro-optic modulator (EOM), we time gate a resonant CW laser, synced to a picosecond event timer. The QD light is time tagged using a single photon detector with 40 ps timing jitter and a RF pulse generator sets the master clock and provides the pulse train for the EOM, which intensity modulates the laser. Fig. 4.13 shows a typical diagram for this technique.

A direct measurement of the QD's transient fluorescence follows the dynamics of the excited state for this 2 level system. Using pulse widths less than the radiative lifetime, we observe the characteristic exponential decay of the excited state population (ρ_{22}), shown in Fig. 4.14. From these data, we extract a radiative lifetime of 640 ± 25 ps which is the inverse of the population decay rate. As the incident power increases, the exponential decay will increase until we reach a π pulse meaning all the population has been transferred to the excited state. Increasing the power past the π power drives the system back to the ground state before emission and thus should decrease the counts present in the QD emission spectrum. Fig. 4.15a shows that as the power increases the peak emission along the decay curve (the part of the histogram after 250 ps) decreases. A more pronounced visual of this effect is seen when we integrate over the emission and plot the integrated counts as a function of square root of power, Fig. 4.15b. These are Rabi oscillations and are evident in the

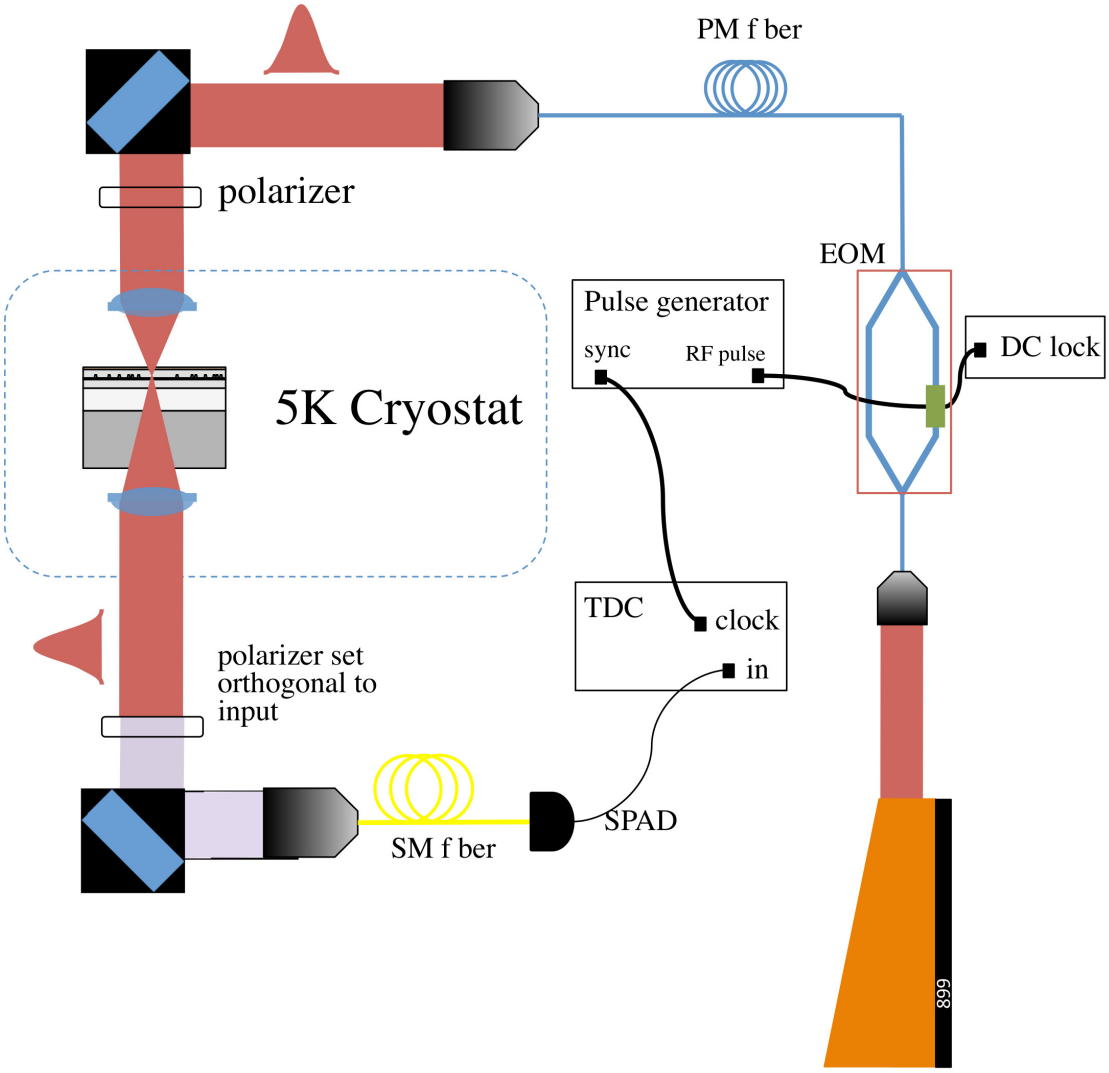

Figure 4.13: Diagram of a typical time tagged fluorescence set-up. The excitation laser is rejected using polarization allowing detection of the QD fluorescence. The EOM is a Lithium Niobate Mach-Zhender where a DC bias applied in one arm creates constructive or destructive interference at the output and the RF input modulates between the constructive and destructive interference. This creates an amplitude modulated, quasi-CW, pulse mirroring the shape of the applied RF signal.

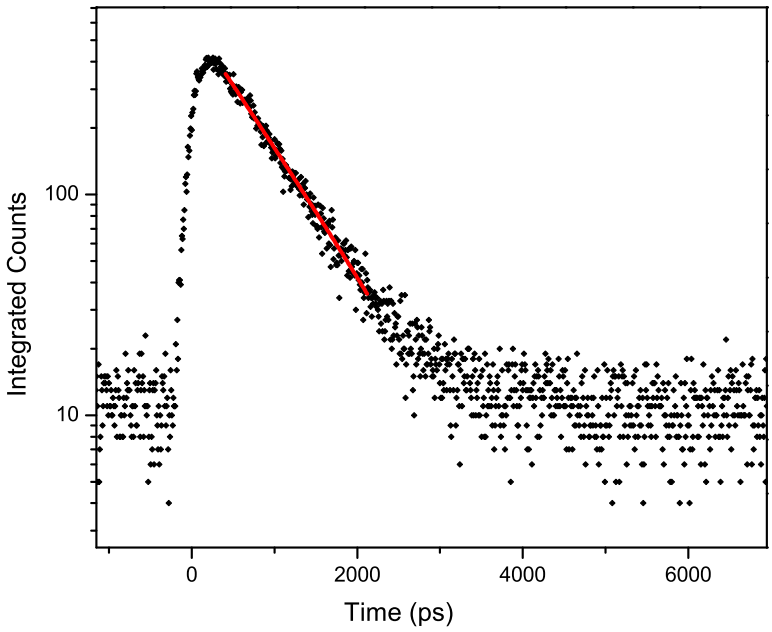

Figure 4.14: An integrated histogram of the time tagged emission from the QD on a log scale with the exponential fit. Excitation is performed with a 250 ps resonant pulse. The single exponential fit gives a lifetime of 640 ± 25 ps

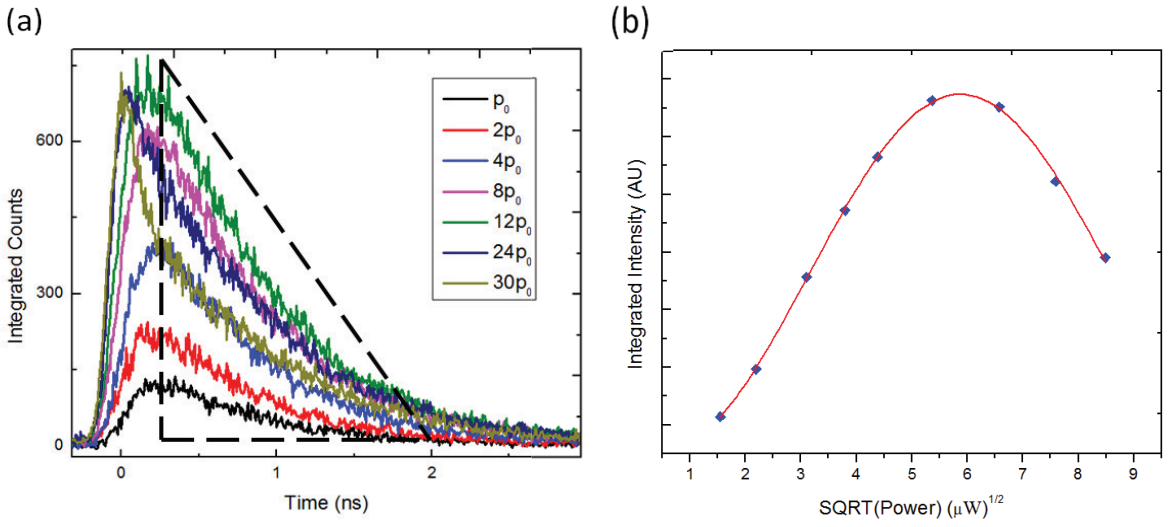

Figure 4.15: (a) Histogram data from a resonant 250 ps pulse with increasing powers showing the increase and decrease in emission as the power surpasses the π power ($12P_0$). (b) Integrated counts taken from the black dotted triangle in (a), are plotted as a function of $\sqrt{(Power)}$ to show the Rabi turnover.

formula for the excited state population under the influence of a driving field E_0,

$$\rho_{22}(t) = sin^2\left(\frac{\mu E_0 t}{2\hbar}\right). \tag{4.9}$$

Where μ is the optical dipole moment. This formula, however, neglects effects from spontaneous emission and decoherence, which are vital to understanding the complete dynamics of the system. Including these effects and solving for the excited state population we find,

$$\rho_{22}(t) = \frac{\Omega_0^2}{2(\Omega_0^2 + \gamma\gamma_2)}\left[1 - \left(cos(\lambda t) + \frac{\gamma + \gamma_2}{2\lambda} sin(\lambda t)\right) e^{-\frac{\gamma+\gamma_2}{2}t}\right] \tag{4.10}$$

with

$$\begin{aligned} \lambda &= \sqrt{\Omega_0^2 - \frac{(\gamma - \gamma_2)^2}{4}} \\ \Omega_0 &= \frac{\mu E_0}{\hbar} \end{aligned} \tag{4.11}$$

Here, we assume resonant excitation, and the generalized Rabi frequency reduces to the usual Ω_0. The exponential in Eqn. 4.10 shows that the oscillation term decays with the average of the longitudinal, γ_2, and transverse, γ, decay rates. An interesting physical interpretation to take from this is that as the optical Bloch vector rotates about the one axis, x, it spends an equal amount of time in both y and z. The magnitude along each axis will decay according to the separate decay rates where y decays at γ, and z at γ_2

Eqn. 4.10 follows the excited state population for a constant field, rendering the analysis on the 250 ps pulse data incomplete when considering the time evolution of ρ_{22} under constant driving field. To further probe the behavior of the excited state, we should look at excitations with a duration larger than the radiative lifetime. Increasing the pulse width and continuing to monitor the fluorescence in the same

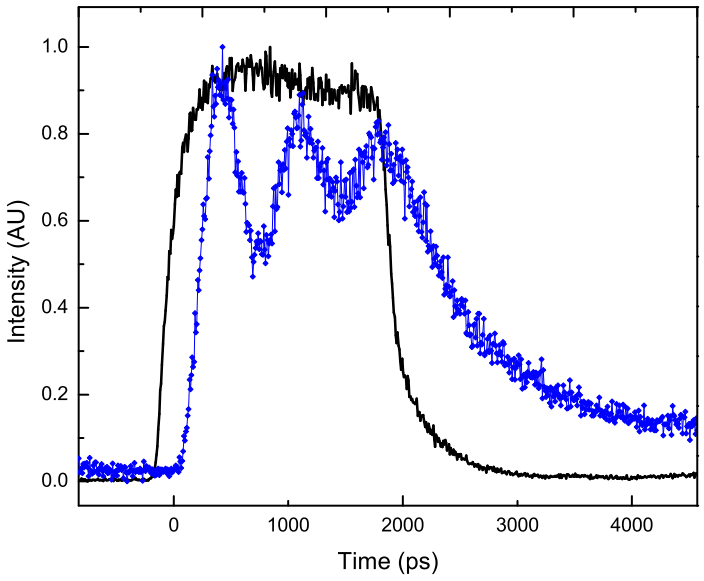

Figure 4.16: A scaled histogram of the 2 ns excitation pulse (black) and the resultant QD fluorescence (blue) when the excitation pulse is suppressed using polarization rejection.

way allows for the direct probe of Eqn. 4.10.

As the pulse width and power are increased, we begin to see oscillations in the time tagged emission. A scaled example of the pulse and the quantum dot scattering are shown in Fig. 4.16. The oscillation frequency increases linearly with the square root of power as expected. Due to the previous determination of the population decay lifetime, $1/\gamma_2$, only the Rabi frequency and decoherence lifetime, γ, are left as unknowns. Using data for multiple input powers we can fit Eqn. 4.10 during the excitation pulse leaving Ω_0 and γ as fitting parameters. From the fits we extract a decoherence lifetime, $1/\gamma$, of 1.22 $\pm$ 0.06 ns. In the absence of pure dephasing we would expect that $2\gamma = \gamma_2$, which is what we observe and is consistent with other studies done on InAs QDs[87]. Also, of interest is the comparison of this time domain data to the CW data shown in Fig. 4.11 of the previous section. The line width extracted from the CW laser scan is 623 $\pm$ 25 MHz, which would imply a decoherence

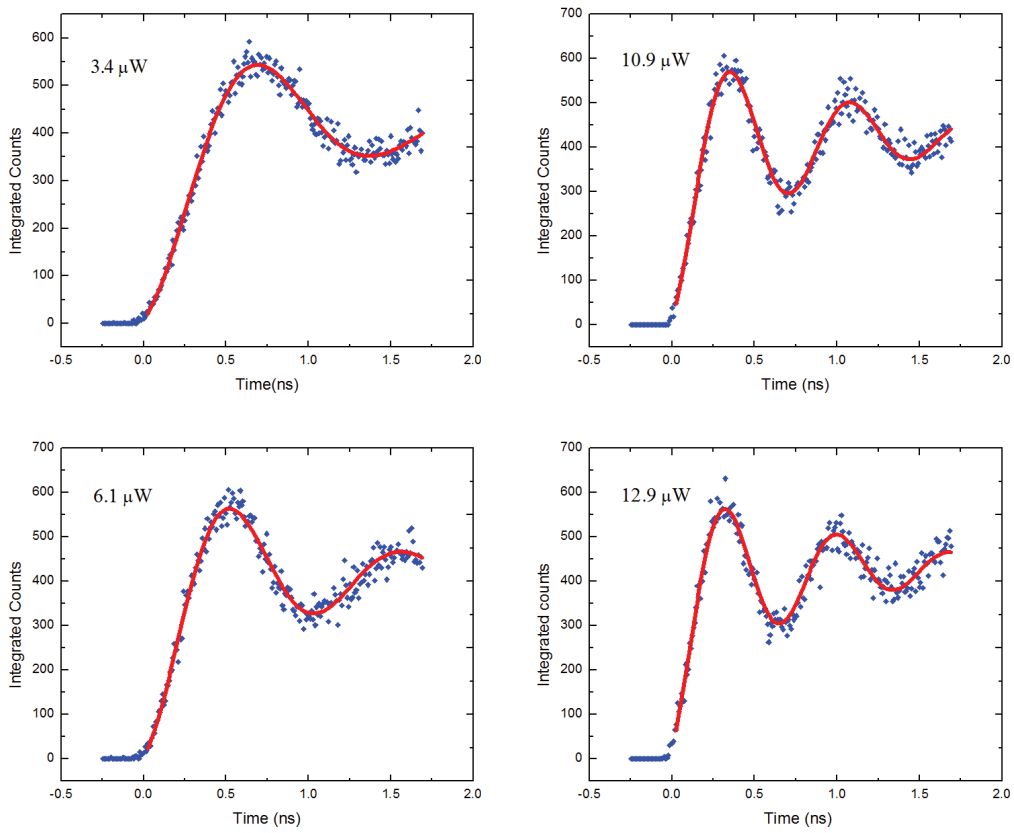

Figure 4.17: Histograms of time resolved QD fluorescence resulting from a 2 ns excitation pulse. The time-dependent Rabi oscillations are seen to increase in frequency as the excitation power increases. The input powers are given on each graph.

lifetime of 511 ± 21 ps. Since the time domain measurements indicate a much longer coherence time we must conclude that the frequency domain measurements of the line width are broadened by some spectral wandering process, which has been previously proposed[86, 42].

Previous studies of Rabi oscillations in QDs utilize short pulses, 2 ps, to drive the oscillations and are observed as a function of the electric field by way of a CW readout laser[80]. Additional experiments show the onset of Rabi oscillation as they manifest in the intensity correlation function, $g2(t)$, of the QD emission[63]. However, our experiment is unique in that we are able to follow the time evolution of the system

as predicted by the solution to the initial value problem of an exciting field, Eqn. 4.10. By using both long (2 ns) and short (250 ps) pulse studies we have determined that the frequency domain response of the QD appears to be broadened beyond the natural linewidth by a spectral wandering process and that the optical decoherence rate is limited by the spontaneous emission rate. Verification of this has profound implications for QDs as nodes in a quantum memory since many architectures utilize photons as carriers of quantum information between nodes[23, 28, 91]. A short optical coherence time would significantly diminish the effectiveness of such systems.

4.8 Optically Induced Spin Rotations

Before we can move on to more complicated entanglement and teleportation studies with QD spins and photons we must first develop a technique to coherently control the QD spin state using fast pulses. The speed of these pulses (2ps) is consistent with the DiVincenzo criteria for a scalable quantum network using QDs[51], which is fast gate operations. In the most simplest form, gate operations are merely spin flips, which is what we will be discussing in this section.

As stated previously, section 3.4.2, the trion system in the Voigt geometry gives rise to a four level system with linearly polarized selection rules. The ground state spin ($|x+\rangle$ and $|x-\rangle$) is the qubit of interest and rotations or spin flips will refer to manipulations of this spin state. By using a pulse detuned from the trion states we can drive a two-photon or stimulated Raman transition [19, 30]. The system can now be thought of as an effective two level system consisting of the ground state spins, where π pulses and $\pi/2$ pulses will transfer population or place the system in a superposition of spin states, respectively. A schematic of the level diagram and the pulse detuning is given in figure 4.8.

Now we look at the current system when acted upon using this Raman pulse to determine the best way to model spin rotations which will become important in the

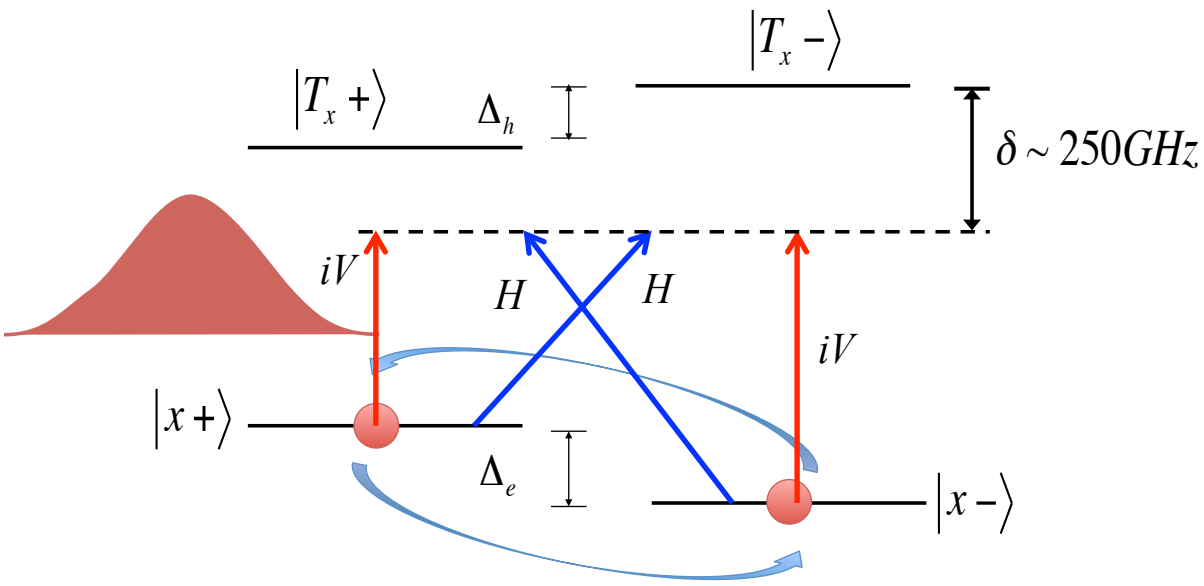

Figure 4.18: The four level diagram for a trion in the Voigt geometry under excitation of a detuned (250GHz) Raman pulse that drives spin flips between $|x+\rangle$ and $|x-\rangle$ dependent on the pulse area.

next chapter. So we can write the full Hamiltonian in the field interaction picture under the influence of a detuned pulse as,

$$\tilde{H(t)} = \begin{pmatrix} -\frac{\hbar\Delta_e}{2} & 0 & V_{13} & V_{14} \\ 0 & \frac{\hbar\Delta_e}{2} & V_{23} & V_{24} \\ V_{31} & V_{32} & \hbar\omega_0 - \frac{\hbar\Delta_h}{2} & 0 \\ V_{41} & V_{42} & 0 & \hbar\omega_0 + \frac{\hbar\Delta_h}{2} \end{pmatrix} \tag{4.12}$$

Where the electric field of the pulse is modeled as,

$$E_p(t) = 1/2 E_p \text{sech}\left(\frac{t}{\tau}\right)\left(\hat{\epsilon}e^{-i\omega_p t} + \hat{\epsilon}^* e^{i\omega_p t}\right), \tag{4.13}$$

with τ as the pulse width. Using a general definition of $\hat{\epsilon}$,

$$\hat{\epsilon} = \frac{\hat{x} + e^{i\phi}\hat{y}}{\sqrt{2}}, \tag{4.14}$$

we can write the expressions for the V_{ij} terms above,

$$\begin{aligned} V_{13} &= V_{24} = V_{31} = V_{42} = \frac{\hbar\chi_p}{\sqrt{2}}\text{sech}\left(\frac{t}{\tau}\right)\left(e^{-i\omega_p t} + e^{i\omega_p t}\right) \\ V_{14} &= V_{23} = -V_{32} = -V_{23} = \frac{i\hbar\chi_p}{\sqrt{2}}\text{sech}\left(\frac{t}{\tau}\right)\left(e^{i\phi}e^{-i\omega_p t} + e^{-i\phi}e^{i\omega_p t}\right) \end{aligned}$$

We can solve for the equations of motion for the four state amplitudes using,

$$\dot{c}_i(t) = \frac{1}{i\hbar}\sum H_{ij}c_j(t) \tag{4.15}$$

and recall that in the field interaction picture the amplitudes become,

$$\begin{aligned} c_1(t) &= \tilde{c_1}(t), c_2(t) = \tilde{c_2}(t) \\ c_3(t) &= \tilde{c_3}(t)e^{-i\omega_p t}, c_4(t) = \tilde{c_4}(t)e^{-i\omega_p t}. \end{aligned}$$

Solving for the equations of motion,

$$\begin{aligned} \dot{\tilde{c}}_1(t) &= \frac{i\Delta_e}{2}\tilde{c_1}(t) - \frac{i\chi_p}{\sqrt{2}}\text{sech}\left(\frac{t}{\tau}\right)\left(\dot{\tilde{c}}_3(t) + i\dot{\tilde{c}}_4(t)e^{i\phi}\right) \\ \dot{\tilde{c}}_2(t) &= -\frac{i\Delta_e}{2}\tilde{c_2}(t) - \frac{i\chi_p}{\sqrt{2}}\text{sech}\left(\frac{t}{\tau}\right)\left(i\dot{\tilde{c}}_3(t)e^{i\phi} + \dot{\tilde{c}}_4(t)\right) \\ \dot{\tilde{c}}_3(t) &= -i\left(\omega_0 - \omega_p - \frac{\Delta_h}{2}\right)\tilde{c_3}(t) - \frac{i\chi_p}{\sqrt{2}}\text{sech}\left(\frac{t}{\tau}\right)\left(\dot{\tilde{c}}_1(t) - i\dot{\tilde{c}}_2 e^{i\phi}(t)\right) \\ \dot{\tilde{c}}_4(t) &= -i\left(\omega_0 - \omega_p + \frac{\Delta_h}{2}\right)\tilde{c_4}(t) - \frac{i\chi_p}{\sqrt{2}}\text{sech}\left(\frac{t}{\tau}\right)\left(\dot{\tilde{c}}_2(t) - i\dot{\tilde{c}}_1 e^{i\phi}(t)\right) \end{aligned}$$

For a sufficiently large detuning ($\delta = \omega_0 - \omega_p > \Delta_h$) the excited state amplitudes become adiabatically eliminated and we are left with,

$$\begin{aligned} \dot{\tilde{c}}_1(t) &\approx \frac{i\chi_p^2}{2\delta}\text{sech}^2\left(\frac{t}{\tau}\right)\tilde{c_2}(t)\left(e^{i\phi} - e^{-i\phi}\right) \\ \dot{\tilde{c}}_2(t) &\approx \frac{i\chi_p^2}{2\delta}\text{sech}^2\left(\frac{t}{\tau}\right)\tilde{c_1}(t)\left(e^{i\phi} - e^{-i\phi}\right) \end{aligned} \tag{4.16}$$

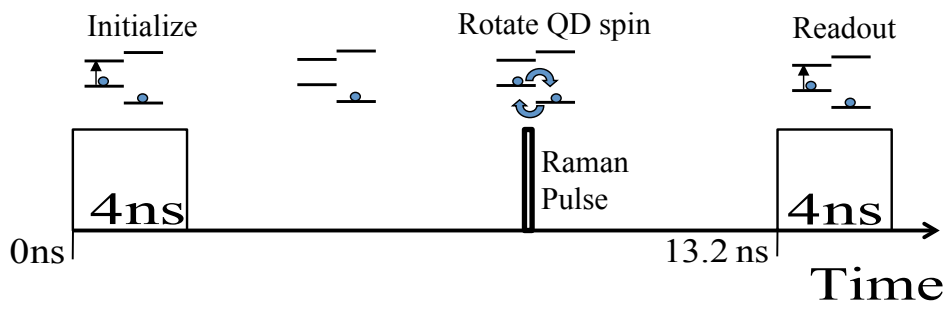

Figure 4.19: Timing diagram for the spin rotations experiment. The first 4ns pulse initializes the system to $|x+\rangle$ and the Raman pulse rotates the spin state where the 4ns pulse from the next shot reads out the population in the $|x+\rangle$ state. As the power on the Raman pulse is changed, the amount of population in $|x+\rangle$ will change and the scattering in the readout pulse will reflect that.

. Here ϕ is set to represent the polarization state of the input pulse. For example, in the case of $\sigma+$, $\phi = \pi/2$ and we are left with,

$$\begin{aligned} \dot{\tilde{c}_1}(t) &\approx -\frac{i\chi_p^2}{\delta}\text{sech}^2\left(\frac{t}{\tau}\right)\tilde{c_2}(t) \\ \dot{\tilde{c}_2}(t) &\approx \frac{i\chi_p^2}{\delta}\text{sech}^2\left(\frac{t}{\tau}\right)\tilde{c_1}(t) \end{aligned}$$

By solving these equations we can write a unitary transformation matrix for the rotations of the spin state,

$$R(\theta) = \begin{pmatrix} \cos\left(\frac{\theta}{2}\right) & -i\sin\left(\frac{\theta}{2}\right) \\ -i\sin\left(\frac{\theta}{2}\right) & \cos\left(\frac{\theta}{2}\right) \end{pmatrix} \tag{4.17}$$

where the angle θ is given by,

$$\theta = \frac{\chi_p^2\tau}{\delta}.$$

So we can see that by adjusting the Rabi frequency (χ_p) the pulse area is adjusted and the rotation we are able to induce between $|x+\rangle$ and $|x-\rangle$ is changed.

To verify that this detuned Raman pulse drives spin flips in our system we use

scattering off the trion transitions to readout the spin state. The experiment will use a 4ns EOM pulse similar to the one discussed above as both the initialization and readout of the spin state. This initialization pulse is tuned to the $|x+\rangle \rightarrow |T_x+\rangle$ transition, which optically pumps all the population into the $|x-\rangle$ state (a sample timing diagram for this spin rotation experiment can be found in figure 4.8). Next a Raman pulse of variable power (which maps into pulse area) is used to rotate the spin state and depending on the area can give a full rotation of the spin back into $|x+\rangle$ or a partial rotation. The optical pumping pulse from the next shot of the experiment will scatter a photon only if the spin state is in $|x+\rangle$. So by looking for scattering events in the readout pulse and comparing that with the Raman pulse power we should see a clear sinusoidal dependence of the $|x+\rangle$ spin state population as a function of $\sqrt{\text{power}}$[45, 66]. This dependence can be seen clearly in figure 4.8. We build statistics by integrating each power point.

In order to effectively drive rotations of the QD spin state optically we must use a detuned Raman pulse. This technique has the added advantage that we adiabatically eliminate the excited trion states so there is no stray scattering during the spin flip process that could contribute to background. The rotation pulse will become important when discussing entanglement and teleportation since these schemes require the ability to rotate a coherent superposition of spin states in to a population of a single spin state. This feat is accomplished by using a $\pi/2$ pulse area pulse which we will discuss more in the next chapter.

4.9 Conclusion

In this Chapter we have laid out the recent techniques developed to manipulate QDs in a more versatile way. The direct detection of the light scattered from a QD is a recent technological feat, and the use of EOMs to gate CW laser has already yielded results interesting to the field. The Rabi oscillations observed during a long

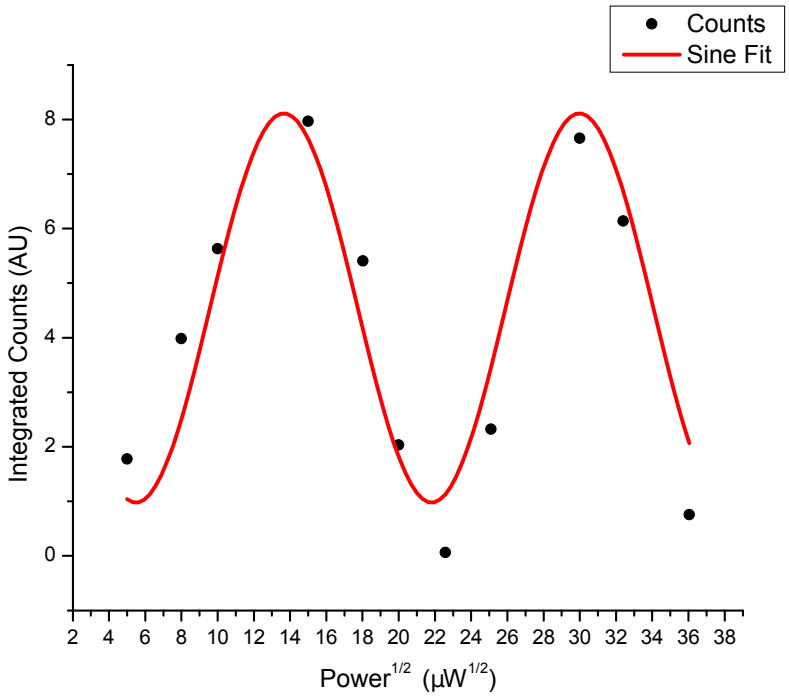

Figure 4.20: Data showing that as the power in the Raman pulse is increased the population in $|x+\rangle$ traces out a sine wave as a function of $\sqrt{\text{power}}$ as we would expect from equation 4.17. The sine fit is included as a guide to the eye.

excitation pulse give us insight to the optical decoherence nature of the QD and allow us to extract a decoherence time consistent with no pure de-phasing. The ability to follow the excited state population evolution is itself unique and has never been achieved in QDs before. One might take for granted that QDs give data similar to a well behaved two level system, but it is not obvious that such a system would be capable of suppressing the many-body physics to reveal a more elegant behavior.

CHAPTER V

Entanglement Verification Between a QD spin and a photon

5.1 Introduction

This chapter follows data and analysis on entanglement between a photon emitted from a QD and its electron spin qubit previously published by our group[72], and others[37, 25]. As was previously discussed, a single electron confined to a QD provides an exceptional candidate for quantum computing. To make this system viable there must be some way to coherently transport information from one quantum node to another. A straightforward way to accomplish this is by using the spontaneously emitted photon from the QD to transmit the spin qubit information between nodes. Such a technique requires entanglement between the emitted photon and the spin qubit[28, 23, 91]. Experimental verification of this entanglement is vital to the feasibility of QDs for quantum computing.

5.2 Theoretical background: Jaynes-Cummings Model

In this section, a theoretical description of the proposed entanglement is presented. A photon emitted from $|T_x-\rangle$ has two paths: a H polarized photon emitted and an electron in $|x-\rangle$, or a V photon and an electron in $|x+\rangle$. Superficially, the resulting

spin state and the polarization state of the photon appear to be entangled, however a rigorous approach would be more satisfying. The following treatment will use the conventions from Berman and Malinovsky, and follow closely their treatment of the Jaynes-Cummings Hamiltonian [7]. We start with the Jaynes-Cummings Hamiltonian in the dipole and rotating-wave approximation for a 3 level system (which is a good approximation since the $|T_x+\rangle$ is not involved in the spontaneous emission process) with photons in H and V.

$$\begin{aligned} H &= \hbar\omega_{T_{x}-}\sigma_z^{T_{x}-} + \hbar\omega_{x-}\sigma_z^{x-} + \hbar\omega_{x+}\sigma_z^{x+} \\ &+ \sum_j \hbar\omega_{Hj}a_{Hj}^\dagger a_{Hj} + \sum_{j'} \hbar\omega_{Vj'}a_{Vj'}^\dagger a_{Vj'} \\ &+ \hbar\left[\sum_j g_{Hj}\left(\sigma_+^H a_{Hj} + a_{Hj}^\dagger\sigma_-^H\right) + \sum_{j'} g_{Vj'}\left(\sigma_+^V a_{Vj'} + a_{Vj'}^\dagger\sigma_-^V\right)\right] \end{aligned} \tag{5.1}$$

The state we investigate is,

$$\begin{aligned} |\psi(t)\rangle &= \sum_j b_{Hj}(t)e^{-i(\omega_{Hj}+\omega_{x+})t}|x+;1_{Hj}\rangle \\ &+ \sum_{j'} b_{Vj'}(t)e^{-i(\omega_{Vj'}+\omega_{x-})t}|x-;1_{Vj'}\rangle + c_D(t)e^{-i\omega_{T_{x-}}t}|T_{x-};0\rangle \end{aligned} \tag{5.2}$$

Where $|E;0\rangle$ denotes the dot is in the excited state and there is no photon, while $|x+;1_H\rangle$ denotes the QD ground state corresponding to a H emitted photon, and the sum is over all of the emitted photon modes. Applying the Schrodinger equation

gives,

$$
\begin{aligned}
& i\sum_j \dot{b}_{Hj}(t)e^{-i(\omega_{Hj}+\omega_{x+})t}|x+;1_{jH}\rangle \\
+ \;& i\sum_{j'} \dot{b}_{Vj'}(t)e^{-i(\omega_{Vj'}+\omega_{x-})t}|x-;1_{Vj'}\rangle \\
+ \;& i\dot{c}_D(t)e^{-i\omega_{T_{x-}}t}|T_{x-};0\rangle \\
= \;& -|x+;1_H\rangle\left(\sum_j g_{Hj}c_D(t)e^{-i\omega_{T_{x-}}t}\right) \\
- \;& |x-;1_V\rangle\left(\sum_{j'} g_{Vj'}c_D(t)e^{-i\omega_{T_{x-}}t}\right) \\
+ \;& |E;0\rangle\left(\sum_j g_{Hj}b_{Hj}(t)e^{-i(\omega_{Hj}+\omega_{x+})t}+\sum_{j'} g_{Vj'}b_{Vj'}(t)e^{-i(\omega_{Vj'}+\omega_{x-})t}\right)
\end{aligned}
\tag{5.3}
$$

Writing the equations of motion for the state amplitudes gives us,

$$
\begin{aligned}
\dot{b}_H(t) &= i\left(\sum_j g_{Hj}c_D(t)e^{i\delta_{Hj}t}\right) \\
\dot{b}_V(t) &= i\left(\sum_{j'} g_{Vj'}c_D(t)e^{i\delta_{Vj'}t}\right) \\
\dot{c}_D(t) &= -i\left(\sum_j g_{Hj}b_{Hj}(t)e^{-i\delta_{Hj}t}+\sum_{j'} g_{Vj'}b_{Vj'}(t)e^{-i\delta_{Vj'}t}\right)
\end{aligned}
\tag{5.4}
$$

with

$$\delta_{Hk,Vk'} = \omega_{Hk,Vk'} + \omega_{x+,x-} - \omega_{T_{x-}}. \tag{5.5}$$

If we put in a decay from the excited state by hand we can solve these equations by direct integration.

$$c_D(t) = e^{-\Gamma t} \tag{5.6}$$

Now the expression for the k and k' mode of $b_H(t)$ and $b_V(t)$ becomes,

$$b_{Hk}(t) = \frac{g_{Hk}}{\delta_{Hk} - i\Gamma} e^{\left(i\delta_{Hk} - \Gamma\right)t} \tag{5.7}$$

$$b_{Vk'}(t) = \frac{g_{Vk'}}{\delta_{Vk'} - i\Gamma} e^{\left(i\delta_{Vk'} - \Gamma\right)t} \tag{5.8}$$

These coefficients form the Lorentzian line shape we expect from the spontaneous emission. Additionally, equation 5.4 indicates that the state amplitude c_D is now entangled with the H and V photon. This calculation could be taken further to encompass another excited state with more complicated dynamics. However, for the purposes of this paper, showing the entangled nature of the system is sufficient to proceed. The overlap we have shown is Loretzian, and a much more rigorous calculation, modeling the detection process, has shown the full recovery of entanglement, if a fast detector is used[71].

5.3 Entanglement Background and Set-up

The protocol we use to verify the entanglement demonstrates correlation between the spontaneously emitted photon's polarization state and the final spin state. The correlation measurements are performed in two orthogonal bases x and z for the spin state, which correspond to linear and circular polarization for the photon. This technique has been utilized in previous demonstrations of entanglement between a matter qubit and an emitted photon[12, 83, 84, 81]. We will be working with the energy level structure shown in Fig. 3.8b and will be focusing on a photon emitted from the $|T_x-\rangle$ state resulting in the entangled state described in Eqn. 5.9. As described above the entanglement of interest is between the spin state ($|x+\rangle$ and $|x-\rangle$) and the polarization state of the photon ($|H\rangle$ and $|V\rangle$). The frequency is also entangled with the spin and will destroy the entangled state if the frequencies are resolvable by elements in the set-up. To eliminate this problem we employ a fast

detection scheme where the timing resolution of the single photon detector used to observe the entangled photon is (48 ps) faster than the bandwidth of the ground state splitting (set at $\Delta_e/2\pi = 7.35$ GHz) to destroy the "which-path" information[71]. The resulting entangled state of the system becomes,

$$|\Psi\rangle = \frac{|H\rangle|x+\rangle - i|V\rangle|x-\rangle}{\sqrt{2}} \tag{5.9}$$

The time resolved fluorescence techniques developed in section 4.7 are essential when initializing the system, generating the entanglement, and finally reading out the spin state. To begin we must initialize to a pure state, $|x-\rangle$, using an EOM to gate a narrow bandwidth CW laser similar to the 2 ns pulse employed earlier to generate Rabi oscillations. This pulse is tuned to the $|x+\rangle \leftrightarrow |T_x+\rangle$ transition for 4 ns and results in optical pumping to the $|x-\rangle$ state. Following this initialization a pulse (250 ps), shorter than the radiative lifetime, excites to the $|T_x-\rangle$ state. In order to transfer the entire population to the excited state we employ the technique shown in Fig. 4.15 of section 4.7 to determine the π power. Once the pulse is turned off, the excited state will decay to one of two paths creating the entangled state of Eqn. 5.9[29]. The experiment is performed at a repetition rate of 76 MHz, so the optical pumping pulse from the next shot of the experiment will act as a readout of the $|x+\rangle$ state since it is already tuned to that transition.

A diagram of the optical set-up can be seen in figure 5.3 where we show the set-up for the full rotated basis experiment. When investigating the linear basis in the next section we simply exclude the rotation pulse and the sync for the experiment is set by the internal repetition rate of the pulse generator.

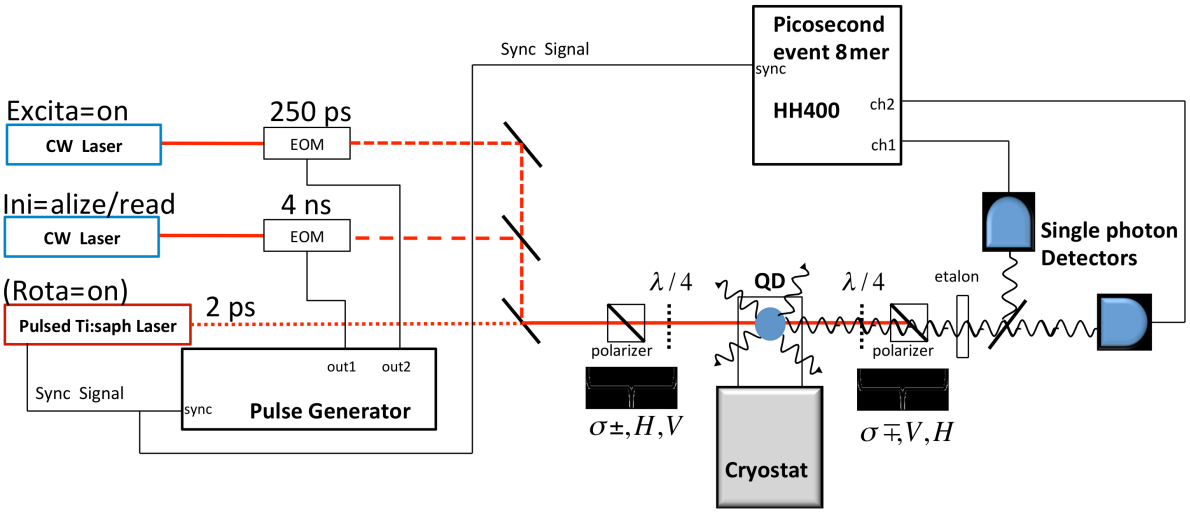

Figure 5.1: The optical set-up for the spin photon entanglement verification. The CW lasers are gated using EOMs synced with the MIRA rep-rate. A 4ns pulse is used as the initialization pulse and the readout pulse and the 250ps pulse is used to create population in $|T_x-\rangle$, where a decay will create the spin-photon entangled state of interest. For the linear basis correlations in section 5.4 the rotation (MIRA) pulse is removed and the master clock is set by the internal pulse generator rep-rate. Two detectors are used in these experiments since we want to measure two events within a single frame and the detectors have significant dead-time making them useless for 100ns after a "photon" event is registered.

5.4 Linear Basis Correlations

The linear basis measurement correlation is rather straightforward. We need to determine the conditional probabilities of a H or V photon emitted and being in $|x-\rangle$ or $|x+\rangle$. The use of polarization rejection makes this measurement easy to perform. However, in the z (rotated) basis, polarization selection happens using $\sigma+$ or $\sigma-$ polarized light, since we are correlating these polarizations with $|z+\rangle$ and $|z-\rangle$, which are linear combinations of the nondegenerate x basis states and hence evolve in time. Our detection scheme requires a collection polarization orthogonal to the input polarization (see section 4.6). This demands that the short pulse excitation laser be narrow enough in frequency to only excite to $|T_x-\rangle$, since the input polarization would not prohibit it from coupling to $|T_x+\rangle$. The EOM generated pulse provides us with the narrow band excitation required.

In the x basis, the conditional probabilities we want to find are, $P(x+|H), P(x-|H), P(x+|V)$, and $P(x-|V)$. For example, $P(x+|H)$ reports the probability that the system is in state $|x+\rangle$ if a H photon is emitted after excitation to $|T_x-\rangle$ what is the probability of population in $|x+\rangle$, this should be unity for perfect correlation. For the positive correlations, $P(x+|H)$ and $P(x-|V)$, the timing diagram is shown in Fig. 5.2. The following description is how we determine $P(x+|H)$, and the extension to $P(x-|V)$ is obvious. Using V polarized input light, so we can collect the H polarized emission, once the state is initialized to $|x-\rangle$ we excite with a π pulse to $|T_x-\rangle$ and measure the time of decay. If a photon is detected along the decay then the QD should be in $|x+\rangle$ and the readout (initialization pulse from the next shot of the experiment) will scatter a photon. By correlating this with readout pulses in distant shots of the experiment, which should have no correlation, we are able to observe a strong positive correlation (Fig. 5.3).

For negative correlations, $P(x-|H)$ and $P(x+|V)$, we insert an extra 250 ps pulse (see Fig. 5.4). Again, we will describe the case for the detection of H polarized light,

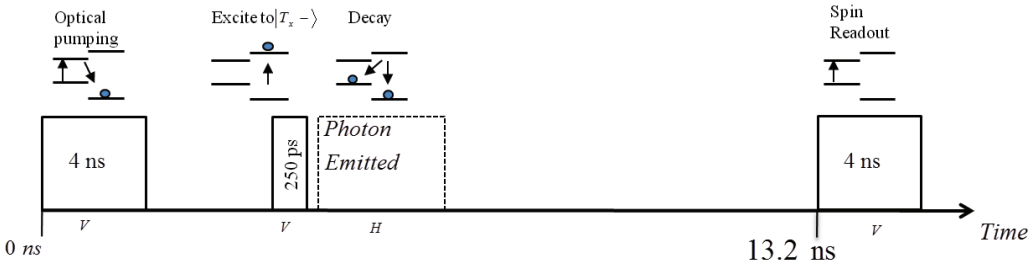

Figure 5.2: Pulse sequence for determining positive correlations for $P(x+|H)$. A photon emitted in the dashed region will only be detected if it is a H photon and therefore scattering should occur with a probability of 1 during the spin readout. To normalize this measurement, correlations between detection of a photon in the dashed region and scattering from a spin readout of a distant shot are set to 1/2 since the entire system has been reset from shot to shot.

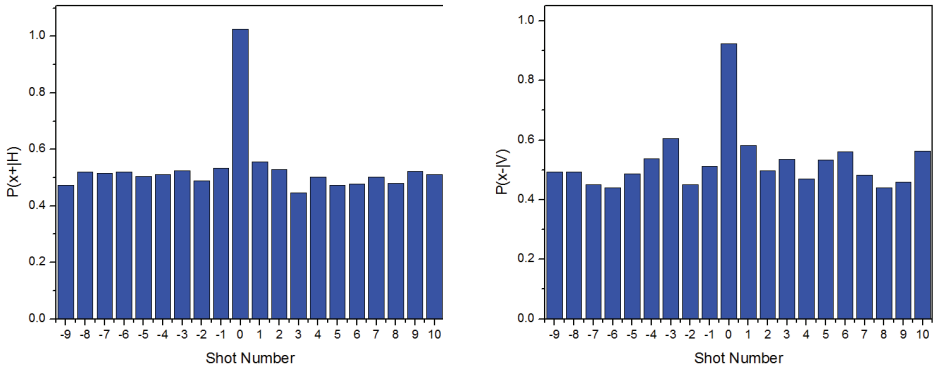

Figure 5.3: Conditional probability data for $P(x+|H)$ and $P(x-|V)$ where the distant shot number is label and the average correlations between a photon in the emission region of shot 0 and a readout photon from all distant shots, have been set to 1/2.

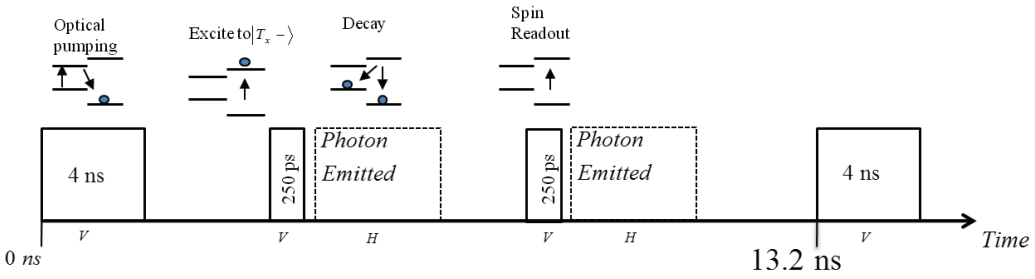

Figure 5.4: Pulse sequence for anti-correlation measurements of $P(x-|H)$ and $P(x+|V)$. The addition of an extra 250 ps pulse serves as a readout of the $|x-\rangle$ state. If a photon is found in the emission region of the first pulse then an H photon was emitted and there can be no population in $|x-\rangle$ so no emission should occur in both emission regions of the same shot. As before the normalization is determined by correlating with distant shots.

$P(x-|H)$. The initialization and first excitation are the same as before, however, the additional 250 ps pulse acts as a readout for $|x-\rangle$. If a detection occurs after the first 250 ps pulse, then we should expect nothing in the second since the QD is now in state $|x+\rangle$. The anti-correlation is seen by correlating detection in the first 250 ps pulse with the second and is normalized by correlating with second pulses from distant shots of the experiment. The anti-correlation signals are seen in Fig. 5.5. A summary of all four x basis conditional probabilities is shown in Fig. 5.8a.

5.5 Rotated Basis Correlations

As stated before the z basis measurement is more complicated since it is time dependent, allowing the measurement of two conditional probabilities at the same time. Since we wish to look for $P(z\pm|\sigma+)$ and $P(z\pm|\sigma-)$ polarization projection along a circular axis (e.g. $\sigma+$) is required, and the orthogonal circular polarization (e.g. $\sigma-$) must be the input, so we can reject the excitation lasers. The experimental sequence begins in the same way as the x basis; a 4 ns optical pumping pulse initializes to $|x-\rangle$. Next, a 250 ps π pulse transfers the QD population to $|T_x-\rangle$ where the system decays generating the entangled photon. The photon is then polarization

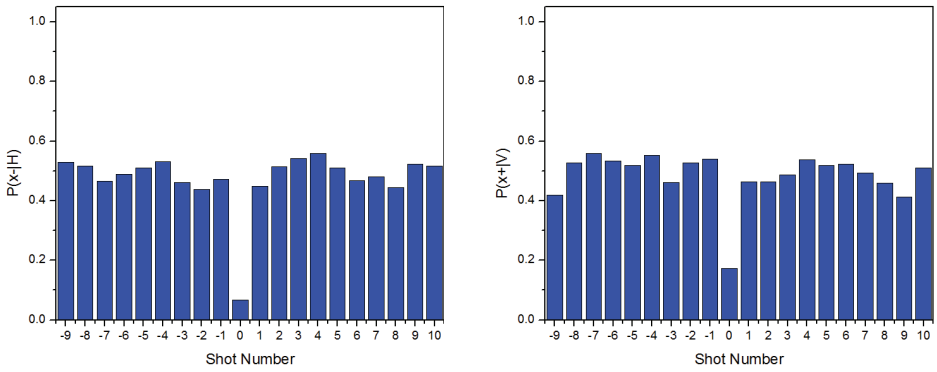

Figure 5.5: conditional probability data for $P(x-|H)$ and $P(x+|V)$ where the distant shot number is label and the average correlations between a photon in the emission region of shot 0 and a spin readout photon from all distant shots, have been set to 1/2.

selected leaving the system momentarily in $|z+\rangle = (|x+\rangle - |x-\rangle)/\sqrt{2}$ or $|z-\rangle = (|x+\rangle + |x-\rangle)/\sqrt{2}$. However, the spin begins to precess under unitary time evolution about the x axis until it is rotated into a population (into $|x+\rangle$ or $|x-\rangle$) by a $\pi/2$ Raman pulse. The spin rotation is achieved by using a detuned broadband pulse driving a two-photon transition. Since the rotation pulse is circularly polarized it non-destructively couples all the transitions allowing geometrical phase rotation of the QD spin, dependent on the pulse area. The rotation occurs about the optical axis, in our case z[66, 45]. Finally, the optical pumping pulse from the next shot of the experiment reads out the population in $|x+\rangle$. The mathematical description of this sequence is shown below and a timing diagram appears in Fig. 5.6.

$$\langle \sigma \pm |\Psi\rangle = \frac{|x+\rangle \mp |x-\rangle}{2} \tag{5.10}$$

$$U(\tau)\langle \sigma \pm |\Psi\rangle = e^{-i\frac{\Delta_e}{\hbar}\tau}\frac{|x+\rangle \mp |x-\rangle}{2} \tag{5.11}$$

$$|\langle x+|R_{\sigma\mp}(\pi/2)U(\tau)\langle \sigma \pm |\Psi\rangle|^2 = \tfrac{1}{4}(1+\sin\Delta_e\tau) \tag{5.12}$$

Here the projection $\langle x+|$ represents the readout of the $|x+\rangle$ state and the rotation is a $\pi/2$ rotation about the z axis,

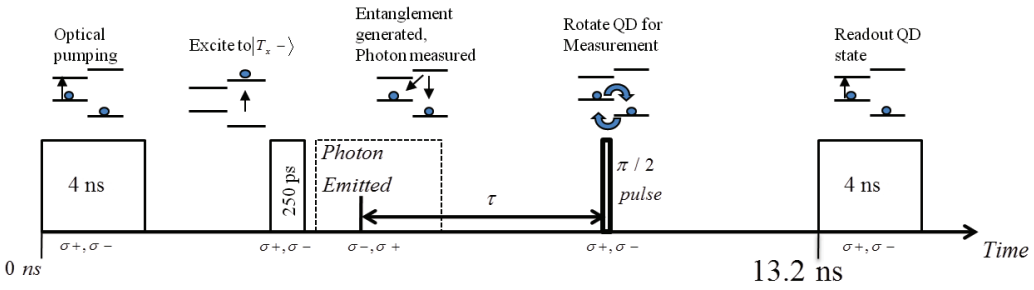

Figure 5.6: Timing diagram for the z (rotated) basis measurement. The entangled photon is emitted randomly along an exponential decay and some time τ later is rotated from a coherence into a population by a detuned $\pi/2$ Raman pulse. The population is $|x+\rangle$ is then readout by the following initialization pulse acting as a readout. Time binning of the emission with respect to the rotation creates an exponentially weighted fringe pattern, which signifies coherent electron precession.

$$R_{\sigma\mp}(\pi/2) = \left[|x+\rangle\langle x+| + |x-\rangle\langle x-| \pm i(|x+\rangle\langle x-| + |x-\rangle\langle x+|)\right]/\sqrt{2}.$$

From this analysis, the time, τ, between emission and detection is crucial, and to observe the frequency of precession, Δ_e (the spin difference frequency), we must utilize a low magnetic field to keep Δ_e smaller than the detector bandwidth. The added complication in choosing the correct magnetic field strength is in the excited state splitting. Since we are using polarization that will couple to all transitions, we must use frequency selectivity to only excite to $|T_x-\rangle$. Taking into account these complications, we use a 1.1T magnetic field giving an excited state and ground state splitting of 4.62GHz and 7.35GHz, respectively. The emission from the excited state will be randomly distributed along the exponential decay, so by time binning the emission with respect to the stationary rotation pulse a fringe pattern will emerge weighted by the exponential decay. This fringe pattern will peak when the time between emission and rotation is sufficient for the Bloch vector to be rotated into $|x+\rangle$ by a $\pi/2$ rotation, and dip when rotated into $|x-\rangle$. This oscillation occurs at the spin difference frequency, Δ_e. After correlating a photon scatter event in the 4 ns pulse with an observed decay after the 250 ps pulse and subtracting out the exponential we can see a fringe signal emerge, where the conditional probabilities can

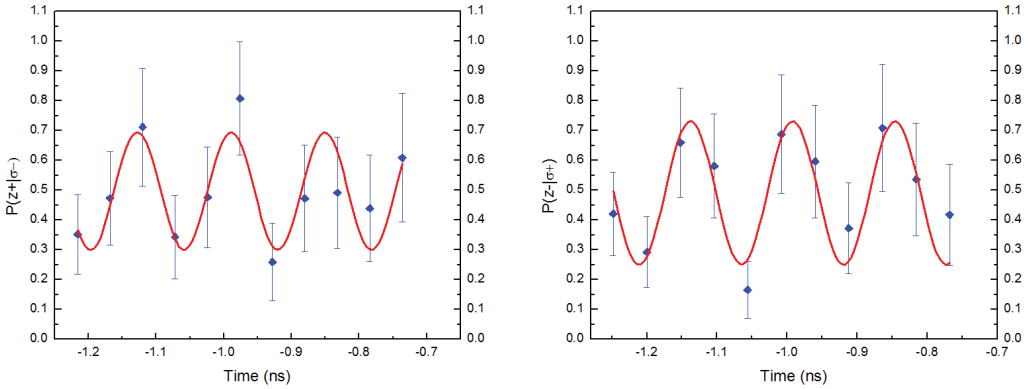

Figure 5.7: The fringe pattern recovered by time binning the photon emission, following the 250 ps pulse when a readout photon is detected as well. This coincidence should only occur at certain times during the electron precession as evident from this fringe pattern. The exponential decay has been divided out to make the fringes easier to observe. A sinusoidal fit recovers the spin precession frequency and reveals the conditional probabilities from the contrast.

be read directly from the fringe contrast (see Fig. 5.7)

By requiring that the conditional probabilities sum to one we can extract the following for the x basis measurement: $P(x+|H) = 0.94 \pm 0.05, P(x-|H) = 0.06 \pm 0.01, P(x+|V) = 0.16 \pm 0.01, P(x-|V) = 0.84 \pm 0.04$. The z basis conditional probabilities are: $P(z+|\sigma-) = 0.69 \pm 0.04, P(z-|\sigma-) = 0.31 \pm 0.04, P(z-|\sigma+) = 0.70 \pm 0.05, P(z+|\sigma+) = 0.30 \pm 0.05$. For both the x and z bases the conditional probabilities combine (see Fig. 5.8) to give a lower bound on the entanglement fidelity, calculated using established techniques [12].

$$F \geq \frac{1}{2} \quad \Big(\rho_{Hx+,Hx+} + \rho_{Vx-,Vx-} - 2\sqrt{\rho_{Hx-,Hx-}\rho_{Vx+,Vx+}} + \rho_{\sigma-z+,\sigma-z+} - \rho_{\sigma-z-,\sigma-z-} + \rho_{\sigma+z-,\sigma+z-} - \rho_{\sigma+z+,\sigma+z+}\Big) \tag{5.13}$$

We find a lower bound on the fidelity of $F \geq 0.59 \pm 0.04$. It is important to note that this lower bound is mostly limited by the fringe contrast in the z basis measurement,

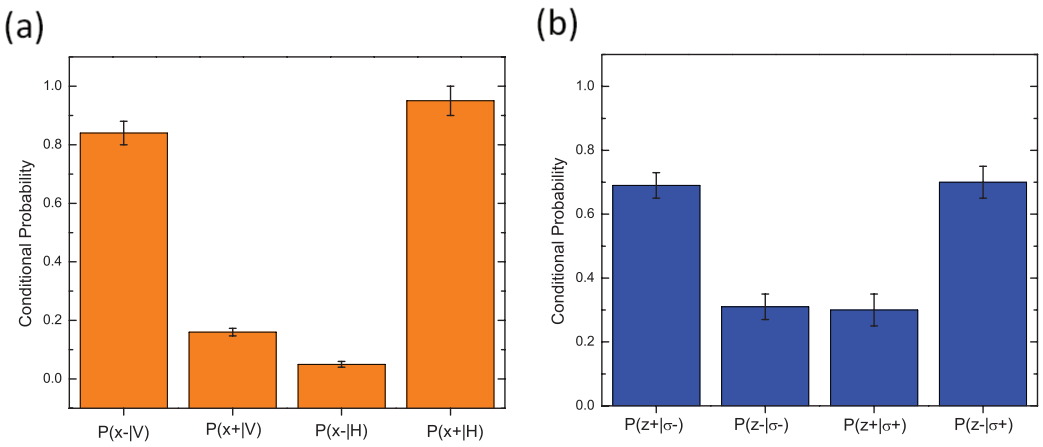

Figure 5.8: The combined conditional probabilities for the (a) x basis, where the probabilities are extracted from previous graphs and constrained to add up to 1n and (b) z basis, where the probabilities are read directly from the fringe contrast.

which is diminished by the finite timing resolution of the detector. In many protocols for entangling multiple quits via interference of the entangled photons, the detector timing resolution is not vital[60, 9].

Here we have shown that the spontaneously emitted photon from a QD is entangled with its spin state, having profound implications to the world of quantum information. QDs have the advantage that they can be easily integrated into an industrial infrastructure designed around semi-conductor fabrication. using on-chip photonics waveguides these entangled photons can be directed to many different quantum nodes making a scalable quantum architecture possible.

5.6 Conclusion

The demonstration that a photon emitted from a QD is entangled with the ground state spin qubit has numerous implications for quantum information. We can now send these photons to any distant node and retain the spin information coded on them. The information transfer is typically mediated by the interference of entangled photons on a Hong-Ou-Mandel (HOM) interferometer, which projects the entangled

matter qubits to a specific state upon coincidence causing them to coherently evolve together[43, 60, 9]. In this way, two separate QDs could be entangled. Also we can use the entangled nature of the emitted photon to teleport information onto the QD spin state [36]. The possible experiments greatly increase when you consider the capabilities for manipulation and coherent control of QDs. Experiments such as these further the case that QDs can indeed be considered viable and useful when considering the future of quantum technologies.

CHAPTER VI

Coherence Properties of QD Radiation

6.1 Introduction

In the previous chapter we verified the entanglement between a photon emitted from a QD and the QD spin state. The next step in developing QDs as a viable quantum information technology is the ability to transport this entanglement to distant places or use the entangled nature to encode quantum information on the QD spin state via intermediate interference of the entangled photon with another photonic state. This interference is conducted using a Hong-Ou-Mandel (HOM) interferometer which will be discussed in detail later in the chapter. The HOM works by exploiting the indistinguishability of two photonic envelopes incident on separate ports of a beam splitter. So we will need to study the properties of the radiation scattered in our system to test for indistinguishability and some other interesting quantum optics measurements will come out of this. However, before any of these experiments can begin we address the limitations inherent in the previous Schottky diode sample used to conduct all measurements up to now. The light collection from this sample is far too low to conduct any of the above mentioned HOM interference experiments. So we move to the sample discussed in 3.3.2 with a DBR mirror behind the QD layer to redirect the radiation in the backward direction.

This chapter discusses the new quantum optics measurements we are capable of

achieving with the increased light collection of the new sample structures. Also we will look into how this can be used to study the coherence properties of the scattered and emitted radiation from these QD structures. The experimental techniques and the results derived from this chapter will be important moving forward with a teleportation scheme using QD spin-photon entangled states.

6.2 New Sample With Higher Light Collection

The sample structure discussed in 3.3.2 provides us with a mirror in the form of alternating AlAs and GaAs layers that act to reflect the radiation back through the excitation beam path. The PL techniques used here are identical to those previously discussed in 4.3. A sample spectrum and bias dependent PL map are provided for comparison in figures 6.2 & 6.1, respectively.

The absorption measurements differ in that they are taken in the reflection geometry so it is slightly unclear how to interpret the results. A schematic of the reflection geometry homodyne measurement is given in figure 6.3. The homodyne detection scheme we use in transmission relies on the fact that the interacting (part that induces absorption in the QD) and non-interacting part of the laser field are co propagating so the phase of the signal can be well understood. In the reflection geometry there are many surfaces that the laser field can reflect off of (the top surface, or any one of the DBR layers) that can affect the phase of the signal. Since all the reflections and the part of the laser field that interacts with the dot will be mixed on the APD we cannot necessarily trust the phase of the signal. Due to the ambiguity of the signal, we only use the lock-in homodyne signal as a more accurate measure of the trion transition frequency and bias existence range. An example of a DR/R (homodyne) scan is given in figure 6.4

As stated above the previous techniques (PL and DR/R) serve quite well to identify the QD resonance, but due to ambiguities in the lock-in signal the best way for

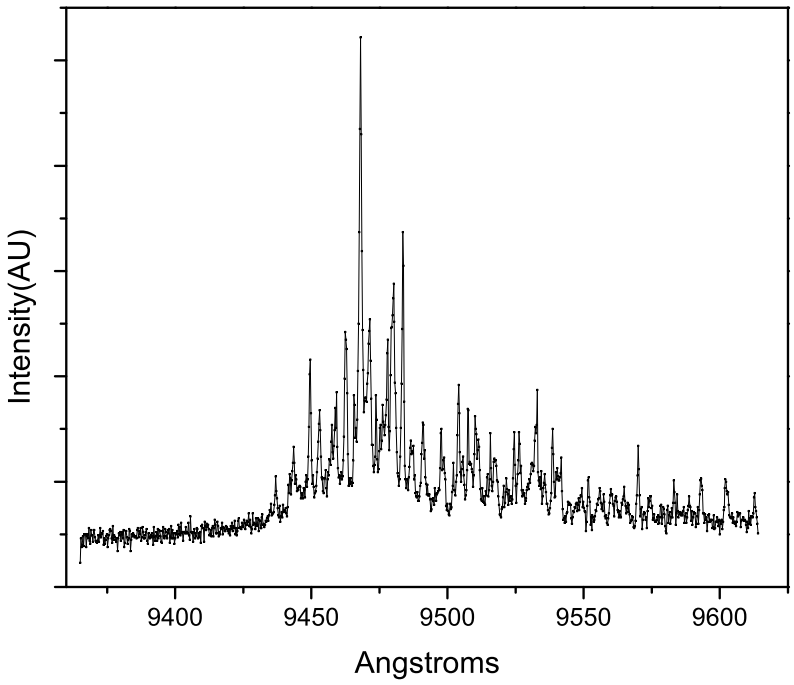

Figure 6.1: A single PL spectrum from the DBR sample. We can see that there are many dots in this region so care must be taken to identify and readout a single dot.

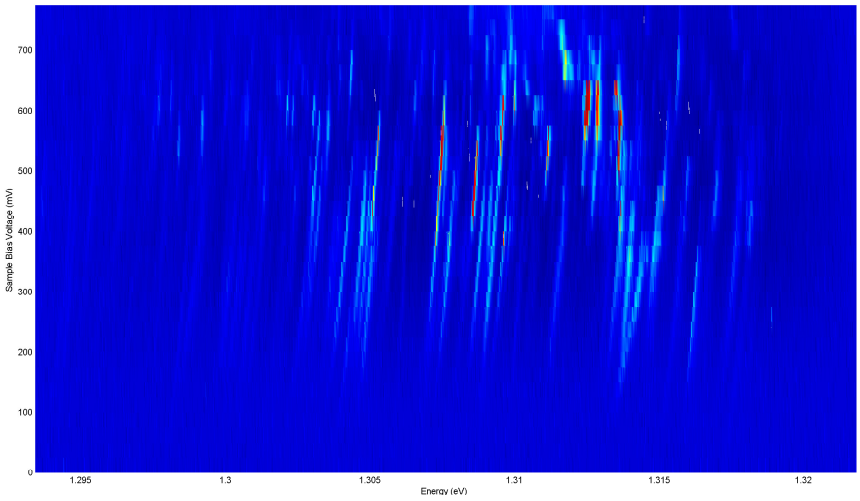

Figure 6.2: A bias dependent PL map taken on the DBR sample. As the bias across the dot layer is scanned spectra are taken indicating the charging of the QD states and allow us to identify good candidates for negatively charged QDs.

us to more accurately study the properties of the trion is to look at resonant Rayleigh scattering. The theory of this was developed previously in 4.6. A sample Rayleigh scattered scan is provided in figure 6.2. This spectrum is taken by scanning the laser across the trion resonance and using a 90:10 beamsplitter to collect 90% of the scattered radiation from the QD transition (set-up shown in figure 6.2). Of course 90% of the reflected laser light is also present on top of the desired signal, so we use a polarizer set orthogonal to the input polarization is used to filter out the excitation laser similar to how we took data in the Schottky diode sample. To provide additional rejection we use a single mode (SM) fiber as a spatial filter. The reason a spatial filter helps with polarization rejection is that the polarization vectors become altered compared to the other parts of the wavefront are diffracted by the high curvature of the focusing asphere. If we try to use just polarization as the filtering mechanism and image the beam we can clearly see what is known a Maltese cross pattern, shown in figure 6.2, where the parts of the beam hitting the outer parts of the lens have a

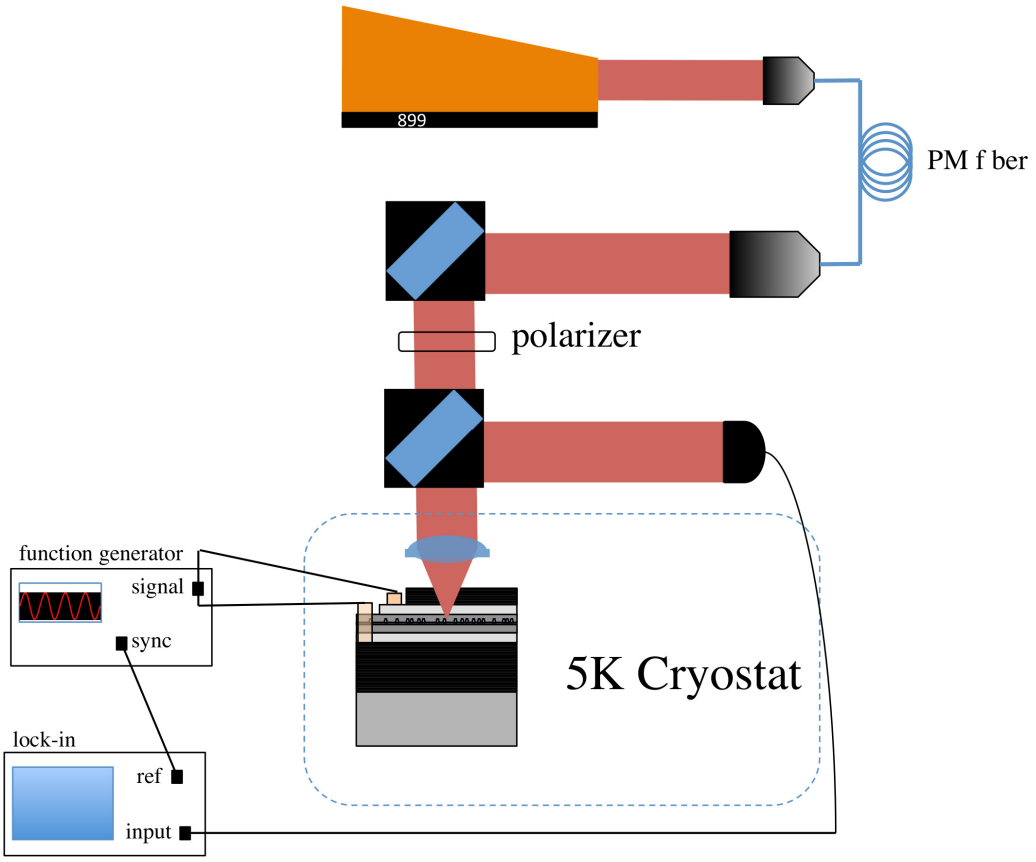

Figure 6.3: The set-up for a homodyne detection scheme in the reflection geometry. The measurement of merit will be the change in reflection on resonance over the laser reflection intensity or DR/R.

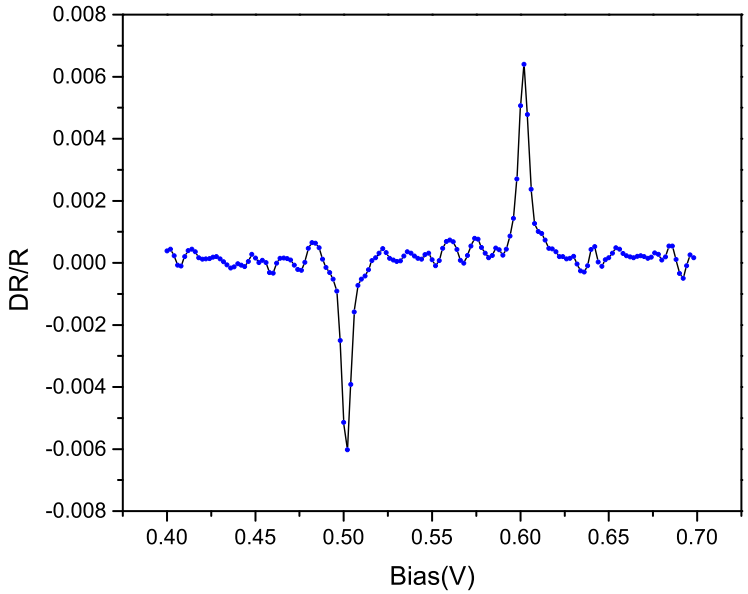

Figure 6.4: A sample scan of DR/R spectrum where the bias across the QD layer is modulated and scanned while the laser frequency is fixed. The methods of detection are identical to those used in the previous DT/T measurements.

different polarization than the center. By using a spatial filter we reject these bright lobes and only allow the scattered radiation of interest through to the detector. After the rejection techniques we can now observe the scattered radiation using a single photon detector and by performing background subtraction we are left with a clean Lorenztian line shape as the excitation laser scans across the trion resonance (figure 6.2). One key difference in the Rayleigh scattered spectra is that with the DBR sample the peak counts are close to 300kcps as opposed to 4kcps when using the Schottky diode sample for similar Rabi frequencies. So, with the new sample structure we are able to increase the counts in the collection channel by almost a factor of 100. This increase makes it possible to extend the spin-photon entanglement more complicated experiments requiring more than a two-fold coincidence, such as teleportation and distant QD entanglement. Before we move into the discussion of teleportation there are a few interesting quantum optics experiments now possible using the newly

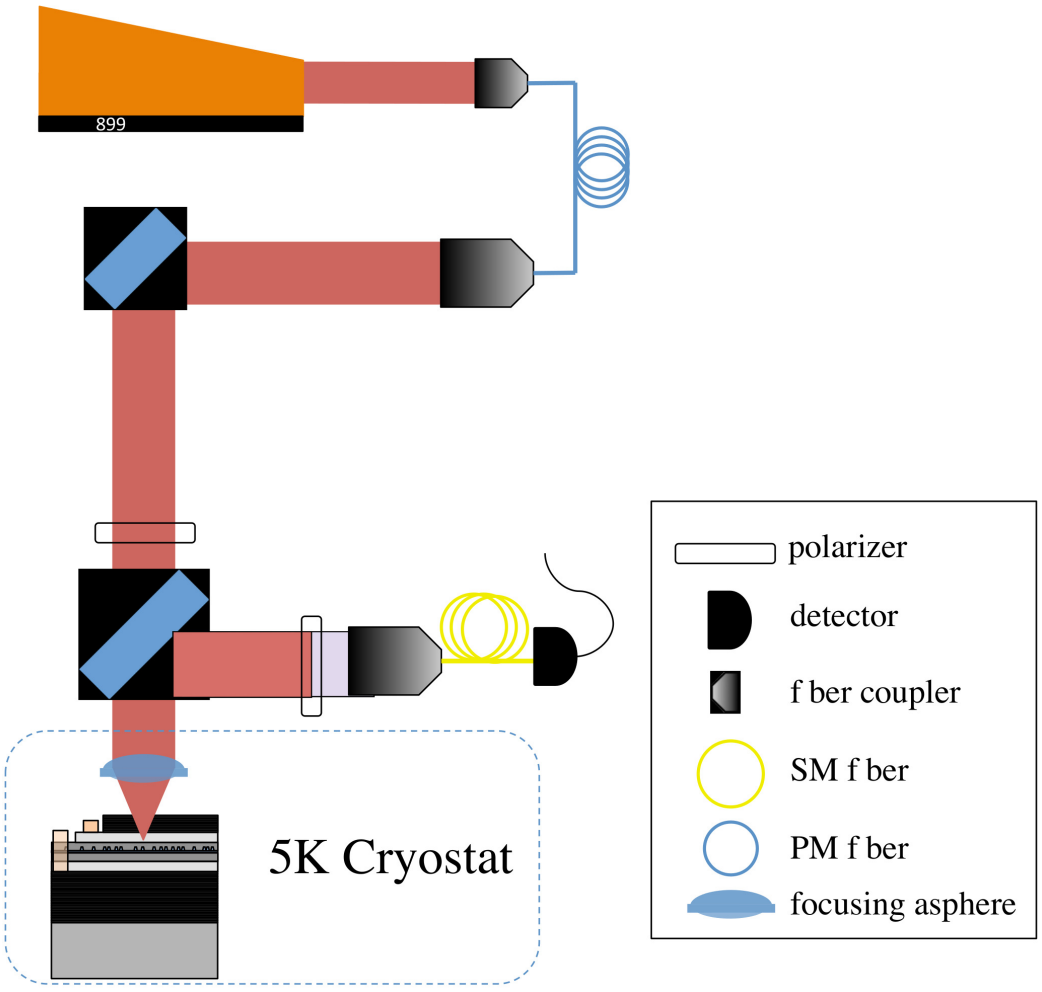

Figure 6.5: Set-up used to take resonant Rayleigh scattering in the reflection geometry.

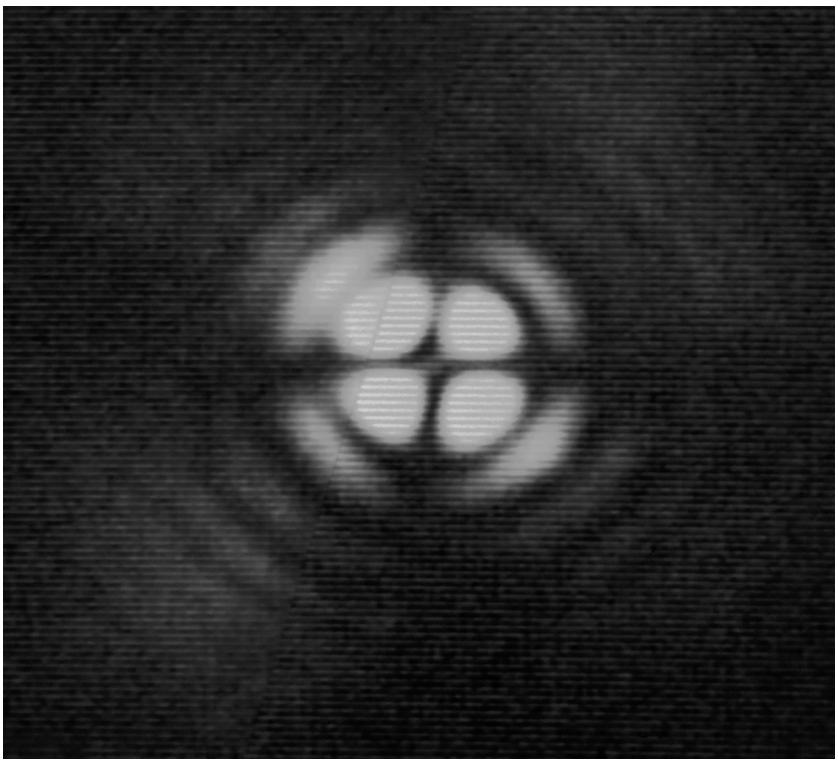

Figure 6.6: Image of The Maltese cross created by the depolarization of the outer parts of the laser wavefront induced by the edges of the high curvature focusing lens. By using a spatial filter we can collect only the signal from the middle and reject the depolarized outer parts of the beam.

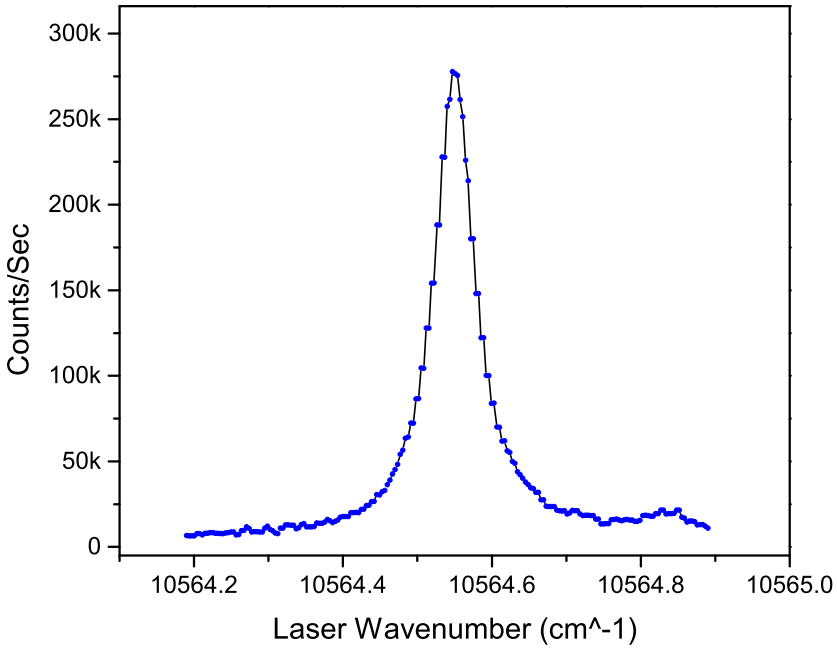

Figure 6.7: A sample Rayleigh scattering scan showing the QD trion transition at zero field. The peak counts increase by a factor of 50 to 100 times for a similar Rabi frequency as the Schottky diode samples.

improved light collection.

6.3 Observation of the Mollow Triplet

The above mention Rayleigh scattering is sometimes referred to as resonance fluorescence in the literature. Fluorescence evokes the idea of emission and while there are certain situations throughout this work where emission is the proper way to model the observed process, such as in the creation of the spin-photon entangled state from 5.5 or in the lifetime measurement of figure 4.14, this is not always the proper language. A common misconception is that the radiation collected during a CW scan are emitted from the QD and occur at the QD resonance frequency. In fact the theory for CW excitation reveals that, in the low power limit, the radiation is scattered at the driving laser frequency, so a more apt name would be to call this process resonant Rayleigh scattering [7]. As the power is increased however, a frequency resolved emission spectrum reveals the onset of in-elastic scattering in the form of the Mollow triplet, reported earlier in QDs [64, 61].

Previous studies in our lab have investigated the Mollow triplet spectrum by using a pump probe approach, but we have never before observed it directly in the scattered radiation spectrum [85]. The best way to begin the discussion of this phenomenon is to start with a theoretical discussion of the in the atom-field picture. We can begin by looking at the Hamiltonian in the rotating wave approximation,

$$\begin{aligned} H &= \frac{\hbar\omega_0}{2}\sigma_z + \sum_{k,\mathbf{k}} \hbar\omega_k a^\dagger_{\mathbf{k}} a_{\mathbf{k}} + \hbar\chi(\sigma_+ e^{-i\omega t} + \sigma_- e^{i\omega t}) \\ &\quad + \sum_{\mathbf{k}} \hbar(g_{\mathbf{k}}\sigma_+ a_{\mathbf{k}} + g^*_{\mathbf{k}}\sigma_- a^\dagger_{\mathbf{k}}) \end{aligned} \tag{6.1}$$

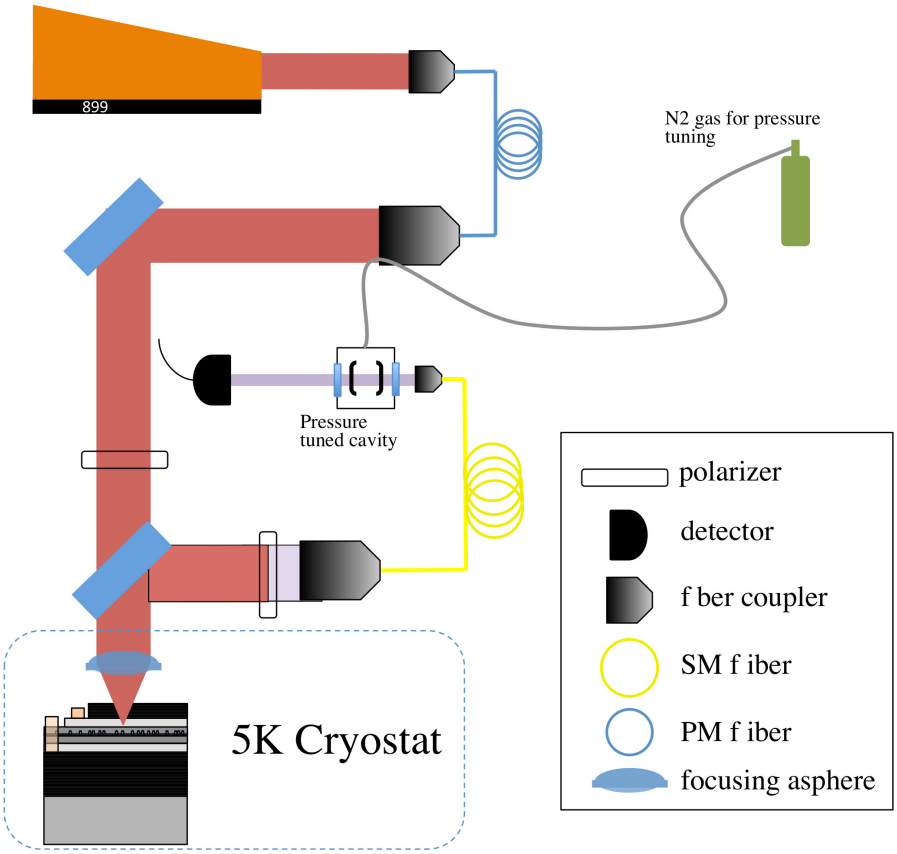

Figure 6.8: The optical diagram for taking frequency resolved data. The pressure tuned cavity is adjusted by using a computer controlled valve to scan the pressure in the cavity and change the pass frequency across the entire free spectral range of 40GHz with a linewidth of 400MHz

Where χ is half the Rabi frequency and,

$$g_{\mathbf{k}} = -i\mu_{21}\sqrt{\frac{\omega_k}{2\hbar\epsilon_0 V}}\sin\theta_{\mathbf{k}}. \tag{6.2}$$

A detailed calculation of the spectrum is carried out in several quantum optics texts [7, 74]. In typical Rayleigh scattering the scattering process is calculated to out to first order in the applied field and the result is scattered radiation at the laser drive frequency ($\omega = \omega_k$ from conservation of energy) . The state amplitudes that remain to first order go like,

$$\dot{c}_{2;0} = -\frac{\gamma_2}{2}c_{2;0} - i\chi e^{i\delta t}c_{1;0} \tag{6.3}$$

$$\dot{c}_{1;\mathbf{k}} \approx -ig_{\mathbf{k}}e^{i\delta_k t}c_{2;0} \tag{6.4}$$

Using the convention from [7], where ω_0 is the transition frequency, $\delta = \omega_0 - \omega$ and $\delta_k = \omega_0 - \omega_k$, with $c_{1;\mathbf{k}}$ describing the QD in state 1 and the field in state $\mathbf{k}$. Recall, that γ_2 is the longitudinal decay rate and the transverse decay rate is given by $\gamma = \gamma_2/2$. Carrying through the calculation reveals that for long times, to remove transient effects, the scattered spectrum occurs at the laser frequency as expected.

However, this calculation can be carried out to additional orders in the field which gives rise to additional intermediate resonance states with scattering symmetric about the laser frequency. This process is seen in figure 6.3. Of interest is the case where three separate frequency components are present in the scattered field spectrum (Mollow triplet) having the resonance condition $3\omega - \omega_A - \omega_B - \omega_C$. The intermediate resonances cases go like,

$$\gamma \gtrsim |2\omega - \omega_A - \omega_0| \tag{6.5}$$

$$\gamma \gtrsim |3\omega - \omega_A - \omega_B - \omega_0| \tag{6.6}$$

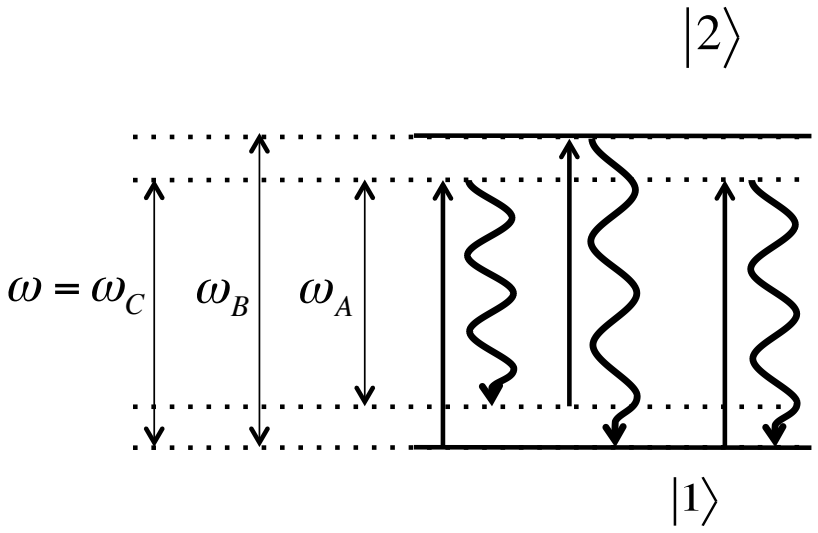

Figure 6.9: Cartoon of a multi-field scattering process ω_C is the laser frequency and the red and blue shifted sidebands are ω_A and ω_B.

From this we get three peaks in the scattered spectrum centered about the laser drive frequency forming the Mollow triplet. Where ω_B and ω_A form the blue and red detuned sidebands, respectively, and ω_C corresponds to the laser frequency. The sidebands are inelastic scattering events and the central peak contains both the inelastic and elastic components. Including higher order scattering events only adjusts the position of the sidebands and to extract information from the widths and weights of the spectrum requires a calculation out to all orders in the field. Since our experimental apparatus is limited to low resolution scans, the presence of the Mollow triplet peaks and their dependence on input power, as expected, is the result of merit in this experiment.

The data is taken by setting a CW laser on resonance with the QD's trion transition and collecting the scattered radiation. A pressure-tuned etalon is used to frequency resolve the emission from the QD after we filter out the excitation laser. An optical diagram of the experiment can be found in figure 6.3. The etalon has a linewidth of 400MHz so high resolution scans are not possible in the current configuration. As it stands now the line shapes extracted will be a convolution of the

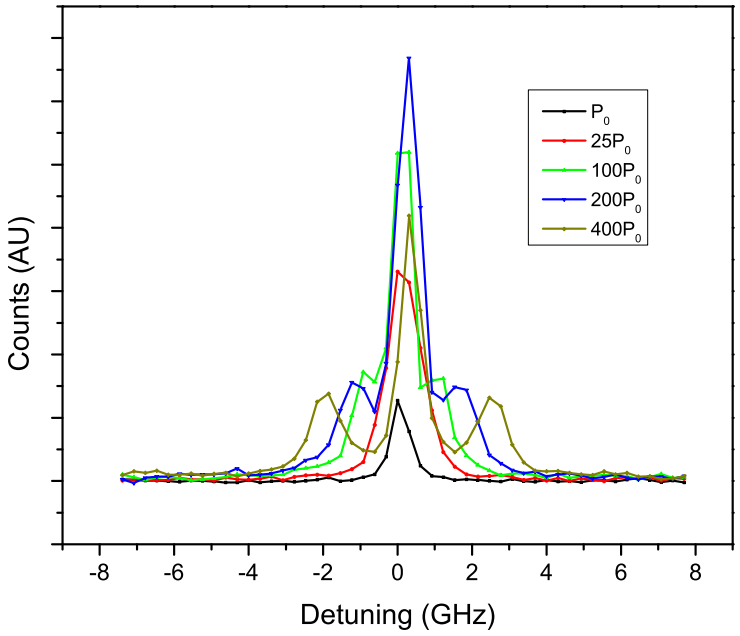

Figure 6.10: Frequency resolved Resonance fluorescence from the QD trion transition. The laser is fixed on resonance and a pressure-tuned etalon is scanned through the resonance with a linewidth of 400MHz, so high resolution scans are not available and the resulting spectrum is a convolution of the linewidth of the trion transition and the etalon. Even with this limitation we can still see clear sideband emerge as the driving radiation field is increased far beyond saturation.

instrument response of the etalon and the actual linewidth of the state. From the data we can see the expected dependence of the sidebands on the increasing power of the drive field. Future directions might include a high resolution scan of the Mollow spectrum and compare that to the transient measurements of γ and γ_2 extracted in previously in 4.7.

6.4 Indistinguishability of QD Radiation

The study of indistingushability is an important tool when considering quantum coherence and applications to quantum technologies. Photons provide an attractive

carrier of quantum information due to their robustness against decoherence when compared to other technologies. The coherence properties of QD scattered and emitted radiation have been studied in the past to determine the single emitter nature of the QD and the purity of the emitted field. [58, 62, 78, 70, 94]. For the case of our system the ability to show the single emitter nature is essential and was done previously in this work (see figure 4.12). Our group up to this point has not studied the indistinguishability of radiation from the QD and this is an important step moving forward. The ultimate goal of teleportation relies on the interference of field envelopes from different sources which necessitates the investigation of the level of indistinguishability present in the individual sources themselves.

6.4.1 Theoretical Background

The indistinguishable interference of interest occurs when overlapping photon envelopes enter a 50/50 beam splitter and exit through the same port [43, 31]. The theoretical description of the beam splitter gives an insight to why this should be the case. The following theoretical discussion uses input and output states described using single kets and creation and annihilation operators. It is crucial to note that this is not strictly the true since the emitted radiation field from the QD is a multi-mode field owing to the bandwidth associated with the decay process. The multi-mode nature of the field affects the indistinguishability measurement in the form of noise in the coincidence spectrum and is observed as a rise in coincides above zero centered about zero delay, which can be observed in figure 6.4.3.

If we first consider two photon envelopes incident on two different input ports of a beam splitter, as seen in figure 6.4.1, then we can write down all the cases that can occur in this geometry. We start by describing the input and output ports of the beam splitter using creation operators. In a simple case, if we have an input state in the a port described by $|1\rangle_a$ we can also write this as $a^\dagger|0\rangle_a$. The output case is

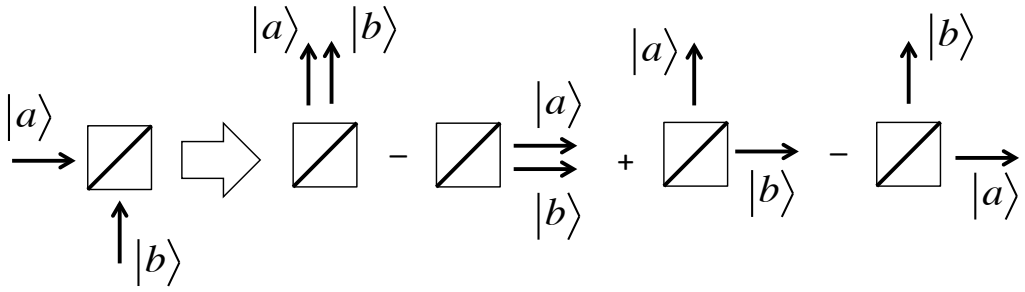

Figure 6.11: This figure depicts the possible output configurations for two input single photon envelopes incident on a 50/50 beam splitter. For the case where *keta* and $|b\rangle$ are overlapping in frequency, polarization, timing, and spatial distribution, then both states will exit the same port of the beam splitter, a phenomenon measured by a drop in coincidence when detecting the outputs of the beam splitter.

then a probabilistic superposition of the creation operators for each output state of the beam splitter ($c^\dagger$ and $d^\dagger$).

$$\frac{c^\dagger + d^\dagger}{\sqrt{2}}|0\rangle_{cd}. \tag{6.7}$$

For the case where we have a photon present at each input port of the beam splitter, we will use $b^\dagger$ to describe the creation of a photon in the second input port and we are left with the input state,

$$|1,1\rangle_{ab} = a^\dagger b^\dagger |0,0\rangle_{ab}. \tag{6.8}$$

The beam splitter acts like a unitary transformation on the input states given by,

$$U(a,b \to c,d) = \begin{pmatrix} 1 & 1 \\ 1 & -1 \end{pmatrix}. \tag{6.9}$$

Now the new output states are given by the following creation operators,

$$\frac{c^\dagger + d^\dagger}{\sqrt{2}}|0,0\rangle_{cd} \quad \text{and} \quad \frac{c^\dagger - d^\dagger}{\sqrt{2}}|0,0\rangle_{cd} \tag{6.10}$$

for a and b inputs respectively. So if we consider the case of Eqn. 6.8 and use Eqn. 6.10 then we are left with the following output configuration,

$$\frac{1}{2}(c^{\dagger 2} - d^{\dagger 2} \underbrace{-c^{\dagger}d^{\dagger} + d^{\dagger}c^{\dagger}}_{-[c,d]})|0,0\rangle_{cd} \tag{6.11}$$

Due to the bosonic nature (symmetric under exchange) of photons the commutator $[c,d]$ vanishes leaving,

$$\frac{c^{\dagger 2} - d^{\dagger 2}}{2}|0,0\rangle_{cd}. \tag{6.12}$$

The result of this indicates that there is a random but equal probability that both states will exit either c or d but never both at the same time for identical input states a and b. So, for overlapping input photonic states we should see no coincidence counts when detectors are placed on each output port of the beam splitter [43, 10, 56, 69]. Verifying that the single photons from our QD are indistinguishable is critical for any teleportation protocol relying on intermediate interference as ours does [37, 65, 75, 13]. Section 6.4.3 provides the data confirming the indistinguishability from the QD, but before this it is useful to develop the theory for HOM interference when the input states of a beam splitter have different frequency or polarization field components..

6.4.2 Qubit Interference in a HOM

The teleportation protocol we use, and in fact many of the other entanglement swapping protocols used in previous experiments, rely on the interference of entangled photonic qubits [13, 60, 23, 8]. A single qubit state can be described by a two-dimensional Hilbert space, however, if we look at the interaction of two separate qubits, one in each arm of a beam splitter then we must describe this combined system using a four-dimensional Hilbert space [57, 55]. We use a polarization basis to describe the qubits but the extension to frequency qubits, which we use in the teleportation protocol, is trivial. If we take the two input states to be the following

photonic polarization qubits,

$$|\psi\rangle_1 = \frac{|H\rangle_1 + |V\rangle_1}{\sqrt{2}} \quad \text{and} \quad |\psi\rangle_2 = \frac{|H\rangle_2 + |V\rangle_2}{\sqrt{2}} \tag{6.13}$$

Then the new Hilbert space can be written using four new states,

$$\begin{aligned}
|\Psi^+\rangle &= \frac{1}{\sqrt{2}}\left(|H\rangle_1|V\rangle_2 + |V\rangle_1|H\rangle_2\right) \\
|\Psi^-\rangle &= \frac{1}{\sqrt{2}}\left(|H\rangle_1|V\rangle_2 - |V\rangle_1|H\rangle_2\right) \\
|\Phi^+\rangle &= \frac{1}{\sqrt{2}}\left(|H\rangle_1|H\rangle_2 + |V\rangle_1|V\rangle_2\right) \\
|\Phi^+\rangle &= \frac{1}{\sqrt{2}}\left(|H\rangle_1|H\rangle_2 - |V\rangle_1|V\rangle_2\right).
\end{aligned} \tag{6.14}$$

These are the famous Bell states for a four dimensional Hilbert space, sometimes called the Bell basis [5]. A crucial thing to note is that only one of these states is antisymmetric under particle exchange, $|\Psi^-\rangle$. For indistinguishable states the total wavefunction for each case should be symmetric, leading to an anti-symmetric spatial distribution for the case of $|\Psi^-\rangle$[35]. If a and b indicate the spatial configuration of the input states, then the following are the resultant sates for two qubits incident on two input ports of a beam splitter,

$$\begin{aligned}
|\Psi^+\rangle &= \frac{1}{\sqrt{2}}\left(|H\rangle_1|V\rangle_2 + |V\rangle_1|H\rangle_2\right)\left(|a\rangle_1|b\rangle_2 + |b\rangle_1|a\rangle_2\right) \\
|\Psi^-\rangle &= \frac{1}{\sqrt{2}}\left(|H\rangle_1|V\rangle_2 - |V\rangle_1|H\rangle_2\right)\left(|a\rangle_1|b\rangle_2 - |b\rangle_1|a\rangle_2\right) \\
|\Phi^+\rangle &= \frac{1}{\sqrt{2}}\left(|H\rangle_1|H\rangle_2 + |V\rangle_1|V\rangle_2\right)\left(|a\rangle_1|b\rangle_2 + |b\rangle_1|a\rangle_2\right) \\
|\Phi^+\rangle &= \frac{1}{\sqrt{2}}\left(|H\rangle_1|H\rangle_2 - |V\rangle_1|V\rangle_2\right)\left(|a\rangle_1|b\rangle_2 + |b\rangle_1|a\rangle_2\right).
\end{aligned} \tag{6.15}$$

From this we see that $|\Psi^-\rangle$ can be differentiated from the other states due to its spatial wavefunction. Coincidence clicks (a photon in each output port of a beam

splitter) will occur only in the case of an anti-symmetric input spatial state and therefore project the input field to the anti-symmetric state, $|\Psi^-\rangle$. As we will see in the next chapter the projection to the anti-symmetric bell state results when the qubits are orthogonal and if another state (a QD spin state) is entangled with one of the qubits then the entangled state becomes orthogonal to the other qubit state. This process is referred to as teleportation since the information from one photonic qubit is transferred to the state entangled with the other photonic qubit via orthogonal projection.

This result will become crucial in chapter VIII when we discuss the teleportation protocol. The ability to distinguish a single photonic state from the four possible is used to herald successful teleportation. Since the coincidence can only occur for the case of an anti-symmetric photonic Bell state then we are confident that a projection to this state has occurred [60].

6.4.3 HOM Between Successively Emitted QD Radiation

The following describes the experiment to determine indistinguishability of QD Radiation. This data is taken in the time domain so we use a 250ps pulse from an electro-optic modulator to excite the trion state similar to the technique used in section 4.7 and the optical diagram in figure 4.13. The time-gated fluorescence from the QD is now split into two arms, say l_1 and l_2. These two paths are then recombined on a beam splitter, which will serve as the HOM interferometer. The path length of l_2 is delayed in such a way that if a photon packet enters l_2 and another photon packet generated in the next shot of the experiment goes through l_1 then they will arrive on the beam splitter at the same time, or $l_2 = l_1 + c\tau$. Where c is the speed of light and τ is the repetition rate of the EOM generated pulse. A schematic of this experiment can be found in figure 6.4.3. By adjusting the input polarization on the beam splitter input we are able to alter the polarization component of the input field and show that

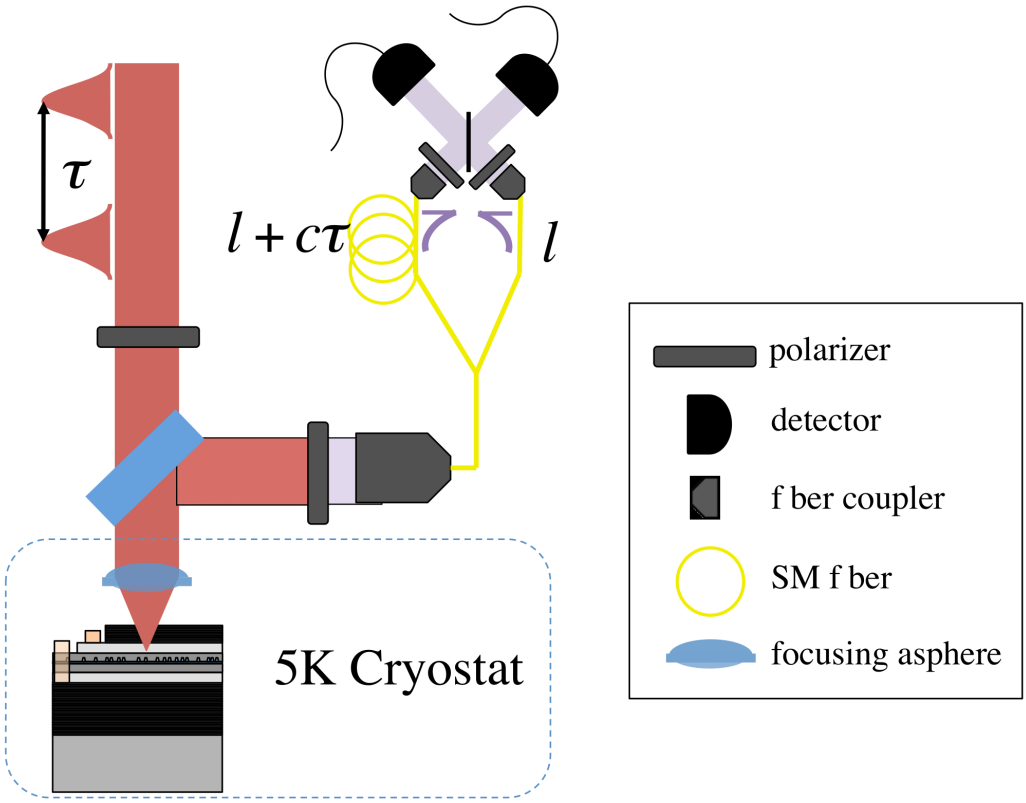

Figure 6.12: HOM setup for checking indistinguishability of QD radiation. The dot radiation is split by a fiber beam splitter and one of the lengths is delayed such that an event from the next shot of the experiment will interfere with it on the beam splitter. The polarizers on the output are used to control the polarization state of the beam splitter inputs since polarization is one of the characteristics that must be identical for interference.

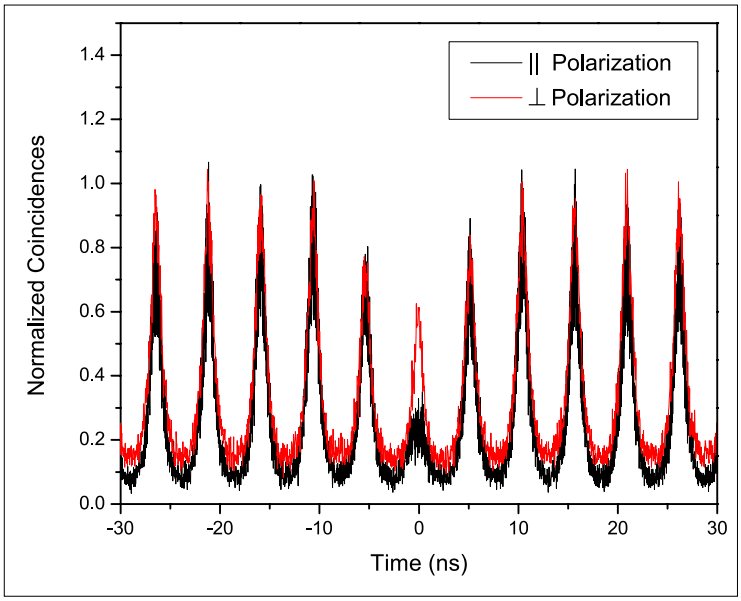

Figure 6.13: HOM data for a QD interfering with itself. The field emitted from the one shot of the experiment is interfered with a field from a delayed shot of the experiment. By adjusting the polarization states of the HOM input ports we can show that when the fields have different polarizations they are distinguishable and the coincidence at time zero increases. Alternatively, for the case where the fields are indistinguishable we can see that the coincidence at time zero drops significantly.

for the same or parallel polarization ($\parallel$) the fields should show no coincidences at similar arrival times. If we set the polarization of the beam splitter inputs orthogonal to eachother ($\perp$) then the photon states will be distinguishable and the coincidences will rise. Data showing this effect is given in figure 6.4.3. The data is taken using a start-stop photon counting method similar to previous work [36, 33, 38]. The two pulses are overlapped by looking at a histogram of the pulse arrival times on the beam splitter, where a delay in one of the arms can be adjusted to achieve good temporal overlap of the QD decay packet. Once the timing of the photon packets on the beam splitter is set we integrate data for an hour to build good statistics and analyze. By using a start stop technique we can see that the events cluster in discrete time bins corresponding to arrival. The distance between them is the repetition rate of the

experiment. In the case where the polarizations are parallel the coincidences should go to zero so the number of counts in the zeroth time bin is dramatically reduced compared to when we look at longer times which should average out to one similar to a intensity correlation measurement ($g2(0)$). As expected, when the polarizations are perpendicular the coincidences at time zero increase due to the distinguishability of the input radiation.

6.5 Conclusion

In this chapter we have looked at a new sample that enables us to get much higher counts by almost a factor of 100 better than the previous samples. This enables us to study the properties of our QD system even better than before. We are able to recover the Mollow triplet by frequency resolving the scattered radiation from the QD transition, which, up to now was done using pump-probe methods in our lab instead of direct detection. We are also able to show HOM interference between successively emitted pulses from the trion state; and though the emitted radiation is by nature multi-mode we can still recover the dip in coincidences at zero delay predicted by the quantum model of the beam splitter. We determined that the QD radiation shows a high degree of indistinguishability that is crucial for further experiments involving teleportation. Finally, qubit interference was discussed in the context of a HOM measurement. These results will be important in the teleportation work later in the thesis.

CHAPTER VII

Spontaneous Parametric Down Conversion

7.1 Introduction

This chapter will discuss the physics behind spontaneous parametric down conversion (SPDC) and how we will utilize it as a source of single photons for teleportation. The teleportation experiment, discussed in detail in the next chapter, will utilize the single photons created in the SPDC process to teleport information onto the QD spin state. This is achieved by means of interference of an SPDC photon with the photon from the spin-photon entangled state of the QD, discussed in chapter V. For the teleportation protocol we only require the fact that the SPDC system can be made into a high brightness source of single photons. In expanding beyond the teleportation discussed in this thesis the fact that photon pairs created in SPDC can be entangled allows us to extend the teleportation protocol to entangle two distant QDs. In the following discussions we will outline the theory of SPDC, how we can increase the output intensity using a cavity and the entangled nature of the photon pairs that are created.

The high brightness SPDC source we will use to generate the photon states to be teleported onto the QD spin is built at the University of Illinois In Paul Kwiat's lab. We currently have a collaborative effort with this group to achieve the goal of teleportation and beyond using the SPDC source.

7.2 Theoretical Background

From non-linear optics, we know that the optical response of a medium is given by the polarization ($\tilde{P}$)represented as a power series in the applied electric field $\tilde{E}(t)$,

$$\tilde{P}(t) = \chi^{(1)}\tilde{E}(t) + \chi^{(2)}\tilde{E}^2(t) + \chi^{(3)}\tilde{E}^3(t) + ... \tag{7.1}$$

Where the $\chi^{(i)}$s are referred to as the ith order optical susceptibilities [15]. The linear susceptibility $\chi^{(1)}$ contributes to well known effects like the index of refraction of a material and the higher order term contribute to non-linear properties like, second harmonic generation (SHG) [34] and SPDC for $\chi^{(2)}$; and third harmonic generation and four-wave mixing for $\chi^{(3)}$. Since the $\chi^{(2)}$ non-linear susceptibility gives rise to the SPDC effect we are interested in exploiting for the teleportation experiment this is what we will be the focus. One important aspect here is that $\chi^{(2)}$ vanishes for media possessing inversion symmetry. This fact can be easily seen by looking at an applied electric field $\tilde{E}(t) = E_0 \cos\omega t$ where if we change $\tilde{E}$ to $-\tilde{E}$ then the polarization must change sign as well. Taking this to its mathematical conclusion we find that,

$$\tilde{P}(t) = -\tilde{P}(t) = \chi^{(2)}\tilde{E}^2(t), \tag{7.2}$$

which can only occur in the case where $\tilde{P}(t) = 0$. So the crystal structure used to generate the photon pairs must lack inversion symmetry.

In the case of SPDC we are looking to create two photons from an input pump beam. By convention these photons are called the signal and the idler and due to conservation they must satisfy the following phase matching conditions,

$$\mathbf{k}_p = \mathbf{k}_s + \mathbf{k}_i \tag{7.3}$$

and

$$\omega_p = \omega_s + \omega_i. \tag{7.4}$$

The photons generated in this process must be created in pairs otherwise we are left with a coherent state and any kind of single photon interference techniques we wish to use are ineffectual due to the large number of modes present in the field. For SPDC or spontaneous parametric fluorescence, as many older text refer to it, the fact of simultaneous photon creation has been verified for some time [17]. For our case it is instructive to briefly discuss how this comes about. A more detailed description of this is provided in Yariv's *Quantum Electronics* text book [92]. The parametric florescence effect we are looking for arrives from a quantum description of the output fields of frequency ω_s and ω_i, however the intense pump can still be described classically. Using the Polarization of a medium we can write an expression for the energy function using,

$$\mathbf{P} = -\nabla_E U(\mathbf{E}) \tag{7.5}$$

and we can write $U(\mathbf{E})$ as,

$$U(\mathbf{E}) = -\frac{\epsilon_0}{2}\chi_{ij}E_iE_j - \frac{2\zeta_{ijk}}{3}E_iE_jE_k + ... \tag{7.6}$$

Where the χ and ζ are the tensor non-linear susceptibilities discussed previously. The second term in the expression will serve as the Hamiltonian density for the parametric interaction of interest and we us the pump electric field is given by, $E_p(\mathbf{r}, t) = E_p(\mathbf{r})\cos\omega_p t)$,

$$H = \int_V U(\mathbf{E})dv = g\hbar\cos\omega_p t(a_s^\dagger - a_s)(a_i^\dagger - a_i) \tag{7.7}$$

Here $a^\dagger$ and a are the creation and annihilation operators for the field modes of the

signal and idler, and g represents the following,

$$g = \frac{\zeta}{3}\sqrt{\frac{\omega_s \omega_i}{\epsilon_s \epsilon_i}} \int_V E_p(\mathbf{r}) E_s(\mathbf{r}) E_i(\mathbf{r}) dv \tag{7.8}$$

We can solve for the equations of motion in the Heisenberg representation and find,

$$\dot{a_s}^\dagger = i\omega_s a_s^\dagger - \frac{ig}{2} a_i e^{i\omega_p t} \tag{7.9}$$

$$\dot{a_i} = -i\omega_i a_i - \frac{ig}{2} a_s^\dagger e^{-i\omega_p t} \tag{7.10}$$

Solutions to these equations are given by,

$$a_s^\dagger(t) = \left[a_s^\dagger(0)\cosh\left(\frac{gt}{2}\right) + i a_i(0)\sinh\left(\frac{gt}{2}\right)\right] e^{i\omega_s t} \tag{7.11}$$

$$a_i(t) = \left[a_i^(0)\cosh\left(\frac{gt}{2}\right) - i a_s^\dagger(0)\sinh\left(\frac{gt}{2}\right)\right] e^{-i\omega_i t} \tag{7.12}$$

In the teleportation experiment we are most interested in the number of quantum in the field so we look at terms that look like the photon number operator $n(t) = aa^\dagger$. Since we are in the Heisenberg picture if we calculate the expectation value of $n(t)$, the wavefunctions are the initial amount of quanta in the field at time $t = 0$ (just as the pump irradiates the medium), $|n_{s0}\rangle$ and $|n_{i0}\rangle$. We find an expression for the number of photons in the field,

$$\langle n_s(t)\rangle = n_{s0}\cosh^2\left(\frac{gt}{2}\right) + (1 + n_{i0}\sinh^2\left(\frac{gt}{2}\right) \tag{7.13}$$

$$\langle n_i(t)\rangle = n_{i0}\cosh^2\left(\frac{gt}{2}\right) + (1 + n_{s0}\sinh^2\left(\frac{gt}{2}\right) \tag{7.14}$$

The important part of these equations is noting that at time when there are no initial photons of ω_s and ω_i ($n_{s0} = n_{i0} = 0$) the pump induces single photon production due to the $1 + n_0$ term. In this way if the input pump radiation is the only applied field present then the non-linear medium emits spontaneous radiation at ω_s and ω_i. This is

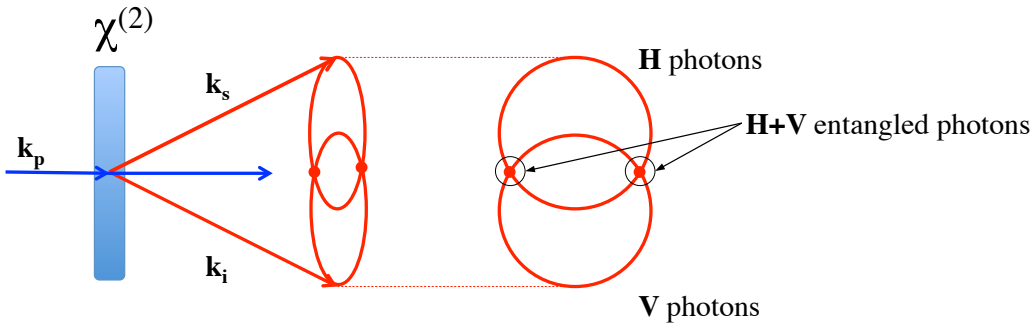

Figure 7.1: SDPC pair creation. Here the H photons and the V photons emerge from the crystal in different cones and where those cones overlap we cannot tell if the photon is a H or V photon until the polarization state is measured which tells us what the state of the other photon is.

the single photon production we are looking for and will exploit for the teleportation experiment.

7.3 Entangled Photon Pairs from SPDC

The non-linear crystals used in this work and others involving SPDC are bi-refringent, meaning that different polarizations propagate differently in the crystal and for pair creation the signal and idler have different polarizations (this is known as the type II phase matching condition). The most obvious way to see this is by observing the light cones created by the fast and slow axes of the crystal. A cartoon of this phenomenon can be seen in figure 7.3. The two cones come out as H and V polarized radiation and by looking at the figure we can clearly see that if we select out the overlapping parts then two polarization entangled photons are present [48]. The combined entangled state of the photons is,

$$|\Phi\rangle_{12} = \frac{|H\rangle_1|V\rangle_2 + |V\rangle_1|H\rangle_2}{\sqrt{2}} \tag{7.15}$$

Where the fact that we cannot tell what the polarization state of the photon is until a polarization measurement gives rise to the entanglement. For example, if we placed

polarization sensitive detector set to pass H in one of the overlapped beams then when an event is registered we instantly know the polarization state of the photon in the other overlapped beam.

A number of LOQC protocols can be carried out using the polarization entangled nature of these photon pairs [46, 67]. Additionally, one of the seminal works of quantum teleportation was accomplished using SPDC pairs [13]. Since the goal of this work is to achieve teleportation between a SPDC photon and a QD spin we will discuss the work in [13]. This protocol involves two SPDC sources: one acting as a source of single photons to be teleported, the other as an entangled pair to be teleported on. Here we will use the notation from the paper. We can write an initial state we wish to teleport,

$$|\psi\rangle_1 = \alpha|\leftrightarrow\rangle_1 + \beta|\updownarrow\rangle_1 \tag{7.16}$$

from one of the SPDC sources. The photons from the other SPDC source will be polarization entangled in the following way,

$$|\psi\rangle_{23} = \frac{1}{\sqrt{2}}\left[|\leftrightarrow\rangle_2|\updownarrow\rangle_3 - |\updownarrow\rangle_2|\leftrightarrow\rangle_3\right] \tag{7.17}$$

Here $|\leftrightarrow\rangle$ and $|\updownarrow\rangle$ represent the polarization state of the photon. If $|\psi\rangle_1$ and $|\psi\rangle_2$ are interfered on a beam splitter then coincidence clicks projects the photons to the anti-symmetric entangled state,

$$|\psi^-\rangle_{12} = \frac{1}{\sqrt{2}}\left[|\leftrightarrow\rangle_1|\updownarrow\rangle_2 - |\updownarrow\rangle_1|\leftrightarrow\rangle_2\right] \tag{7.18}$$

The anti-symmetric projection was discussed in 8.3. Once photon 1 and 2 are projected to this state then photon 3 is projected to the initial state placed on 1. This occurs because once coincidence occurs we are projected to $|\psi^-\rangle_{12}$ so regardless of the initial state of 1, 2 is now the opposite of that. And since 2 and 3 were initially

entangled to begin with 2 and 3 are orthogonal and thus the state of 3 becomes the state of 1,

$$|\psi\rangle_3 = \alpha|\leftrightarrow\rangle_3 + \beta|\updownarrow\rangle_3 \tag{7.19}$$

The essence of this teleportation is how we describe the teleportation of matter qubits via intermediate photon interference, so the discussion here is an instructive background for our own experiment.

7.4 High-brightness SPDC source

In all of the previously mentioned SPDC experiments the count rates are quite low compared to what we need to do our experiment, and the field of LOQC is growing to more complicated designs and measurements involving 6 and 8 fold coincidence measurements. So it is easy to see why increasing the count rates (called brightness in the literature, but when discussing single photons this is not the best language. Nevertheless we will use it here since it is the standard of the field) of single photon pair creation would be ideal. These high brightness SPDC sources are created by placing a strong cavity around the down conversion crystal to enhance emission in a narrow band (depending on the cavity linewidth).

The birefringent type phase matching condition that is described above makes integration into a cavity and in fact any optical system more challenging. Additionally the type II phase matching condition only occurs for the case where the cones overlap so a majority of the photon pair events are thrown out. To alleviate this problem we move to a periodically poled nonlinear crystal, specifically periodically poled potassium titanyl phosphate ($KTiOPO_4$) or PPKTP. This poling gives rise to a new quasi-phase matching condition ,

$$\mathbf{k}_p = \mathbf{k}_s + \mathbf{k}_i + \frac{2\pi}{\Lambda} \tag{7.20}$$

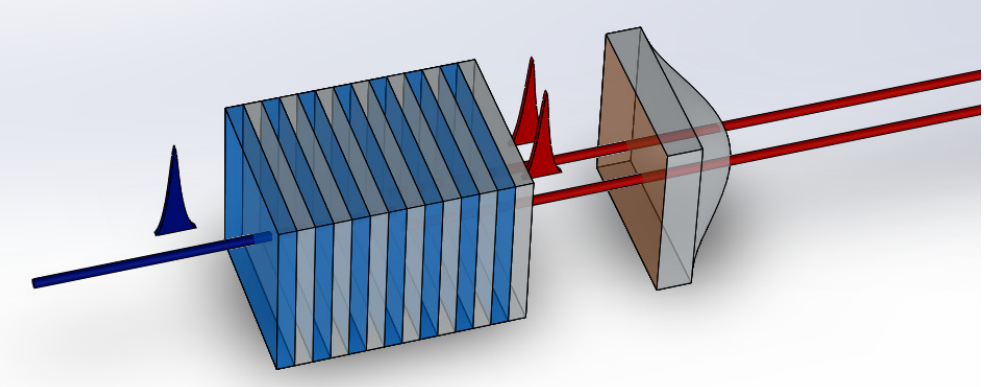

Figure 7.2: A PPKTP crystal with a cavity formed around it by HR coatings to enhance specific SPDC frequencies. The rounded crystal is a normal KTP crystal used to create a double-resonant cavity and enhance the quasi-phase matching condition. Since the PPKTP crystal is still birefringent the rounded KTP compensates for this so the H and V polarized photons exit the cavity at the same time.

where Λ is the pole spacing [32]. This more relaxed phase matching condition allows us to achieve type II phase matching for almost any $\mathbf{k}$ vector. So, collinear type II phase matched SPDC pairs are now achievable. Figure 7.4 is an example of a PPKTP crystal for creating collinear entangled photon pairs. The extra rounded crystal in the figure helps to form the cavity that will enhance the brightness of these entangled pairs and assists in achieving the quasi-phase matching condition [90].

For this experiment we will use a 5mm PPKTP crystal with a high reflective (HR) coating of 99% at 942nm on one side. A KTP (2.5mm length) crystal with a rounded end and reflective coating of 90% at 942nm is placed on the other side forming a double-resonant cavity with an overall cavity length of 15mm. In previous cavity-enhanced SPDC experiments the goal was to show coupling to atomic transitions so the cavity linewidths were 7MHz [3, 93]. However, since the bandwidth given by the QD trion lifetime is closer to 200MHz, this is the regime we will target for the SPDC cavity. Matching of the SPDC bandwidth to the QD bandwidth ensures larger coincidence counts in the HOM during interference. The cavity is placed in a temperature stabilized housing where temperature tuning will enable us to adjust

the center frequency of the SPDC cavity to match the center frequency of the QD. Since QDs are inhomogeneously broadened the ability to tune the SPDC cavity to match various QD transitions is important. However, the tuning range of the cavity is somewhat diminished due to limitations in temperature tuning. We are generally only able to achieve a tuning range of 2nm so we must find a QD around 942nm and the temperature tuning can be adjusted to align exactly with the QD transition. The distributions of our QD resonances are centered around 945nm so finding a QD at 942nm is not that challenging. We typically see 10-20 QDs in $1\mu m^2$ and have a field of view of $15\mu m^2$, so finding a dot in the desired range is not a major concern.

A 40ps pulse width mode-locked TiSaph laser is sent through a PPKTP crystal (not the cavity SPDC crystal) for second harmonic generation (SHG) the 461nm beam is then sent through the cavity SPDC set-up where polarization entangled photon pairs are created at 942nm with a 200MHz bandwidth. The cavity is locked to a reference laser using a Pound-Drever-Hall (PDH) locking method [11]. A mechanical chopper that blocks the locking beam when photon pairs are present so as not to flood the single photon detectors with the locking beam locks the cavity intermittently. In principle the cavity lengths for H and V polarized light are different but the addition of the concave surface to the "output coupler" KTP crystal adjusts the pathlengths in such a way that the pairs emerge from the cavity simultaneously and collinearly [90]. In order to avoid a higher photon number than 2 we operate below (700mW) the optical parametric oscillation (OPO) limit for this cavity (2.8W) [52, 41]. An optical diagram of this entire process is provided in figure 7.4 With these high brightness sources we are able to achieve the proper statistics within a reasonable integration time to show teleportation between SPDC photonic states and a QD spin state.

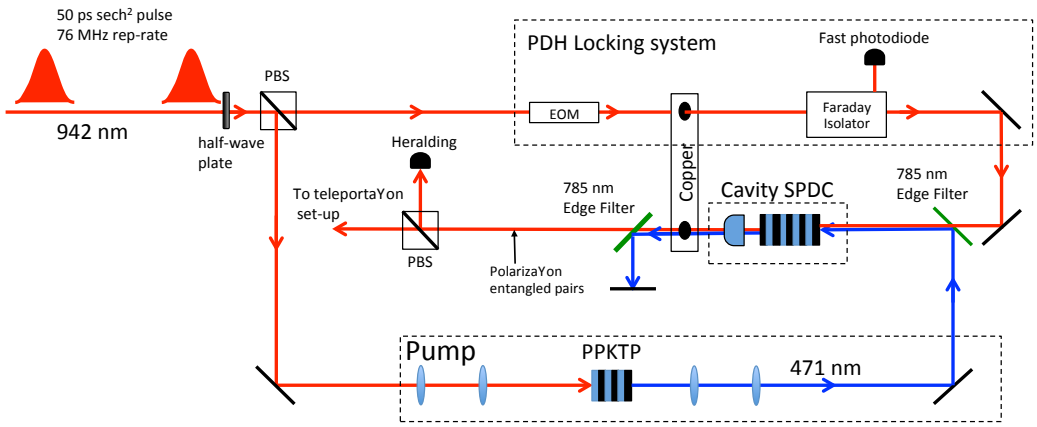

Figure 7.3: The cavity enhanced SPDC optical diagram. The 50 ps pulses are generated using a Tsunami laser and are fed into the SPDC set-up where the beams are split with one going to the Pound-Drever-Hall (PDH) locking set-up and the other to generate SPDC. The SPDC beam is doubled using a ppKTP crystal to 471nm and then sent through the cavity enhanced SPDC crystals to generate the down converted photons. The Chopper from the PDH set-up only locks the cavity when the laser is on so the detectors are not flooded with unwanted laser light. The residual 471 nm light is filtered using an edge filter and only the 942nm light of interest is sent to the teleportation set-up after the polarization beam splitter (PBS) picks one of the polarizations for heralding.

7.5 Conclusion

The cavity enhanced SPDC source discussed here is what will be used to carry out the teleportation experiment discussed in the next chapter. Some fundamentals of SPDC were discussed in this chapter to provide context and theoretical background for the coming experiments. We must understand the aspects of our apparatus in order to predict issues and analyze our results. The extension beyond teleportation requires a more in-depth understanding of SPDC than simply thinking of it as a push button source of photon pairs. So understanding how the process arises and the progression of the technique is important for this whole body of work.

CHAPTER VIII

Teleportation between a SPDC photon and a QD spin state

8.1 Introduction

Quantum teleportation has been studied for some time in systems that generate entangled photon pairs [13, 14, 6, 18, 82]. More recently the scheme of teleportation using a beam splitter and HOM interference is investigated to mediate entanglement swapping between two matter qubits (NV spins and trapped ions)[59, 8]. Until very recently, July 2015, this result had never been verified in QD spins [26]. The ability to transmit quantum information to different quantum memories or nodes will be crucial when scaling up any quantum technology. The resistance to decoherence exhibited by photons make them the best candidate to transmit this information. The fact that emitted photons can have their degrees of freedom entangled with the degrees of freedom of a qubit means that quantum information encoded on the qubit can be teleported onto another qubit via interference of the entangled photon states. We have already verified that this spin-photon entanglement is present in our QD system and this chapter will describe how we can extend this entanglement to do a more interesting experiment involving teleportation.

Since entangled photon pairs started and continue to lead the field of quantum

teleportation, it is not only straight forward but ideal to use this system to teleport information on a QD spin. This has the added benefit that both these systems are useful in many quantum information protocols and creating a hybrid quantum information architecture is useful for the maturation of the field of quantum technologies. The previous chapter discussed the theory for SPDC entangled pairs and how the down-conversion crystal can be placed in a temperature tuned cavity to enhance brightness and create pairs having a narrow bandwidth. We will use the high-brightness single photon packets to code information on the photons for teleportation on the spin state.

8.2 Theory of Teleportation

The implementation of this teleportation protocol relies heavily on the fact that two photonic qubits incident on a beam splitter will result in coincident clicks at the exit port in the case of an anti-symmetric Bell state. This result is discussed in section 8.3. The fact that an anti-symmetric projection occurs constrains the input states and can herald a teleportation of information. The interference relies on the fact that two photons in identical modes when incident on a beam splitter will always emerge along the same path, as discussed in section 6.4. So, two detectors placed in either output arm of a beam splitter would see a drop in coincidence counts as the two input photons become completely overlapped. By extension two non-identical photons, say of different frequency, could emerge in different arms resulting in coincident clicks on the detectors. This can be taken further by considering two input photonic states that are each a superposition of two different photon modes, in our case frequency, with one of the photon states being entangled with some matter qubit, which we will take to be our QD spin.

Recall from the entanglement section the polarization component is filtered out (section 5.5) leaving the photon in a superposition of the two transition frequencies (we will call $|R\rangle$ and $|B\rangle$ for red and blue). In the entanglement measurement a fast

detection scheme is employed to remove this frequency or which-path information [71]. However, in the case of teleportation this "color" qubit will act as the mediator of the entanglement and we will be interfering photonic qubits with different colors instead of different polarizations, but the resulting interaction can be calculated in the same way [59].

Let us consider the spin-photon entangled state from the QD to be,

$$|\Psi\rangle_{1qd} = \frac{|R\rangle_1|x+\rangle_{qd} + |B\rangle_1|x-\rangle_{qd}}{\sqrt{2}} \tag{8.1}$$

Here the subscripts denote the photonic part and the QD part. This is important for bookkeeping when we include a qubit from another photonic state. The photonic state from the SPDC source is split into two frequencies by an electo-optic phase modulator (EOPM) and the amount of each frequency can be controlled experimentally. The SPDC photon wavepacket is given by,

$$|\phi\rangle_2 = \frac{C_r|R\rangle_2 + C_b|B\rangle}{\sqrt{2}}. \tag{8.2}$$

The coefficients, C_r and C_b, are experimentally controllable by adjusting the amount of each frequency component present in the EOPM. Upon coincident detection in the HOM we know that the photons emerged from different paths and were therefore in different modes. However, there is no way to determine which input photonic qubit emerged on a given side, this leads to a projection of the photons to an intermediate anti-symmetric entangled state $|\Psi^-\rangle_{12}$.

$$|\Psi^-\rangle_{12} = \frac{|R\rangle_1|B\rangle_2 - |B\rangle_1|R\rangle_2}{\sqrt{2}} \tag{8.3}$$

Where the photonic states are now orthogonal to each other requiring the initial state

of photon 2 be instantly teleported onto $|\psi\rangle_{qd}$ giving [6],

$$|\psi\rangle_{qd} = \frac{C_b|x+\rangle - C_r|x-\rangle}{\sqrt{2}} \tag{8.4}$$

By adjusting the coefficients and reading out the spin state we are able to show that the spin state populations follow the experimentally controllable photonic qubit from the SPDC source.

This section describes the teleportation theory but there are several experimental constraints to consider and also the phase of the signal has not been discussed at all. The phase factor was important to keep track of for the entanglement experiment and we will discuss how to keep track of it in this experiment next.

8.3 Calculation of the Relevant Phases and Timing Considerations

One important advantage to using the HOM for mediating teleportation or entanglement swapping is that the timing resolution need not be sub-nanosecond like in the entanglement verification. The following calculations will show that this is the case and will look at the form of our signal for the teleportation protocol.

If we start with the QD spin-photon entangled state after the polarization component is filtered out, we have,

$$|\psi\rangle_{qd} = \frac{|R\rangle|x+\rangle - i|B\rangle|x-\rangle}{2} \tag{8.5}$$

And as we saw before this will oscillate at the photon frequencies between when the photon is detected and when it is rotated. This time between detection and rotation is what required the constraint in the timing resolution in the entanglement experiment.

so the state evolves like,

$$|\psi\rangle_{qd} = \frac{e^{i\omega_R(t_d-t)}|R\rangle|x+\rangle - ie^{i\omega_R(t_d-t)}|B\rangle|x-\rangle}{2} \tag{8.6}$$

Where t_d is the detection time and t will become the rotation time when we apply the $\pi/2$ pulse, which will act to rotate the coherence into a population. It is important to note that the rotation time is fixed by the experiment since the rotation pulse repetition rate is what sets the master clock for the experiment. Now the frequency qubit generated in the EOPM after the SPDC source will evolve as well until it is detected.

$$|\phi\rangle_{spdc} = \frac{C_r e^{i\omega_R(T_c-t_d)}|R\rangle_2 + C_b e^{i\omega_B(T_c-t_d)}|B\rangle}{\sqrt{2}} \tag{8.7}$$

Where here T_c is the creation time and t_d is the detection time. Important to note is that the detection time, t_d, is the same for both of these packets since they are incident on a HOM and we are looking for coincident clicks. By combining the result from Eqn. 8.3 the state teleported onto the spin state is,

$$|\psi\rangle_{qd} = \frac{C_b e^{i\omega_B(T_c-t_d)}e^{i\omega_R(t_d-t_r)}|x+\rangle - C_r e^{i\omega_R(T_c-t_d)}e^{i\omega_R(t_d-t)}|x-\rangle}{4} \tag{8.8}$$

Factoring out a global phase and canceling out the t_d we are left with,

$$|\psi\rangle_{qd} = \frac{c_b e^{-i\Delta(t-T_c)}|x+\rangle - C_r|x-\rangle}{4} \tag{8.9}$$

Now applying the rotation pulse R, which will set t now to t_r and projecting to the $|x+\rangle$ by looking at the initialization pulse from the next shot of the experiment as the readout of the spin state as we did in the entanglement experiment. The Δ describes the frequency difference of the photon states and corresponds to the spin difference frequency.

$$\langle x+|R|\psi\rangle_{qd} = \frac{C_b e^{-i\Delta(t_r-T_c)} + iC_r}{4} \tag{8.10}$$

if we take the case where $C_r = 1$ and we put an oscillation on C_b, like $e^{i\phi}$ then when we look at the signal we are left with,

$$|\langle x + |R|\psi\rangle_{qd}|^2 = \frac{1 - \sin\left[\Delta(t_r - T_c) + \phi\right]}{16} \tag{8.11}$$

Here we have laid out the considerations of the phase and shown that the detection time cancels out so the need for fast timing is not required due to the nature of the HOM interference. Additionally, we can see that as the coefficient C_b is adjusted we will see an oscillation in the signal in Eqn. 8.11. So that by counting the coincidences in a single shot we are able to see the counts rise and fall as we adjust C_b. The next sections will discuss the experimental implementation of the experiment, but before we can discuss the entire experimental apparatus we need to introduce the phase modulator that will be used to generate the two frequencies from the SPDC beam to match the QD spin-photon entangled frequencies.

8.3.1 Electro-optic Phase Modulator

The way we generate the two frequencies is by using an electro-optic phase modulator (EOPM). This device consists of a crystal waveguide in our case we use lithium niobate ($LiNbO_3$) modulators provided by EOSpace Inc. Lithium niobate is attractive for use in these devices since its refractive index is subject to change by the application of an electric field through the crystal. Also, the response of the material is quite high so modulations in the crystal on the time scale of 100 picoseconds is possible (note we use EOMs previously to achieve pulse widths of 250ps, so clearly the response in lithium niobate is capable of reaching high speeds). Unlike the regular EOMs which are amplitude modulators, these EOPMs only modulate the phase of the input radiation using a radio frequency (RF) input. The RF signal electrically drives the crystal changing the refractive index of the material and switching the phase of

any field in the crystal. A field in the crystal under no RF input will have the form $Ae^{i\omega t}$, now if we input a RF signal into the crystal with a frequency ν we get,

$$Ae^{i(\omega t + B\sin(\nu t))}. \tag{8.12}$$

We can expand this expression out to all orders and attain the following expression,

$$Ae^{i(\omega t + B\sin(\nu t))} = Ae^{i\omega t}\left(J_0(B) + \sum_{n=1} J_n(B)e^{in\nu t} + \sum_{n=1}(-1)^n J_n(B)e^{-in\nu t}\right). \tag{8.13}$$

Where $J_n(B)$ are Bessel functions derived from a useful expression [24],

$$e^{iB\sin\theta} = \sum_{n=-\infty}^{\infty} J_n(B)e^{in\theta}. \tag{8.14}$$

The RF input creates sidebands at integer multiples of the RF drive frequency of decreasing amplitude. By driving the EOPM at a frequency set to match the spin difference frequency, Δ, and setting the SPDC source to match one of the QD transitions, the side band generated will match the other QD transition frequency. Now the frequency components in each photonic qubit are matched.

It is one thing to generate sidebands from a laser field but a scattered single photon is fundamentally different[47]. To determine that we can get multiple frequencies we send the Rayleigh scattered single photons from the QD through the EOPM and frequency resolve the output. A schematic for this experiment is shown in figure 8.3.1. The CW laser is set resonant to the QD transition with collection in the reflection geometry as in chapter VI. The excitation laser is blocked using polarization and the single photons are sent into the EOPM where they are then sent through a pressure tuned etalon with a 400MHz linewidth and a free spectral range of 40GHz. By adjusting the pressure in the etalon cavity housing, using a computer controlled gas valve, we are able to scan through the etalon's entire free spectral range to determine

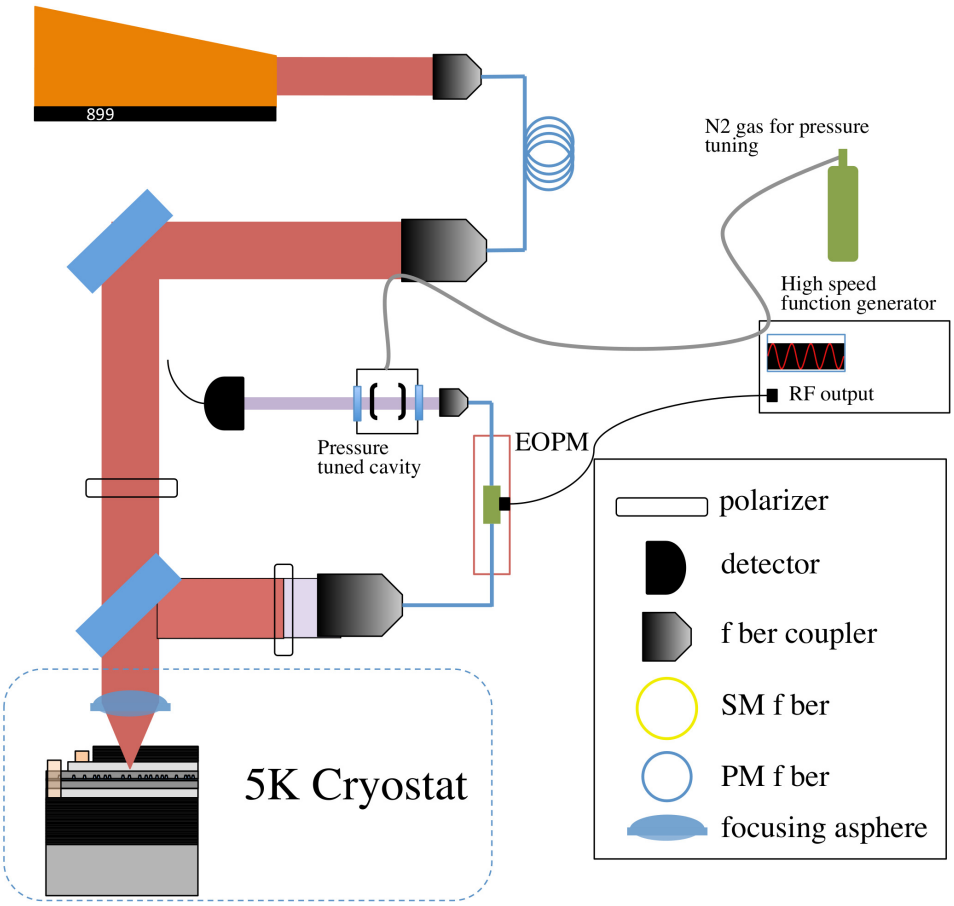

S

Figure 8.1: Set-up to determine if single photons scattered off the QD transitions will be split into multiple frequencies after sent through an EOPM with and RF drive. The frequencies are resolved using a pressure tuned cavity with a line width of 400MHz. The linewidth does not allow for high resolution scans, but if the RF drive is set to many GHz we should easily be able to resolve it.

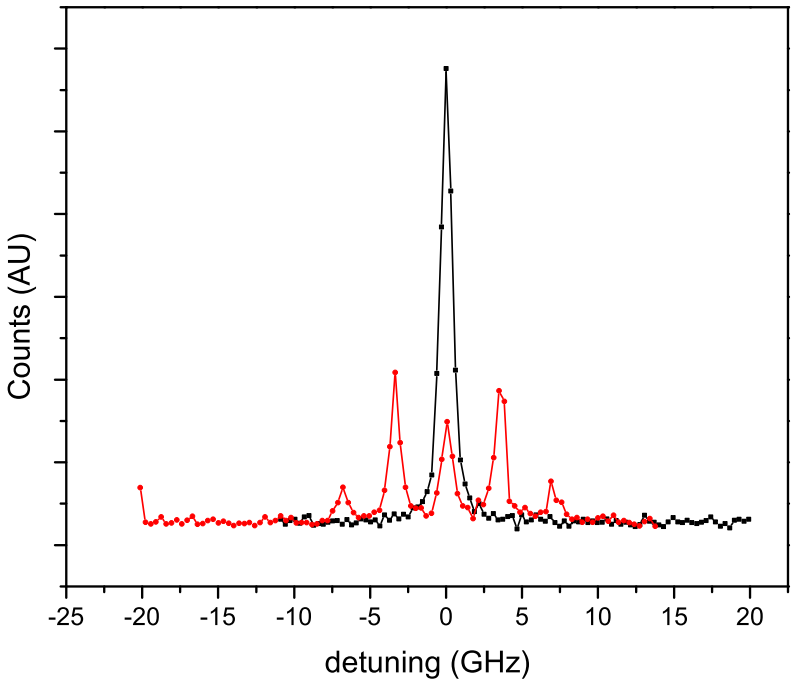

Figure 8.2: The data shows a frequency resolved scan when sent through the EOPM with the RF drive off (black) and on (red). The frequency is set using a Hewlett-Packard function generator (HP8672a) with the drive set to 3.2GHz

frequency separations. The CW linewidth of the QD trion transition we are interested in is 1.7GHz so the etalon linewidth should not limit this measurement. Of course the resulting spectrum will be a convolution of the linewidth of the etalon and the QD linewidth but we are mostly interested in frequency resolving peaks separated by 5-8GHz (the range of the spin splitting for the teleportation measurement), so resolving this will not be a problem for this optical system. Figure 8.3.1 shows scanned etalon data with the RF output applied to the EOPM and with no signal applied to the EOPM. We can clearly see from this data that the scattered photons are split into different frequencies corresponding to the RF drive frequency. When selecting the frequencies we use an air-spaced etalon to filter our the unwanted frequencies, leaving only the two frequencies that will be interfered with the QD photonic qubit. The air

spaced etalon we are using is manufactured specially by Tec Optics with a free spectral range of 652GHz and a finesse of 120. The etalon is chosen with these parameters to give a linewidth of 5.2GHz so we can generate sidebands 7.5GHz (the typical spin difference frequency) apart and only pass two components.

8.3.2 Qubit Interference Generated by EOPM

Finally, before we move into the experimental implementation of the teleportation we must determine that the state generated from the phase modulator is a frequency qubit. To do this we take the output of the phase modulator with a 5GHz RF frequency applied to the EOPM and use the etalon mentioned in the previous section to only allow 2 frequencies to pass. We can repeat the experiment from section 6.4.3, by sending the single photon pulse through The EOPM before we split the arms and delay one for interference (figure 6.12). The frequency qubit should be identical to the delayed qubit and we expect to see a clear drop in coincidences at time zero corresponding to indistinguishability. Figure 8.3 shows that the degree of indistinguishability present for the frequency qubit is nearly identical to that of just a single photon with the RF drive on the EOPM switched off [37]. The polarization of the input HOM arms are set parallel to each other and if they were perpendicular we would see the normalized coincidences rise to 0.5 as in figure 6.13.

So from this experiment we can see that the frequency qubit generated from the EOPM has a high degree of indistinguishability, which is important for the teleportation protocol.

8.4 Experimental Implementation

A timing diagram for the experiment can be seen in figure 8.4. Similarly to the entanglement experiment the top diagram describes the process for generating the spin-photon entangled state that interferes with the SPDC photonic qubit rep-

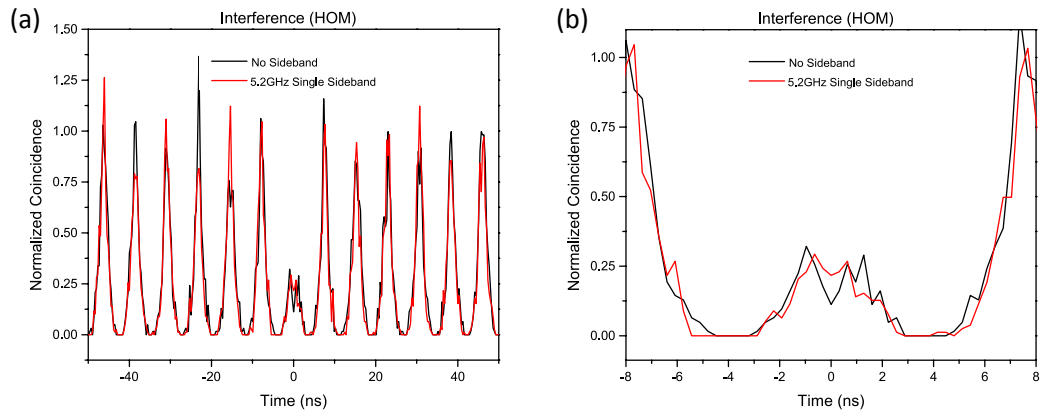

Figure 8.3: Interference data from a

resented in the bottom diagram. The teleportation experiment is set-up similar to the entanglement experiment. The 4ns initialization/readout pulse optically pumps the spin population to $|x-\rangle$ and the 250ps π-pulse selectively excites the population to $|T_x-\rangle$. Decay from $|T_x-\rangle$ generates the spin-photon entangled state and after the polarization is projected away we are left with Eqn. 8.1. The photon from the QD is interfered on a beam splitter with the photonic qubit from the SPDC source. The event from the SPDC source is generated using a pulsed Ti:Saph laser (Spectra Physics Tsunami) with a pulse width of 40ps and locked to the repetition rate of the MIRA (the 2ps rotation laser) so there is a single master clock for the experiment. Since the MIRA is passively mode-locked, we use the sync signal generated from the a fast photodiode in the MIRA cavity to lock the clocks of all the timing electronics (the Tsunami laser, the HydraHarp TDC, the detectors, and the EOMs). The SPDC generates polarization entangled states so a polarizing beam cube is used to separate the co-linear radiation. One polarization is used to herald (idler) the presence of a single photon pulse in the other polarization (signal), since single photon pulse operation only occurs during a heralded process for SPDC. The signal beam is sent through the EOPM generating the second frequency required to match the QD photonic qubit. The relative strengths of the frequencies is controlled by adjusting the

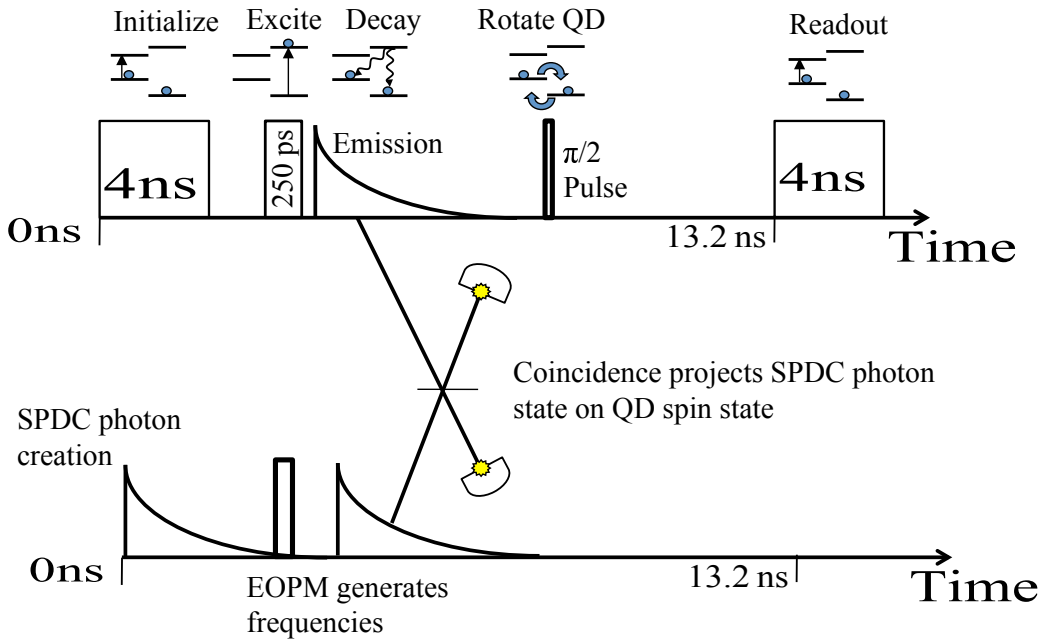

Figure 8.4: The timing diagram for the teleportation protocol. The single photon packets from the QD and the SPDC source are interfered on a beam splitter and coincident clicks heralds successful teleportation. The rotation and readout are performed identically to the entanglement experiment.

drive amplitude which effects the teleported coefficients discussed in section 8.2. If a coincidence is registered in the HOM then this will herald a successful teleportation and the 4ns initialization pulse from the next shot of the experiment will act as the $|x+\rangle$ spin state readout yielding the signal in Eqn. 8.11. A schematic of the optical set-up can be found in figure 8.5.

This is a four-fold coincidence measurement, so understanding the detection rate is vital. To begin the QD collection efficiency, using a 20% detection efficiency detector, in the old Schottky diode sample is $\eta_{qd} \approx 10^{-5}$. Since we have moved to a new sample structure with higher light collection and upgraded our detector system to superconducting nano-wire detectors (SCNWD) this efficiency has increased by a factor of 500 leaving us with $\eta_{qd} \approx 5 \times 10^{-3}$. The SPDC estimates for previously achievable coincidence rates in similar cavity enhanced systems gives a rate of $\approx 3 \times 10^4 s^{-1}$ when using a 20% efficiency detector. This leads to an overall collection efficiency of $\eta_{spdc} \approx 4 \times 10^{-2}$ for each photon generated in SPDC. Since the signal beam from the SPDC will go through the EOPM, there is an extra loss of 70% in that arm due to the efficiency and the insertion loss of the EOPM. Combining this with the factors of 2 for the beam splitters and the fact that coincidence should only occur 1/4 of the time due to the 4 Bell states that are possible we get a final expression for 4 fold coincidence of,

$$P_{\text{4fold}} = \frac{\eta_{qd}\eta_{qd}(0.30)\eta_{spdc}\eta_{spdc}}{16} \times (76 \times 10^6 MHz) = 0.57 s^{-1} \tag{8.15}$$

This shows that we should get 3.4 four-fold coincidences each minute. So to achieve a proper signal to noise we want to get between 100 and 300 coincidences at the maximum point of our derived signal from Eqn. 8.11. In the spin photon entanglement experiment we were able to keep all the lasers and QD locked using servo-loops for over 30 hours of integration time. For the teleportation experiment it is reasonable

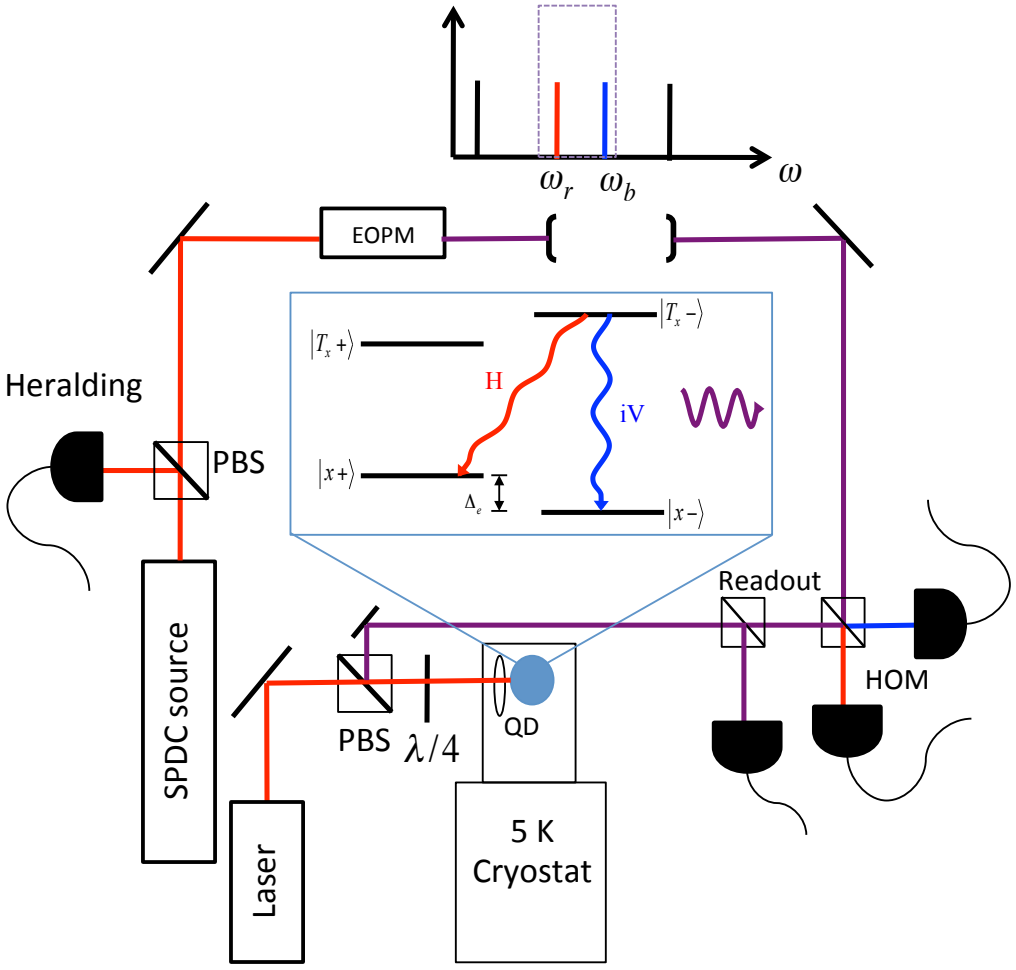

Figure 8.5: The optical schematic for the experimental implementation of the teleportation. The SPDC source is split into two frequencies, matched to the QD frequencies by the EOPM and an etalon selects out the proper sidebands for teleportation. Here "laser" encompasses all the excitation, rotation, and readout/initialization lasers. The SPDC source is the high brightness source discussed in chapter VII.

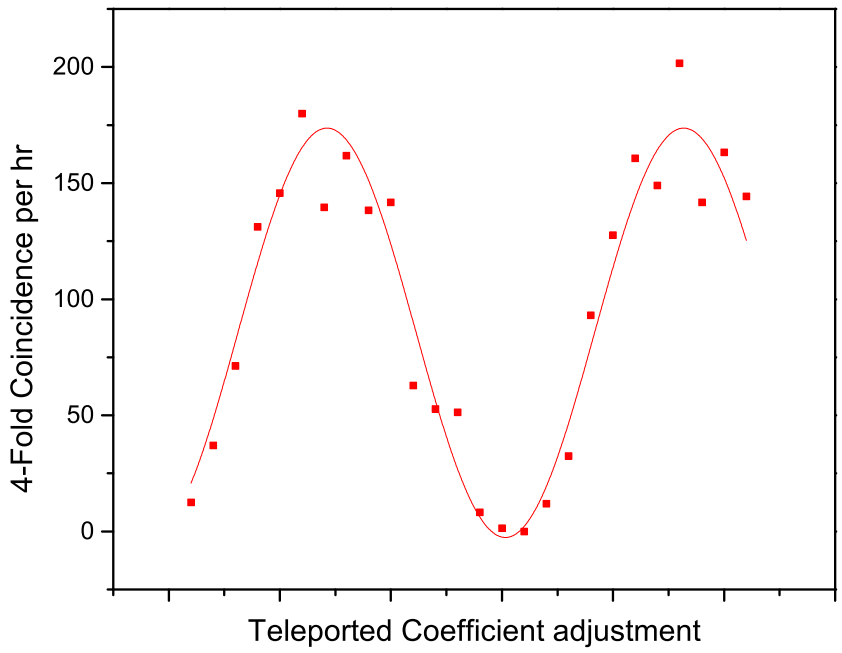

Figure 8.6: This is a Monte Carlo of what our signal might look like. Both the coincidence rate and oscillation frequency have been randomized based on a normal distribution centered around their theoretical values. Each point on the x-axis corresponds to an hour of integration time.

to expect we could take 25 data points of 1 hour integration time for each point and trace out the desired signal. A Monte Carlo (MC) simulation of what this signal could look like is shown in figure 8.6. Using the MC data we can see that a definitive signal should be possible for the 25 hour integration and we can extract a good sine fit showing the dependence of the spin state on the input SPDC photonic qubit state.

The MC simulation is conducted by assigning the maximum amplitude of the signal from Eqn. 8.11 as 200 (the number of 4-fold coincidences in an hour for maximum signal). To mimic counting errors and spurious coincidences a normal distribution, with a standard deviation given by the Poisson statistics associated with photon counting, is randomized and applied to the amplitude of each point. Additionally, random numbers are selected from a normal distribution with a width

associated with the timing of the electronics and applied to the $\Delta(t_r - T_c)$ term in the sine function. Note that these random numbers can be both negative and positive since the normal distributions are each centered around zero. If we assign each of these randomly addressed distributions an expression P_{25}(counting) and P_{25}(timing), where the 25 represents the number of times this distribution is applied (for 25 hour long integration runs at different values of ϕ). we are left with the signal,

$$Sig_{\mathrm{MC}} = (200 + P_{25}(\text{counting}))\,(1 - \sin\left[\Delta\left(P_{25}(\text{timing})\right)(t_r - T_c) + \phi\right]) \qquad (8.16)$$

This expression gives an idea of what the potential signal could look like and gives a more realistic version of the experiment than simply plotting Eqn. 8.11.

8.5 Conclusion

Here we have laid-out the procedure for teleportation of a controllable state onto a QD spin. The mathematical description of the teleportation was discussed and we determined that the detector timing resolution is not as strict as the previous entanglement experiment. We discussed the operation of a phase modulator and how it can be used to generate sidebands in a laser and scattered photons. We showed that scattered photons through a phase modulator with a RF drive through the crystal exhibit the same sidebands that a laser field would. These sidebands can be used to generate the frequency qubit required for teleportation. Implementation of this protocol will open new prospects for entanglement swapping and transportation of quantum information. The next and final chapter will discuss the new avenues available after demonstration of this teleportation.

CHAPTER IX

Conclusions and Future Directions

9.1 Concluding Remarks

In this work we have shown that QD transitions behave similar to atomic transitions and that the methods we used to study atomic transitions can be used in QDs as well. The motivation for QDs as a viable quantum computing architecture was discussed. We show that using time gated quasi-CW laser pulses from EOMs allow us to follow the excited state population in the time tagged scattering spectrum and that the transverse and longitudinal optical decay rates we extract from these time domain data are inconsistent with the numbers we arrive at from CW or frequency domain measurements. The suspected reason for this is a spectral wandering process which exists on time scales larger than the dephasing rate γ. This discovery is important since if we found dephasing mechanisms on a short time scale this could pose a crippling problem when trying to do gate operations before the system dephases.

We showed that a spontaneously emitted photon from a QD trion state is entangled with the ground state electron spin state. This result is crucial to verify if QDs were to have a future in quantum computing. The Fidelity of 0.6 is roughly 84% of the detector limited fidelity so we were mostly harmed by the detector timing resolution. We showed that this timing resolution though important when verifying the entanglement is not a stringent requirement for entanglement swapping protocols

or teleportation protocols that utilize a HOM interferometer to interfere two photon states. So the timing resolution that limited us is not a problem going forward.

We discussed the theory behind HOM interference and how it is altered in the case of entangled qubits. We took data showing interference between a QD scattered photon and the same QD's photon delayed by the repetition rate of the excitation laser. By adjusting the polarization at the input of the HOM we moved from the case of quantum interference when the photons are in identical modes to where the photons are distinguishable and we recover the classical behavior of the beam splitter. We also used an EOPM to create sidebands from the QD scattered photons and interfered those with each other and found the same indistinguishability. This is crucial to our experiment since we will be using the EOPM to create frequency qubits from the SPDC photons for teleportation onto the QD spin. The HOM indistinguishability of the photons from the EOPM coupled with the frequency resolved scans, using a pressure tuned etalon, of the scattered photons through the EOPM in the presence of an RF field to generate sidebands, provide compelling evidence for a frequency qubit generated by single photons through a EOPM.

The original reason to use the tunable etalon was for resolving the EOPM sidebands but it was also used to observe the Mollow triplet by frequency resolving the scattering from a trion transition at zero magnetic field. This feat had never been accomplished in our lab except by means of pump-probe spectroscopy. We showed how the Mollow triplet comes about and that the expected behavior of the sidebands under increasing excitation powers is observed experimentally. The ability to frequency resolve scattering and emission could aid data taking in a number of experiments.

We outlined the theory of SPDC and how we will use cavity enhancement to generate larger rates of single photon pairs. These single photons will then be used in the teleportation experiment that we laid out in the final chapter. Here we discussed the theory of teleportation and completed a calculation of the relevant phases for

the teleportation experiment. We found that the detection time (which needed to have high timing in our entanglement experiment) cancels in the HOM and the high timing requirement is loosened allowing us to use higher efficiency detectors. The phase calculation yielded the form of our final signal and a MC simulation shed light on what our potential signal would look like.

9.2 Future Directions

The next step in this work is to verify the outlined teleportation protocol upon completion of the cavity enhanced SPDC source (expected date August 2015). The first step is to simply show the ability to get good HOM interference between the SPDC photons and the QD photons. This first step requires no field or spin read-out/preparation, only the techniques already shown in 6.4.3. The feat of showing this interference is already something other groups have not done. The teleportation protocol, though requiring long (25 hour) integration times to verify, is straight forward now since the theory and considerations have been outlined here. The experimental difficulties are by no mean simple to handle since it requires the locking of 2 CW lasers and 2 Pulsed lasers with a magnetic field applied in the superconducting magnetic cryostat. However, with the expertise already gained when performing the entanglement experiment (2 CW lasers and 1 pulsed laser) it is certainly not a daunting task to accomplish.

As stated in the last section, the Mollow triplet data can hold a compelling interest. Using a higher resolution etalon could enable us to learn more about this spectrum and even utilize the sideband emission for additional quantum optics measurements. One that comes to mind is the extraction of γ and γ_2. We saw before that CW data for these quantities is in disagreement with time domain data but perhaps the inelastic scattering terms that form the sidebands could provide another piece to this puzzle. Unfortunately, the current experimental apparatus is not sensitive enough for

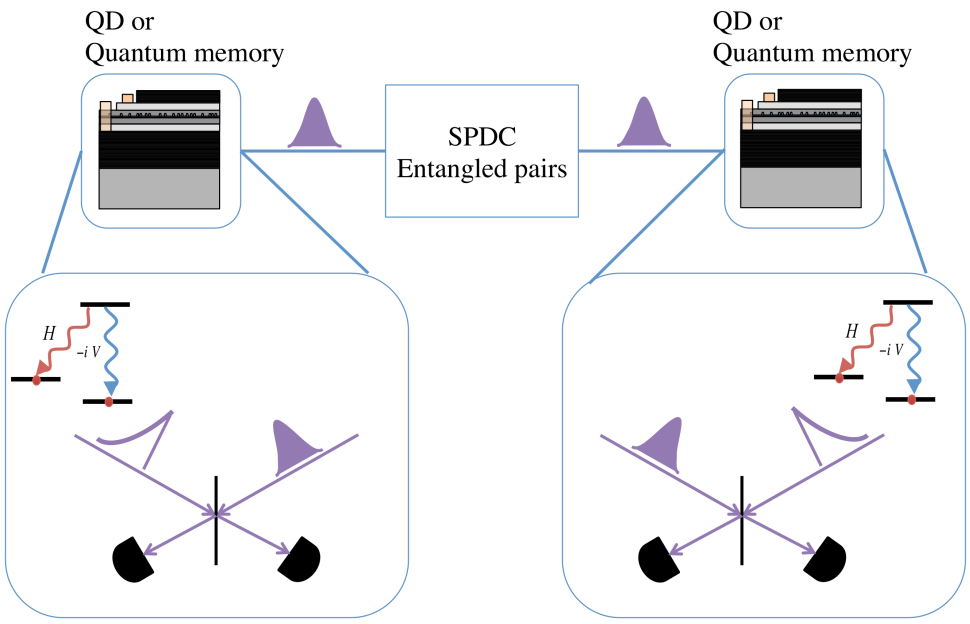

Figure 9.1: The SPDC source described here can couple with a QDs from distant locations or even QD memories in distant locations and act as an entanglement swapping intermediary. The entangled photo pairs from the SPDC source will interfere with the spin-photon entangled state from each QD and swap the entanglement between them causing the ground state spins to precess coherently

this measurement.

The teleportation protocol we discussed here can be extended into a number of different directions. The fact that SPDC creates entangled pairs is not exploited in the current version of the experiment but it is a powerful tool to transport quantum information. If we sent the second photon to another QD and performed the same teleportation type interference then the entangled nature of the SPDC photons could act as an intermediate entanglement swapping apparatus. The two distant QD spins would now be entangled. A diagram of such a method is shown in figure 9.2. By this method we are utilizing the spin-photon entangled state of the QD to entangle distant spins. The entanglement of distant spins, and even spins on the same ship is essential for performing quantum information protocols. This SPDC technology does not need to be limited only to QDs, The same entanglement swapping can be

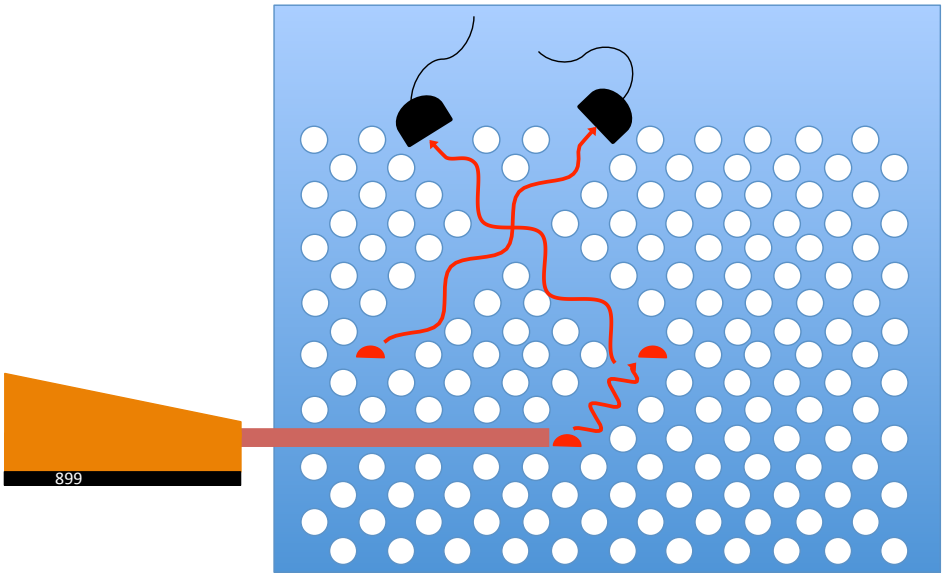

Figure 9.2: A cartoon of a possible integrated photonic circuit. The mounds are QDs embedded in the photonic crystal cavity. radiation from QDs can be guided through the pathways to different QDs. On board detectors can act as readouts.

achieved in any quantum information system. In fact, by tailoring the pump pulse and adjusting the cavity we may be able to use the SPDC to entangle distant spins of different platforms (a QD spin entangled with an NV spin). Were this achieved then quantum memories based on different platforms could share information via this SPDC entanglement bridge.

In order for the QD technology to mature beyond its current state we must move to a more integrated design for the sample structures. Photonic crystal wave guides can be utilized to transport light around a structure and can be used as information pathway between distant QDs embedded in photonic crystal cavities. A cartoon of this is shown in figure 9.2. The photonic waveguides act as pathways to form an integrated circuit. With the emergence of nano-fabrication on-chip detectors to readout the optical pathways are possible and would allow for many of the same measurements conducted in free-space. One of the greatest challenges still facing the field of QDs is the problem of inhomogeneous broadening of the QD resonances.

The interference that enables entanglement swapping in a photonic crystal circuit, requires that the QDs at each node have the same energy. Some advancement has been made in this area but it is still an open field of research.

The study of quantum phenomena is one of the most important avenues in modern science. In the case of this work and other like it we are able to probe these fundamental questions of entanglement and coherence while still addressing the technological applications of such technologies. In the future the study of quantum technologies will become more geared towards engineering of quantum systems, but we must never lose sight of the intellectual curiosity displayed by the giants upon who's shoulder we stand. The continued journey to understand the world of quantum mechanics should always be in the back of our minds when conducting this research.

BIBLIOGRAPHY

BIBLIOGRAPHY

[1] Benito Alén, Florian Bickel, Khaled Karrai, Richard J. Warburton, and Pierre M. Petroff. Stark-shift modulation absorption spectroscopy of single quantum dots. *Applied Physics Letters*, 83(11):2235, 2003.

[2] Mete Atatüre, Jan Dreiser, Antonio Badolato, Alexander Högele, Khaled Karrai, and Atac Imamoglu. Quantum-dot spin-state preparation with near-unity fidelity. *Science*, 312(5773):551–553, 04 2006.

[3] Xiao-Hui Bao, Yong Qian, Jian Yang, Han Zhang, Zeng-Bing Chen, Tao Yang, and Jian-Wei Pan. Generation of narrow-band polarization-entangled photon pairs for atomic quantum memories. *Phys. Rev. Lett.*, 101:190501, Nov 2008.

[4] M. D. Barrett, J. Chiaverini, T. Schaetz, J. Britton, W. M. Itano, J. D. Jost, E. Knill, C. Langer, D. Leibfried, R. Ozeri, and D. J. Wineland. Deterministic quantum teleportation of atomic qubits. *Nature*, 429(6993):737–739, 06 2004.

[5] John S Bell et al. On the einstein-podolsky-rosen paradox. *Physics*, 1(3):195–200, 1964.

[6] Charles H. Bennett, Gilles Brassard, Claude Crépeau, Richard Jozsa, Asher Peres, and William K. Wootters. Teleporting an unknown quantum state via dual classical and einstein-podolsky-rosen channels. *Phys. Rev. Lett.*, 70:1895–1899, Mar 1993.

[7] Paul R Berman and Vladimir S Malinovsky. *Principles of laser spectroscopy and quantum optics*. Princeton University Press, 2010.

[8] H. Bernien. Heralded entanglement between solid-state qubits separated by three metres. *Nature*, 497:86–90, 2013.

[9] H. Bernien, B. Hensen, W. Pfaff, G. Koolstra, M. S. Blok, L. Robledo, T. H. Taminiau, M. Markham, D. J. Twitchen, L. Childress, and R. Hanson. Heralded entanglement between solid-state qubits separated by three metres. *Nature*, 497(7447):86–90, 05 2013.

[10] J. Beugnon, M. P. A. Jones, J. Dingjan, B. Darquié, G. Messin, A. Browaeys, and P. Grangier. Quantum interference between two single photons emitted by independently trapped atoms. *Nature*, 440(7085):779–782, 04 2006.

[11] Eric D Black. An introduction to pound–drever–hall laser frequency stabilization. *American Journal of Physics*, 69(1):79–87, 2001.

[12] B. B. Blinov, D. L. Moehring, L. M. Duan, and C. Monroe. Observation of entanglement between a single trapped atom and a single photon. *Nature*, 428(6979):153–157, 03 2004.

[13] D. Bouwmeester. Experimental quantum teleportation. *Nature*, 390:575–579, 1997.

[14] D. Bouwmeester, A. Ekert, and A. Zeilinger. The physics of quantum information. 2000.

[15] Robert Boyd. *Nonlinear optics*. Academic Press, Burlington, MA, 2008.

[16] R Hanbury Brown and RQ Twiss. Correlation between photons in two coherent beams of light. *Nature*, 177(4497):27–29, 1956.

[17] David C. Burnham and Donald L. Weinberg. Observation of simultaneity in parametric production of optical photon pairs. *Phys. Rev. Lett.*, 25:84–87, Jul 1970.

[18] Wesley B. Cardoso, A. T. Avelar, B. Baseia, and N. G. de Almeida. Teleportation of entangled states without bell-state measurement. *Phys. Rev. A*, 72:045802, Oct 2005.

[19] Pochung Chen, C. Piermarocchi, L. J. Sham, D. Gammon, and D. G. Steel. Theory of quantum optical control of a single spin in a quantum dot. *Phys. Rev. B*, 69:075320, Feb 2004.

[20] J. Chiaverini, J. Britton, D. Leibfried, E. Knill, M. D. Barrett, R. B. Blakestad, W. M. Itano, J. D. Jost, C. Langer, R. Ozeri, T. Schaetz, and D. J. Wineland. Implementation of the semiclassical quantum fourier transform in a scalable system. *Science*, 308(5724):997–1000, 05 2005.

[21] J. Chiaverini, D. Leibfried, T. Schaetz, M. D. Barrett, R. B. Blakestad, J. Britton, W. M. Itano, J. D. Jost, E. Knill, C. Langer, R. Ozeri, and D. J. Wineland. Realization of quantum error correction. *Nature*, 432(7017):602–605, 12 2004.

[22] Colin Chow. *Towards a Universal Two-Qubit Gate with Self-Assembled InAs Quantum Dot Molecules*. Doctoral Thesis, University of Michigan, 2015.

[23] J. I. Cirac, P. Zoller, H. J. Kimble, and H. Mabuchi. Quantum state transfer and entanglement distribution among distant nodes in a quantum network. *Phys. Rev. Lett.*, 78:3221–3224, Apr 1997.

[24] David Colton and Rainer Kress. *Inverse Acoustic and Electromagnetic Scattering Theory (Applied Mathematical Sciences)*. Springer, 3rd ed. 2013 edition, 10 2012.

[25] Kristiaan De Greve, Leo Yu, Peter L. McMahon, Jason S. Pelc, Chandra M. Natarajan, Na Young Kim, Eisuke Abe, Sebastian Maier, Christian Schneider, Martin Kamp, Sven Hofling, Robert H. Hadfield, Alfred Forchel, M. M. Fejer, and Yoshihisa Yamamoto. Quantum-dot spin-photon entanglement via frequency downconversion to telecom wavelength. *Nature*, 491(7424):421–425, 11 2012.

[26] A. Delteil, S. Zhe, W.-b. Gao, E. Togan, S. Faelt, and A. Imamoglu. Generation of heralded entanglement between distant hole spins. *ArXiv e-prints*, July 2015.

[27] D. P. DiVincenzo. Topics in Quantum Computers. *eprint arXiv:cond-mat/9612126*, December 1996.

[28] L. M. Duan, M. D. Lukin, J. I. Cirac, and P. Zoller. Long-distance quantum communication with atomic ensembles and linear optics. *Nature*, 414(6862):413–418, 11 2001.

[29] Sophia E. Economou, Ren-Bao Liu, L. J. Sham, and D. G. Steel. Unified theory of consequences of spontaneous emission in a λ system. *Phys. Rev. B*, 71:195327, May 2005.

[30] C Emary and L J Sham. Optically controlled single-qubit rotations in self-assembled inas quantum dots. *Journal of Physics: Condensed Matter*, 19(5):056203, 2007.

[31] H. Fearn and R. Loudon. Theory of two-photon interference. *J. Opt. Soc. Am. B*, 6:917 –927, 1989.

[32] Alessandro Fedrizzi, Thomas Herbst, Andreas Poppe, Thomas Jennewein, and Anton Zeilinger. A wavelength-tunable fiber-coupled source of narrowband entangled photons. *Opt. Express*, 15(23):15377–15386, Nov 2007.

[33] E. B. Flagg. Interference of single photons from two separate semiconductor quantum dots. *Phys. Rev. Lett.*, 104:137401, 2010.

[34] P. A. Franken, A. E. Hill, C. W. Peters, and G. Weinreich. Generation of optical harmonics. *Phys. Rev. Lett.*, 7:118–119, Aug 1961.

[35] A. Zeilinger G. Weihs. *Photon statistics at beam-splitters: an essential tool in quantum information and teleportation*, manual Chapter 1 - Introduction, page i. Wiley, 2001.

[36] W. B. Gao, P. Fallahi, E. Togan, A. Delteil, Y. S. Chin, J. Miguel-Sanchez, and A. Imamoğlu. Quantum teleportation from a propagating photon to a solid-state spin qubit. *Nat Commun*, 4, 11 2013.

[37] W. B. Gao, P. Fallahi, E. Togan, J. Miguel-Sanchez, and A. Imamoglu. Observation of entanglement between a quantum dot spin and a single photon. *Nature*, 491(7424):426–430, 11 2012.

[38] O. Gazzano. Bright solid-state sources of indistinguishable single photons. *Nat. Commun*, 4:1425, 2013.

[39] Oliver Gywat, Hubert J. Krenner, and Jesse Berezovsky. *Spins in Optically Active Quantum Dots: Concepts and Methods*. Wiley-VCH, 1 edition, 2 2010.

[40] H. Haffner, W. Hansel, C. F. Roos, J. Benhelm, D. Chek-al kar, M. Chwalla, T. Korber, U. D. Rapol, M. Riebe, P. O. Schmidt, C. Becher, O. Guhne, W. Dur, and R. Blatt. Scalable multiparticle entanglement of trapped ions. *Nature*, 438(7068):643–646, 12 2005.

[41] S. E. Harris, M. K. Oshman, and R. L. Byer. Observation of tunable optical parametric fluorescence. *Phys. Rev. Lett.*, 18:732–734, May 1967.

[42] Alexander Högele, Stefan Seidl, Martin Kroner, Khaled Karrai, Richard J. Warburton, Brian D. Gerardot, and Pierre M. Petroff. Voltage-controlled optics of a quantum dot. *Phys. Rev. Lett.*, 93:217401, Nov 2004.

[43] C. K. Hong, Z. Y. Ou, and L. Mandel. Measurement of subpicosecond time intervals between two photons by interference. *Phys. Rev. Lett.*, 59:2044–2046, Nov 1987.

[44] Danny Kim, Sophia E. Economou, Ştefan C. Bădescu, Michael Scheibner, Allan S. Bracker, Mark Bashkansky, Thomas L. Reinecke, and Daniel Gammon. Optical spin initialization and nondestructive measurement in a quantum dot molecule. *Phys. Rev. Lett.*, 101:236804, Dec 2008.

[45] Erik D. Kim, Katherine Truex, Xiaodong Xu, Bo Sun, D. G. Steel, A. S. Bracker, D. Gammon, and L. J. Sham. Fast spin rotations by optically controlled geometric phases in a charge-tunable inas quantum dot. *Phys. Rev. Lett.*, 104:167401, Apr 2010.

[46] E. Knill, R. Laflamme, and G. J. Milburn. A scheme for efficient quantum computation with linear optics. *Nature*, 409(6816):46–52, 01 2001.

[47] Pavel Kolchin, Chinmay Belthangady, Shengwang Du, G. Y. Yin, and S. E. Harris. Electro-optic modulation of single photons. *Phys. Rev. Lett.*, 101:103601, Sep 2008.

[48] Paul G. Kwiat, Klaus Mattle, Harald Weinfurter, Anton Zeilinger, Alexander V. Sergienko, and Yanhua Shih. New high-intensity source of polarization-entangled photon pairs. *Phys. Rev. Lett.*, 75:4337–4341, Dec 1995.

[49] Malcolm H. Levitt. *Spin Dynamics: Basics of Nuclear Magnetic Resonance*. Wiley, 2 edition, 4 2008.

[50] Xiaoqin Li, Yanwen Wu, Duncan Steel, D. Gammon, T. H. Stievater, D. S. Katzer, D. Park, C. Piermarocchi, and L. J. Sham. An all-optical quantum gate in a semiconductor quantum dot. *Science*, 301(5634):809–811, 08 2003.

[51] Daniel Loss and David P. DiVincenzo. Quantum computation with quantum dots. *Phys. Rev. A*, 57:120–126, Jan 1998.

[52] Y. J. Lu and Z. Y. Ou. Optical parametric oscillator far below threshold: Experiment versus theory. *Phys. Rev. A*, 62:033804, Aug 2000.

[53] Xiao-Song Ma, Thomas Herbst, Thomas Scheidl, Daqing Wang, Sebastian Kropatschek, William Naylor, Bernhard Wittmann, Alexandra Mech, Johannes Kofler, Elena Anisimova, Vadim Makarov, Thomas Jennewein, Rupert Ursin, and Anton Zeilinger. Quantum teleportation over 143 kilometres using active feed-forward. *Nature*, 489(7415):269–273, 09 2012.

[54] H. J. Mamin, M. Kim, M. H. Sherwood, C. T. Rettner, K. Ohno, D. D. Awschalom, and D. Rugar. Nanoscale nuclear magnetic resonance with a nitrogen-vacancy spin sensor. *Science*, 339(6119):557–560, 02 2013.

[55] Klaus Mattle, Harald Weinfurter, Paul G. Kwiat, and Anton Zeilinger. Dense coding in experimental quantum communication. *Phys. Rev. Lett.*, 76:4656–4659, Jun 1996.

[56] P. Maunz, D. L. Moehring, S. Olmschenk, K. C. Younge, D. N. Matsukevich, and C. Monroe. Quantum interference of photon pairs from two remote trapped atomic ions. *Nat Phys*, 3(8):538–541, 08 2007.

[57] Markus Michler, Klaus Mattle, Harald Weinfurter, and Anton Zeilinger. Interferometric bell-state analysis. *Phys. Rev. A*, 53:R1209–R1212, Mar 1996.

[58] P. Michler. A quantum dot single-photon turnstile device. *Science*, 290:2282 –2285, 2000.

[59] D. L. Moehring. Entanglement of single-atom quantum bits at a distance. *Nature*, 449:68–71, 2007.

[60] D. L. Moehring, P. Maunz, S. Olmschenk, K. C. Younge, D. N. Matsukevich, L. M. Duan, and C. Monroe. Entanglement of single-atom quantum bits at a distance. *Nature*, 449(7158):68–71, 09 2007.

[61] B. R. Mollow. Power spectrum of light scattered by two-level systems. *Phys. Rev.*, 188:1969–1975, Dec 1969.

[62] E. Moreau. Single-mode solid-state single photon sources based on isolated quantum dots in pillar microcavities. *Appl. Phys. Lett.*, 79:2865 –2867, 2001.

[63] A. Muller, E. B. Flagg, P. Bianucci, X. Y. Wang, D. G. Deppe, W. Ma, J. Zhang, G. J. Salamo, M. Xiao, and C. K. Shih. Resonance fluorescence from a coherently driven semiconductor quantum dot in a cavity. *Phys. Rev. Lett.*, 99:187402, Nov 2007.

[64] A. Nick Vamivakas, Yong Zhao, Chao-Yang Lu, and Mete Atature. Spin-resolved quantum-dot resonance fluorescence. *Nat Phys*, 5(3):198–202, 03 2009.

[65] A. Olmschenk. Quantum teleportation between distant matter qubits. *Science*, 323:486–489, 2009.

[66] David Press, Thaddeus D. Ladd, Bingyang Zhang, and Yoshihisa Yamamoto. Complete quantum control of a single quantum dot spin using ultrafast optical pulses. *Nature*, 456(7219):218–221, 11 2008.

[67] Michael Reck, Anton Zeilinger, Herbert J. Bernstein, and Philip Bertani. Experimental realization of any discrete unitary operator. *Phys. Rev. Lett.*, 73:58–61, Jul 1994.

[68] M. Riebe, H. Haffner, C. F. Roos, W. Hansel, J. Benhelm, G. P. T. Lancaster, T. W. Korber, C. Becher, F. Schmidt-Kaler, D. F. V. James, and R. Blatt. Deterministic quantum teleportation with atoms. *Nature*, 429(6993):734–737, 06 2004.

[69] C. Santori, D. Fattal, J. Vučković, G. S. Solomon, and Y. Yamamoto. Indistinguishable photons from a single-photon device. *Nature*, 419:594–597, 2002.

[70] C. Santori, M. Pelton, G. Solomon, Y. Dale, and Y. Yamamoto. Triggered single photons from a quantum dot. *Phys. Rev. Lett.*, 86:1502 –1505, 2001.

[71] J R Schaibley and P R Berman. The effect of frequency-mismatched spontaneous emission on atom-field entanglement. *Journal of Physics B: Atomic, Molecular and Optical Physics*, 45(12):124020, 2012.

[72] J. R. Schaibley, A. P. Burgers, G. A. McCracken, L.-M. Duan, P. R. Berman, D. G. Steel, A. S. Bracker, D. Gammon, and L. J. Sham. Demonstration of quantum entanglement between a single electron spin confined to an inas quantum dot and a photon. *Phys. Rev. Lett.*, 110:167401, Apr 2013.

[73] J. R. Schaibley, A. P. Burgers, G. A. McCracken, D. G. Steel, A. S. Bracker, D. Gammon, and L. J. Sham. Direct detection of time-resolved rabi oscillations in a single quantum dot via resonance fluorescence. *Phys. Rev. B*, 87:115311, Mar 2013.

[74] Marlan Scully. *Quantum optics*. Cambridge University Press, Cambridge New York, 1997.

[75] J. F. Sherson. Quantum teleportation between light and matter. *Nature*, 443:557–560, 2006.

[76] Jasprit Singh. *Physics of Semiconductors and Their Heterostructures*. Mcgraw-Hill, 9 1992.

[77] Jasprit Singh. *Electronic and Optoelectronic Properties of Semiconductor Structures*. Cambridge University Press, 1 edition, 3 2007.

[78] G. S. Solomon, M. Pelton, and Y. Yamamoto. Single-mode spontaneous emission from a single quantum dot in a three-dimensional microcavity. *Phys. Rev. Lett.*, 86:3903 –3906, 2001.

[79] D. Stick, W. K. Hensinger, S. Olmschenk, M. J. Madsen, K. Schwab, and C. Monroe. Ion trap in a semiconductor chip. *Nat Phys*, 2(1):36–39, 01 2006.

[80] T. H. Stievater, Xiaoqin Li, D. G. Steel, D. Gammon, D. S. Katzer, D. Park, C. Piermarocchi, and L. J. Sham. Rabi oscillations of excitons in single quantum dots. *Phys. Rev. Lett.*, 87:133603, Sep 2001.

[81] E. Togan, Y. Chu, A. S. Trifonov, L. Jiang, J. Maze, L. Childress, M. V. G. Dutt, A. S. Sorensen, P. R. Hemmer, A. S. Zibrov, and M. D. Lukin. Quantum entanglement between an optical photon and a solid-state spin qubit. *Nature*, 466(7307):730–734, 08 2010.

[82] Lev Vaidman. Teleportation of quantum states. *Phys. Rev. A*, 49:1473–1476, Feb 1994.

[83] Jürgen Volz, Markus Weber, Daniel Schlenk, Wenjamin Rosenfeld, Johannes Vrana, Karen Saucke, Christian Kurtsiefer, and Harald Weinfurter. Observation of entanglement of a single photon with a trapped atom. *Phys. Rev. Lett.*, 96:030404, Jan 2006.

[84] Tatjana Wilk, Simon C. Webster, Axel Kuhn, and Gerhard Rempe. Single-atom single-photon quantum interface. *Science*, 317(5837):488–490, 2007.

[85] Xiaodong Xu. *Coherent Optical Spectroscopy of a Single Semi-Conductor Quantum Dot*. Doctoral Thesis, University of Michigan, 2008.

[86] Xiaodong Xu, Bo Sun, Paul R. Berman, Duncan G. Steel, Allan S. Bracker, Dan Gammon, and L. J. Sham. Coherent optical spectroscopy of a strongly driven quantum dot. *Science*, 317(5840):929–932, 2007.

[87] Xiaodong Xu, Bo Sun, Erik D. Kim, Katherine Smirl, P. R. Berman, D. G. Steel, A. S. Bracker, D. Gammon, and L. J. Sham. Single charged quantum dot in a strong optical field: Absorption, gain, and the ac-stark effect. *Phys. Rev. Lett.*, 101:227401, Nov 2008.

[88] Xiaodong Xu, Yanwen Wu, Bo Sun, Qiong Huang, Jun Cheng, D. G. Steel, A. S. Bracker, D. Gammon, C. Emary, and L. J. Sham. Fast spin state initialization in a singly charged inas-gaas quantum dot by optical cooling. *Phys. Rev. Lett.*, 99:097401, Aug 2007.

[89] Xiaodong Xu, Wang Yao, Bo Sun, Duncan G. Steel, Allan S. Bracker, Daniel Gammon, and L. J. Sham. Optically controlled locking of the nuclear field via coherent dark-state spectroscopy. *Nature*, 459(7250):1105–1109, 06 2009.

[90] Jian Yang, Xiao-Hui Bao, Han Zhang, Shuai Chen, Cheng-Zhi Peng, Zeng-Bing Chen, and Jian-Wei Pan. Experimental quantum teleportation and multiphoton entanglement via interfering narrowband photon sources. *Phys. Rev. A*, 80:042321, Oct 2009.

[91] Wang Yao, Ren-Bao Liu, and L. J. Sham. Theory of control of the spin-photon interface for quantum networks. *Phys. Rev. Lett.*, 95:030504, Jul 2005.

[92] Amnon Yariv. *Quantum electronics*. Wiley, New York, 1989.

[93] Han Zhang, Xian-Min Jin, Jian Yang, Han-Ning Dai, Sheng-Jun Yang, Tian-Ming Zhao, Jun Rui, Yu He, Xiao Jiang, Fan Yang, Ge-Sheng Pan, Zhen-Sheng Yuan, Youjin Deng, Zeng-Bing Chen, Xiao-Hui Bao, Shuai Chen, Bo Zhao, and Jian-Wei Pan. Preparation and storage of frequency-uncorrelated entangled photons from cavity-enhanced spontaneous parametric downconversion. *Nat Photon*, 5(10):628–632, 10 2011.

[94] V. Zwiller. Single quantum dots emit single photons at a time: antibunching experiments. *Appl. Phys. Lett.*, 78:2476 –2478, 2001.